The Dissertation Committee for Jooyong Kim Certifies that this is the approved version of the following dissertation:

Parameter Extraction and Characterization of Transmission Line Interconnects Based on High Frequency Measurement

Committee:

Dean P. Neikirk, Supervisor

Francis C. Bostick

Mircea Driga

John H. Davis

Jim Bordelon

Parameter Extraction and Characterization of Transmission Line Interconnects Based on High Frequency Measurement

by

Jooyong Kim, B.S., M.S.

Dissertation

Presented to the Faculty of the Graduate School of
The University of Texas at Austin
in Partial Fulfillment
of the Requirements
for the Degree of

Doctor of Philosophy

The University of Texas at Austin
December, 2006

Dedication

To my parents, In-Soo Kim and Kyeong-Hyuk Ihm**,**
for genuine love, understanding, and patience

Acknowledgements

I would like to express my sincere gratitude to my supervisor Dr. Dean P. Neikirk for his guidance and support of my Ph.D. studies. Dr. Dean Neikirk provided helpful suggestions and valuable opinions and offered me continued encouragement. It is with his precious and insightful guidance that this work was completed. I also would like to acknowledge the members of my dissertation committee, Dr. Francis C. Bostick, Dr. Mircea Driga, Dr. John H. Davis, and Dr. Jim Bordelon for their valuable assistance.

I would like to thank former and present members of Team Neikirk, especially Dr. Sangwoo Kim, Dr. Robert James Friar, Dr. Young-Soo Sohn, Dr. Byunghwa Park, Byungki Woo, Dr. Sangwook Han, Matthew Andringa, Jun Wan Kim, Yoon Sok Park, Praveen Pasupathy, and Joo-Yun Jung. In addition many colleagues deserve my appreciation for their valuable advice and friendship, particularly Dr. Sung-Bo Hwang, Dr. Chul-Jae Choi, Dr. Min-Soo Noh, Hyoung-Sub Kim, and Dr. Jino Choi. I am also grateful to Dr. Chi Shi Chang and Dr. Sangwoo Kim for allowing me to work as an intern at International SEMATECH and making many helpful comments on the extraction, analysis, and modeling for interconnect problems.

Finally, I deeply appreciate the encouragement and devotion from my parents. They have provided love and emotional support throughout my life. I specially thank my wife, Hyun-Sun Park, for her loving and patient support over all my years. I also thank my lovable sons, Jinhong and Jaehoon, for making me proud and making my experience in Austin unforgettable.

Parameter Extraction and Characterization of Transmission Line Interconnects Based on High Frequency Measurement

Publication No._____________

Jooyong Kim, Ph.D.
The University of Texas at Austin, 2006

Supervisor: Dean P. Neikirk

New materials have been, and continue to be, introduced in an effort to reduce the impact of interconnect delay on performance. The accurate experimental characterization of on-wafer transmission lines, particularly lines using copper and low-k materials, is critically important to on-going high-speed digital integrated circuit designers. This dissertation aimed to examine the accurate electrical parameter extraction and characterization of on-wafer embedded microstrip transmission line test structures using high frequency measurements up to 40GHz in determining on-going high-speed digital integrated system performance. In particular we aimed to determine the dielectric constant and loss of low-k dielectric materials, as well as the accurate de-embedding network model of pads on interconnect parameter extraction, the impact of finite measurement precision and error propagation in on-wafer microwave measurement, and the impact of probe placement on high frequency on-wafer measurement.

Table of Contents

CHAPTER 1

CHAPTER 2

CHAPTER 3

CHAPTER 4

CHAPTER 5

IMPACT OF DE-EMBEDDING NETWORK MODELS FOR PAD ON THE EXTRACTION OF INTERCONNECT PARAMETERS

CHAPTER 6

List of Tables

List of Figures

Chapter 1

Introduction

Currently, high-speed interconnection related issues are among the key factors that determine the number of circuits that can be integrated on a chip as well as the chip performance. In the last ten years interconnects have been recognized as a significant limiter in the performance of high speed, high density integrated circuits [1-3]. As we continue reducing the feature sizes of transistors and enlarging chip dimensions, interconnects will reach even more importance, and they might eventually become the dominant performance limiting factors [4]. As a result, advances in interconnect technology might play a key role in integrated circuit density and performance as far as process advance. Hence, a careful and in-depth characterization of the behavior of the interconnect in a semiconductor technology is therefore not only desirable, but even essential.

According to the report from Intel, they expect the microprocessor frequency to double every 2 or 3 years [5]. As the microprocessor on-chip clock speeds have increased as well as reached multiple gigahertz [6], the fundamental development requirement for interconnect has been to meet the high-speed transmission needs of chips despite further scaling of feature size. This will become more common, and it may be that interconnects dominate electrical considerations at some point in the future, and consequently, high frequency would be an important factor requiring careful consideration in developing interconnect characterizations.

According to the International Technology Roadmap for Semiconductors (ITRS) [1], MPU 1/2 pitch size, which is 120nm in 2003 technology, will reach 60nm by the year 2009. By reducing the minimum feature size and enlarging the chip area, the density of transistors would double every generation. Consequently, the number and physical length of interconnects between gates increase accordingly. In general, as interconnection width and thickness decrease, resistance increase, and as interconnections become denser, capacitance increases. Consequently, denser and longer interconnects produce an interconnect that has lager delay which is one of the major concerns about interconnects. As successive technology shrinks in the local interconnect, interconnect width and dielectric thickness are reducing simultaneously. This indicates that the capacitance per unit length would be constant. Simultaneously, the length in the local interconnect would be reduced due to decreased device sizes. As a result, the delay would be roughly constant. On the other hand, the resistance per unit length is increasing with reducing interconnect width and thickness. Particularly, in the global interconnect, much longer interconnects will be required due to the increasing chip size. Hence it is certain that RC delay in the global line can be increased dramatically. For example, interconnect RC delay for a 1mm global line at minimum pitch, which is 42ps in 2003 technology, will reach 139ps by the year 2009, as estimated by ITRS [1]. Again, as far as the technology goal is concerned, interconnect delay can be problematic for scaling down accordingly and thus, it would be another important factor requiring careful consideration for interconnect characterization.

As interconnect delays become increasingly important, we can expect further innovation in design methodologies and architectures in the long term [3]. For the short term, the ITRS roadmap has identified many issues related to interconnect performance.

Among these, the 2001 roadmap (and subsequent updates) focused on new materials such as copper, which has higher conductivity than aluminum, and low dielectric constant materials rather than silicone dioxide for improved performance. Implementation of copper and low-k materials can allow scaling of the interconnect and minimizes the impact on interconnect delay [1, 7]. Therefore, one short term solution for the interconnect delay could be using copper and low-k materials to alleviate technology goals and meet technology goals.

Accordingly, the accurate characterization of transmission line interconnects, particularly lines using copper and low-k materials introduced in an effort to reduce the impact of interconnect delay on performance, is critically important to on-going high-speed digital integrated circuit designers [8-10]. Specifically, the dielectric constant and loss of low-k dielectric materials must be characterized [11-13]. In addition, transmission lines need to be characterized in realistic environments using on-wafer test structures and frequency ranges commonly used in integrated circuits [14-19]. The transmission line characteristics of an IC interconnect can be well approximated using the Telegrapher's equations, so long as the complex propagation constant and complex characteristic impedance of the line can be found. Most commonly, the transmission line parameters, R (resistance per unit length), L (inductance per unit length), C (capacitance per unit length), and G (conductance per unit length), are desired. Once the transmission line parameters are accurately determined, the electrical behavior of an interconnect can be evaluated. Therefore, the accurate extraction of transmission line parameters is essential to the characterizing of interconnects.

However, it can be difficult to accurately determine these parameters since the extracted parameters may have frequency dependencies [20, 21], which could be produced by measurement errors due to systematic uncertainties, and extraction errors induced by the incorrect de-embedding network model of pad parasitics. Particularly, the accuracy of such a measurement strongly depends on the ability to de-embed the frequency dependent parasitics introduced by the probing system and on the probe pads connected between the wafer probes and the actual transmission line interconnects.

Therefore, this dissertation focuses on the accurate electrical parameter extraction of on-wafer embedded microstrip transmission line test structures based on high frequency measurements of up to 40GHz, and accordingly the examination of the impact of error propagation on the extracted parameters and its consequences. Finally, we present the accurate de-embedding network model of pads on parameter extraction. As the work progresses, the following specific sub goals will be focused on in this dissertation:

- Characterization of low-k and SiO_2 dielectric materials with the extraction of dielectric constant and loss via one-port high frequency measurement in chapter 2,
- Characterization of copper and low-k / SiO_2 transmission line interconnects with the extraction of RLCG parameters via two-port high frequency measurement in chapter 2,
- Identification of the measurement error from systematic uncertainties via perturbation simulation in chapter 3,
- Investigation of the impact of probe placement on high frequency measurement of on-chip interconnects experimentally in chapter 4,
- Identification of the impact of pad de-embedding on the extraction of interconnect parameters in chapter 5,

- Finally, proposing the accurate de-embedding network modeling accounting for the current redistribution phenomena in the tested DUTs (Device Under Tests) in chapter 5,
- Chapter 6, summarizing the results in this dissertation and drawing conclusions about the accurate electrical parameters extraction of on-wafer embedded microstrip transmission line interconnects.

Chapter 2

High Frequency Measurements and Electrical Characterization of Copper / Low-k Transmission Line Interconnect

New materials have been, and continue to be, introduced in an effort to reduce the impact of interconnect delay on performance. The accurate experimental characterization of on-wafer transmission lines [22-27], particularly lines using copper and low-k materials, is critically important to on-going high-speed digital integrated circuit designs. Specifically, the dielectric constant and loss of low-k dielectric materials must be characterized. In addition, transmission lines need to be characterized in realistic environments using on-wafer test structures and frequency ranges commonly used in integrated circuits.

The transmission line characteristics of an IC interconnect can be well approximated using the Telegrapher's equations, so long as the complex propagation constant (γ) and complex characteristic impedance (Z_o) of the line can be found. All scattering parameters (S-parameters) for two-port (i.e., complex of S_{11}, S_{21}, S_{12}, and S_{22}) are needed for full characterization of the transmission line. Most commonly, the transmission line parameters, R (resistance per unit length), L (inductance per unit length), C (capacitance per unit length), and G (conductance per unit length) are desired. Once the transmission line parameters are accurately determined, the electrical behavior of the interconnect can be evaluated.

In this chapter, we will present the characterization and results of high frequency measurements for embedded microstrip Cu transmission line test structures (UT_microstrip) on SiO_2, low-k2 (Novellus' Coral low-k dielectric), and low-k1 (JSR Corp. low-k dielectric) wafers, for line-widths of 5μm, 0.25μm, and 0.175μm on the 800AZ test vehicle fabricated at SEMATECH. From measured S-parameters the extracted R (resistance per unit length), L (inductance per unit length), C (capacitance per unit length), and G (conductance per unit length**)** for copper/SiO_2 and low-k transmission line are presented. In addition the relative dielectric constant and loss tangent for various dielectric materials (SiO_2, low-k2 (Novellus' Coral low-k dielectric), and low-k1 (JSR Corp. low-k dielectric)) up to 40GHz are given.

2.1 DEVICE UNDER TEST (DUT)

The selection of the device under tests (DUTs) is governed by the need to characterize transmission line interconnects at a high frequency in realistic environments using on-wafer structures with copper, SiO_2, and low-k materials. This testing indicates the need for deep sub-micron transmission lines with copper, SiO_2, and low-k materials in test structures similar to current environment of actual integrated circuit. In addition, on-wafer, pad-only test structures on different dielectrics are useful for investigating new dielectrics in realistic environments.

The characterization of transmission line interconnects at high frequencies is done using a two-port vector network analyzer. All network analyzers have systematic errors in the accuracy of measured S-parameters [28], and therefore, the accuracy of the extracted parameters is also limited. By considering these errors in the design process [29, 30], test structures were designed to minimize the error bounds for R, L, C, and G by varying the length of the transmission line. This produces 13 different DUTs for the single embedded microstrip transmission line test structures as shown in Table 2.1.

Test Structures	Width	Length
microstrip_5_1380	5 µm	1380 µm
microstrip_5_4000	5 µm	4000 µm
microstrip_5_5000	5 µm	5000 µm
microstrip_5_7100	5 µm	7100 µm
microstrip_025_2100	0.25 µm	2100 µm
microstrip_025_3400	0.25 µm	3400 µm
microstrip_025_8100	0.25 µm	8100 µm
microstrip_025_11000	0.25 µm	11000 µm
microstrip_0175_2000	0.175 µm	2000 µm
microstrip_0175_3000	0.175 µm	3000 µm
microstrip_0175_5000	0.175 µm	5000 µm
microstrip_0175_7400	0.175 µm	7400 µm
microstrip_0175_9000	0.175 µm	9000 µm

Table 2.1: List of single embedded microstrip UT high frequency test structures on SEMATECH 800AZ Test Vehicle.

The first test structure consisted of a simple pad-only test structure on three different dielectrics (SiO_2, low-k2 (Novellus' Coral low-k dielectric), and low-k1 (JSR Corp. low-k dielectric)). These pad-only test structures were used to find the relative dielectric constant (ε_r) and dielectric loss of three different dielectric thin films (SiO_2, low-k2 (Coral), and low-k1 (JSR)). The pad-only test structures consisted of ground-signal-ground co-planar metal squares 50µm x 50µm in size. The ground pads (M2) were connected to the ground plane (M1) using vias (metal 1 (M1)-to-metal 2 (M2) contacts). The top and cross-sectional views of the pad-only test structures manufactured at SEMATECH are shown in Figure 2.1 (a) and (b) [31].

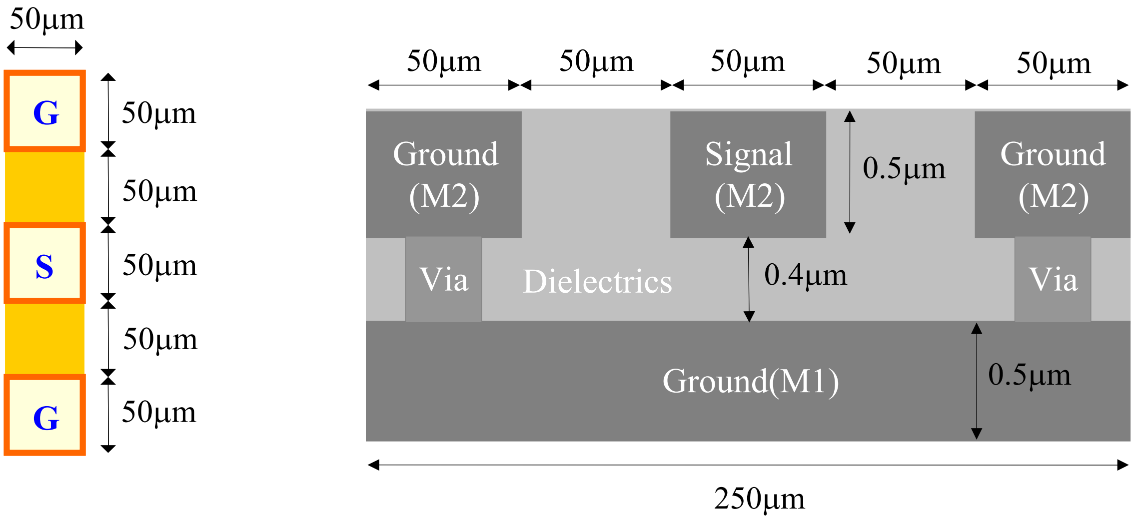

(a) (b)

Figure 2.1: UT High Frequency Pad-Only test structures on SEMATECH 800AZ test vehicle. (a) Top view (b) Cross-sectional view

The second set of test structures were embedded microstrip transmission lines having different geometries (5μm, 0.25μm, and 0.175μm line-width) on three different dielectric thin films (SiO_2, low-k2 (Novellus' Coral low-k dielectric), and low-k1 (JSR Corp. low-k dielectric)). The nominal cross-sectional dimensions for these structures are identical except for the width. These test structures have a 0.5μm thick signal conductor (M2) and 0.4μm separation of signal (M2) to ground (M1). Various line lengths for each line-width, as shown in Table 2.1, were also tested. The top and cross-sectional views of the single embedded microstrip test structures fabricated at SEMATECH, which have 0.25μm of target feature size, are shown in Figure 2.2 (a) and (b). Due to the problem of oxidation of the Cu lines, the design uses an overcoat layer and Al caps over Cu bond pads so that sufficiently accurate high frequency results can still be achieved. The overcoat process at SEMATECH uses a stack of 1000Å SiN / 2000Å SiO_2 (top) and 400Å TaN / 7500 Al (top) over Cu bond pads [32].

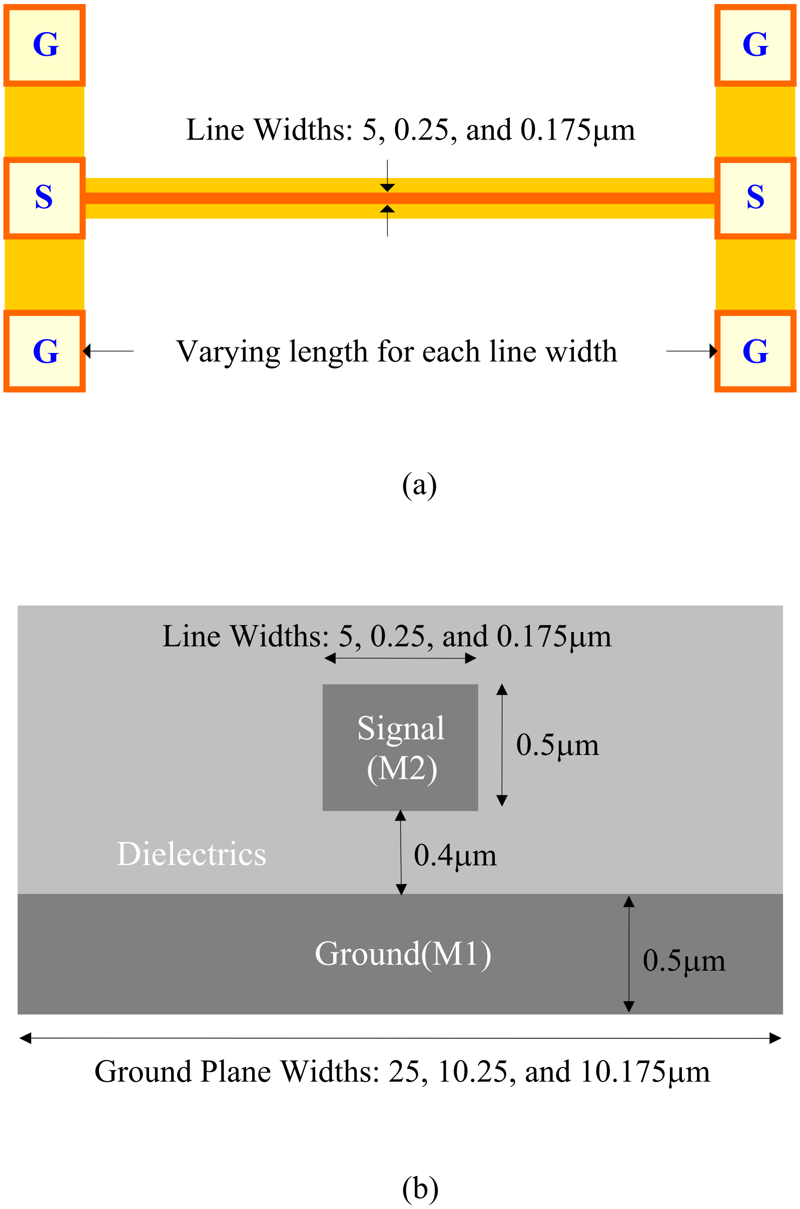

(a)

(b)

Figure 2.2: UT High Frequency embedded microstrip line test structures on SEMATECH 800AZ test vehicle. (Cu line / SiO_2, low-k2 (Coral), and low-k1 (JSR) dielectrics) (a) Top view (b) Cross-sectional view

2.2 DC MEASUREMENTS

The main objectives for DC measurements of resistance are to ensure signal line continuity so that there is a testable transmission line for the high frequency measurement. In addition, it provides a basis of comparison for the extracted resistance with the high frequency measurements.

DC resistance measurements were made using a simple Keithley 195A digital multimeter through two Cascade ACP40 Ground-Signal-Ground probes. Table 2.2 - 2.4 present the result of multiple DC measurement for SiO_2, low-k2 (Coral), and low-k1 (JSR) dielectrics. The resistance of interconnect lines depends on the materials (i.e., resistivity or conductivity), line length, and cross-sectional geometries of signal line. For comparison the resistance using the bulk conductivity of copper and assuming as-drawn dimensions (mask dimensions) can be calculated as given by Equation (2.1), where w and l are respectively the nominal line-width and line-length of the signal line (conductor), and t and σ represent the metal thickness of signal line and bulk conductivity of copper, $5.8\times10^{7} s/m$.

$$R_{cal} = \frac{l}{\sigma \times A} = \frac{l}{t \times w \times \sigma} \tag{2.1}$$

Structures	R_Cal	R_2,4	R_2,5	R_3,5	R_3,6	R_4,1	R_4,2	R_4,3	R_4,4	R_5,0	R_5,1
microstrip_5_1380	10	10.3	10.5	10.5	10.4	10.4	10.3	10.8	9.7	10.6	10.1
microstrip_5_4000	28	27.8	29.1	29.2	29.5	28.1	28	28.4	27.9	29	27.6
microstrip_5_5000	34	35.2	35.9	35.6	36.9	35	35.5	35.8	34.9	36.1	34.7
microstrip_5_7100	49	49.7	50.7	49.7	51.8	49.1	49.8	50.6	49.7	50.1	49.1
microstrip_025_2100	290	282.9	293.6	282.5	310.8	274.9	274.8	276.2	272.8	294.9	281.9
microstrip_025_3400	469	455.1	476.9	454.8	506	442.7	443.9	446.4	438.4	469.4	449.9
microstrip_025_8100	1117	1087.6	1136.0	1083.3	1201.4	1056.8	1058.7	1063.7	1049.5	1128.1	1079.2
microstrip_025_11000	1517	1480.0	1545.0	1472	1630	1436.9	1439.6	1445.8	1428.9	1535.6	1465.3
microstrip_0175_2000	394	460.0	474.9	445.5	493.3	444.4	426.4	413.3	453.1	476.4	450.5
microstrip_0175_3000	591	684.8	685.8	686	738.3	667.5	648.8	617.9	658.9	721.6	645.6
microstrip_0175_5000	985	1135.2	1146.3	1107.4	1212.7	1090.3	1054.7	1058.9	1099	1230	1100.3
microstrip_0175_7400	1458	1653.3	1665.9	1637.2	1768.8	1591.3	1555.3	1515.1	1609	1760.9	1571.3
microstrip_0175_9000	1773	1982.0	2010.0	1973.7	2131	1906.7	1868.3	1837.9	1921	2104	1901.5

Table 2.2: Measured DC Resistance of SiO2 Wafer. (R_Cal illustrates the calculated line-total-resistance (Ω) with nominal dimensions (line-width, line-thickness, and line-length) and bulk conductivity, for example R_2,4 illustrates the measured line-total-resistance for die site of column 2 and row 4 on wafer)

Structures	R_Cal	R_2,4	R_2,5	R_3,3	R_3,4	R_3,5	R_4,1	R_4,2	R_4,3	R_4,4	R_4,5
microstrip_5_1380	10	10	10	10	10	10	10	10	10	9	10
microstrip_5_4000	28	27	27	26	27	26	26	26	26	26	26
microstrip_5_5000	34	33	33	32	33	32	32	32	32	32	33
microstrip_5_7100	49	46	48	45	47	46	46	46	44	46	46
microstrip_0.25_2100	290	407	418	455	396	422	360	350	358	398	413
microstrip_0.25_3400	469	692	750	650	625	660	587	1024	572	599	655
microstrip_0.25_8100	1117	1637	1738	1617	1501	1580	1389	2081	1355	1444	1561
microstrip_0.25_11000	1517	2259	2380	2257	2052	2109	1881	2678	1835	1952	2110

Table 2.3: Measured DC Resistance of low-k2 (Coral) Wafer. (R_Cal illustrates the calculated line-total-resistance (Ω) with nominal dimensions (line-width, line-thickness, and line-length) and bulk conductivity, for example R_2,4 illustrates the measured line-total-resistance for die site of column 2 and row 4 on wafer)

Structures	R_Cal	R_3,3	R_4,1	R_4,3	R_4,4	R_4,5
microstrip_5_1380	10	12	12	13	12	13
microstrip_5_4000	28	33	33	33	32	32
microstrip_5_5000	34	42	41	40	40	42
microstrip_5_7100	49	57	57	57	56	57
microstrip_0.25_2100	290	406	424	390	434	572
microstrip_0.25_3400	469	647	675	709	659	783
microstrip_0.25_8100	1117	1693	1618	1609	1761	2287
microstrip_0.25_11000	1517	2438	2697	2363	2783	3052

Table 2.4: Measured DC Resistance of low-k1 (JSR) Wafer. (R_Cal illustrates the calculated line-total-resistance (Ω) with nominal dimensions (line-width, line-thickness, and line-length) and bulk conductivity, for example R_2,4 illustrates the measured line-total-resistance for die site of column 2 and row 4 on wafer)

In addition, if considering one square of the copper signal line, such that $w = l$, the theoretical sheet resistance (R_{s_theory}) value, which has units of Ω/square, using

$$R_{s\_theory} = \frac{1}{t \times \sigma} \tag{2.2}$$

where t and σ represent the thickness of signal line and bulk conductivity of copper, can be calculated. Finally the sheet resistance ($R_{s\_extracted}$), from the DC resistance measurement of transmission lines can be extracted using

$$R_{s\_extracted} = R_{measure} \times \frac{w}{l} \tag{2.3}$$

again assuming as-drawn dimensions (mask dimensions). The DC resistance can be obtained from multiplying the sheet resistance, $R_{s\_extracted}$, by the ratio of the length to the width of the conductor for any line-length of the transmission lines. As shown in Figure 2.3, the extracted sheet resistances ($R_{s\_extracted}$) from DC measurements of a 0.25µm line-width geometry for SiO_2 are fairly well matched with theoretical sheet resistances (R_{s_theory}) with the bulk conductivity. However, the $R_{s\_extracted}$ of low-k1 (JSR) and low-k2 (Coral) dielectrics are greater than theoretical sheet resistances (R_{s_theory}) with the bulk conductivity. Figure 2.4 clearly illustrates $R_{s\_extracted}$ is greater than R_{s_theory} for 5µm and 0.175µm geometries on a SiO_2 dielectric wafer which has 0.25µm of the target feature. If all line-widths have the same interconnect thickness, and if the liner is a small fraction of the total conductor cross-section, this should be the same for all line-widths. Figure 2.3 and Figure 2.4 might suggest some portions of the actual line thickness or line width are different from the as-drawn dimensions (mask dimensions) due to the significant dishing or others. Hence, the process variations in interconnect width and thickness of the thin film conductor cause interconnect resistance variations.

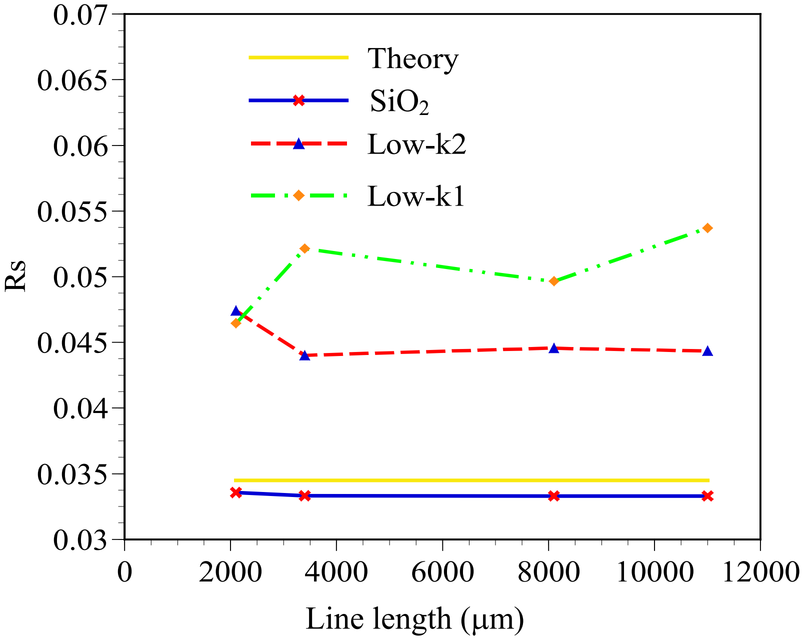

Figure 2.3: Extracted Sheet Resistance (R_s) of different dilectrics. (SiO_2, low-k2 (Coral), and low-k1 (JSR) dielectrics of 0.25µm line-width)

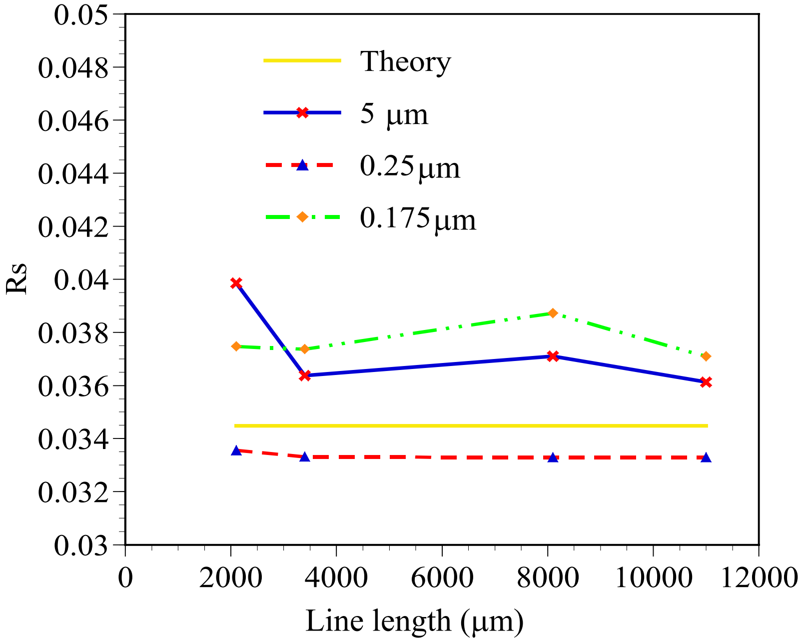

Figure 2.4: Extracted Sheet Resistance (R_s) of different geometries. (5µm, 0.25µm, and 0175µm line-width of SiO_2 dielectrics)

From regression analysis of the DC resistance measurements, the total-line-resistance for any line length as well as the contact resistance (R_c) can be examined for different geometries and dielectrics. Contact resistance (R_c) represents resistances of the external test cables connected between the HP 8510B and the Cascade ACP40 Ground-Signal-Ground wafer probes, connectors, the pad itself, the probe contact at the landing pad, and the vias (metal 1-to-metal 2 contacts) of probe pads. In high frequency measurement we could eliminate the parasitics of the external cables, connectors, and wafer probes through calibration. However, the resistive parasitics of the pad contact and vias (metal 1-to-metal 2 contacts) could not be removed through the microwave calibration. Therefore, the resistive parasitics of the pad contact and vias (metal 1-to-metal 2 contacts) for the RF parameter extraction of the two-port need be considered in the de-embedding procedures, which will be shown in section 2.4, even though they have very small effects due to too much lossy signal line for RLCG extraction of transmission line interconnect of the full two-port high frequency measurement.

2.3 HIGH FREQUENCY MEASUREMENT SET-UP

The vector network analyzer (HP 8510B), S-parameter test set (HP 8516A), and synthesized sweeper (HP 8341B) were used to obtain the scattering parameters (S-parameters) for an embedded microstrip transmission line with two-ports. The vector network analyzer (VNA), designed with a characteristic impedance of 50Ω, was connected through a microwave cable to the two Cascade ACP40 Ground-Signal-Ground 100 wafer probes, which can be used from DC to 40GHz, with characteristic impedances of 50Ω as shown in Figure 2.5.

At high frequencies, it is hard to measure the total voltage and current directly at the device ports. That is the reason that scattering parameters (S-parameters) were developed. Scattering parameters (S-parameters), which are related to common measurement with the vector network analyzer (VNA), are relatively easy to measure. A vector network analyzer (VNA) is used for high frequencies and microwave design purposes [33, 34]. The VNA is quite appropriate for measuring the response of a DUT as a function of frequency. The output of a VNA is ratios of reflected and transmitted power. Through mathematical manipulation of the power ratios, the electrical parameters can be extracted for digital high-speed designs. These include propagation constant, characteristic impedance, frequency dependent resistance, capacitance, inductance, and conductance parameters.

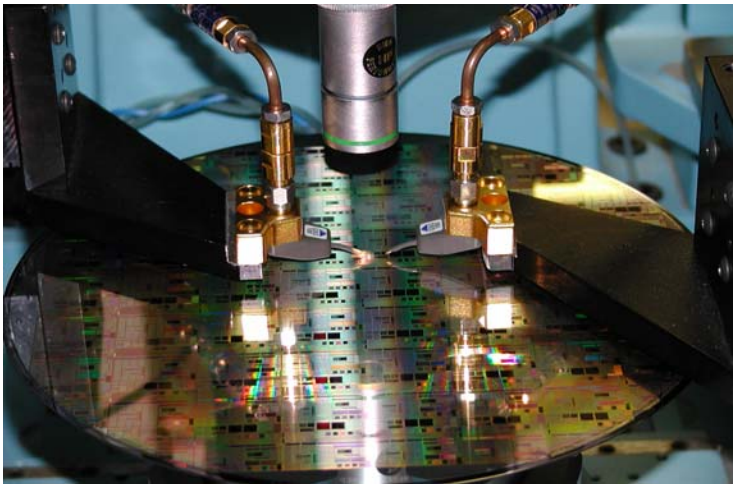

Figure 2.5: High Frequency measurement set-up.

Connections are made to the wafer using microwave wafer probes (i.e., Cascade ACP40 Ground-Signal-Ground 100 wafer probes in this chapter) and probe pads on the device under test (DUT). The three tips of the probe, such as Ground-Signal-Ground of the microwave on-wafer probes is fixed, which means each different probe pad layout (i.e., pitch of pads) requires a different probe (here, 100μm pitch) as shown in Figure 2.6.

The wafer probe has two ground tips on both ends of the center signal tip. Similarly, the probe pads should be laid out as a single signal pad on the center with a ground pad on either ends, as shown in Figure 2.7. The probe pads on DUTs, which were fabricated at SEMATECH, have an overcoat layer and Al caps over Cu bond pads to prevent the oxidation of the Cu, which must be scraped off in order for the on-wafer probes to make good electrical contact with the pads. Consequently, downward pressure should be applied to the wafer probes to maintain good electrical contact.

Figure 2.6: Top view of three-tips of Cascade Ground-Signal-Ground on-wafer probe.

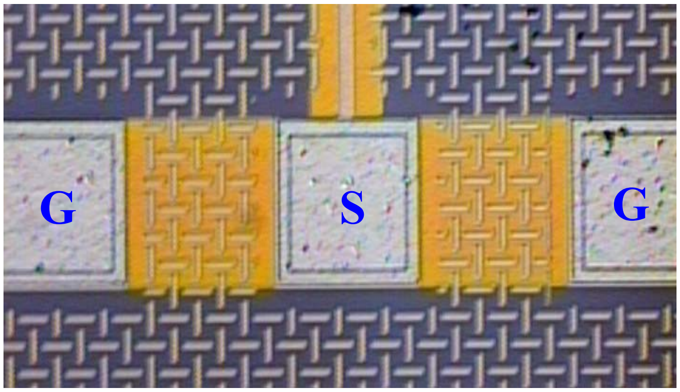

Figure 2.7: Top view of three-probe pads with Ground-Signal-Ground (GSG) configuration connected to signal line fabricated at SEMATECH.

Cascade 005-016 Impedance Standard Substrate (ISS) was used for calibrations applied in this chapter. ISS contains various elements that exhibit well defined electrical characteristics and is mechanically well-suited with Cascade wafer probe tips. The ISS elements include short, load, thru-line, and a couple of transmission line patterns for calibration and verification.

Using contact with these elements during a calibration procedure, the effects of the wafer probes and cabling can be removed for the high frequency measurement. Consequently, as a result of the calibration procedures, which are the open-short-load (OSL) calibration method for one-port measurement and short-open-load-thru (SOLT) calibration method [28, 35] for two-port measurement using a Cascade impedance standard substrate (ISS), the reference planes of the measurements must be taken at the contact points (i.e., end tips) of the microwave wafer probes. Then, the VNA collects the data and processes it using the calibration information. The S-parameters are then sent to the control computer where we extract the parameters.

A VNA (HP 8510B) was used to measure the S-parameters of the pad-only test structure using a one-port measurement. The single embedded microstrip structures were measured with two-port measurement. The measurements were made from 500MHz to 40GHz. Measured S-parameters characterize the reflection and transmission characteristics of the device under test (DUT). The S-parameters fully characterize a two-port device but do not directly provide any information on the transmission line parameters of the DUT. The S-parameters must be mathematically converted to obtain information about the transmission line parameters. We chose to use the transmission line parameters, which we refer to as R (resistance per unit length), L (inductance per unit length), C (capacitance per unit length), and G (conductance per unit length) parameters.

2.4 PARAMETER EXTRACTION AND CHARACTERIZATION

The network analyzer measures S-parameters that characterize the reflection and transmission characteristics of the device under test (DUT). The S-parameters characterize a one-port or two-port device but do not directly provide the interconnect parameters of the DUT due to embedded pad parasitics at both ends. Using an assumed network model of these parasitics, the S-parameters are converted into transmission line parameters such as R (resistance per unit length), L (inductance per unit length), C (capacitance per unit length), and G (conductance per unit length). Hence, in section 2.4, we will present how to extract parameters from one-port and two-port measurement based on an assumed network model of pads and the extracted results.

2.4.1 One-Port

A network analyzer was used to measure the S-parameter of the pad only test structure using one-port measurement. The measurement frequency sweep started at 500MHz and ended at 40GHz. The probe pad-only configuration used in one-port measurement is for a probe with one signal (middle) and two grounds as shown in Figure 2.1 (a) and (b). The ground pads (M2) were connected to the ground plane (M1) using vias (metal 1-to-metal 2 contacts) as shown in Figure 2.1 (b), and the signal pad was connected to the signal line as shown in Figure 2.2 (a).

The signal and ground pads have a mutual coplanar parasitic capacitance, but it should be much smaller than the parallel plate capacitance of the signal pad to the ground plane. In addition, the fringing component does not need to be counted because the ratio (width / thickness) is so large (i.e., 100). However, the contact pads produce a considerable amount of the parasitic capacitance compared to the capacitance of the transmission lines itself. Both resistive and capacitive pad parasitics should be de-embedded in high frequency characterization for two-port parameter extraction. High frequency de-embedding, described in section 2.4.2 in detail, eliminates the resistive (R_c) and capacitive (C_{pad}) pad parasitics. The resistive parasitics (R_c) were extracted from DC measurement. In addition the capacitive parasitics (C_{pad}) were extracted from the measured S_{11} parameter of the pad-only test structure with the assumed Z_o, which is equals to 50Ω. The Z-parameter of the pad-only test structure (Z_{pad}) can be extracted from the measured complex S_{11} parameter and assumed Z_o, as shown in Equation (2.4) and (2.5).

$$S_{11} = \frac{Z_{pad} - Z_o}{Z_{pad} + Z_o} \tag{2.4}$$

$$Z_{pad} = Z_o \times \frac{1 + S_{11}}{1 - S_{11}} \tag{2.5}$$

A Smith chart is helpful for visualizing frequency domain problems. The horizontal line through the center of the Smith chart corresponds to the real impedance axis, which goes from zero ohms (short) on the left-hand side to infinite impedance (open) on the right-hand side. The outside perimeter is equivalent to purely reactive impedance values such as purely capacitive or inductive load. The Smith chart from a one-port S-parameter measurement for open pad-only test structure, as shown in Figure 2.8, confirms the pad has very small resistive parasitics and primarily capacitive parasitics for the different dielectrics tested. Furthermore, the landing pads produce a considerable amount of parasitic capacitance compared to the capacitance of the transmission line itself. Figure 2.9 illustrates the comparison between the capacitance of pad-only test structures and $\frac{\text{self - capacitance}}{10}$ of the transmission line (example: 5μm width and 4000μm length) for different dielectrics. The parasitic capacitances for different dielectrics are about the same order of magnitude as the $\frac{\text{self - capacitance}}{10}$ of the transmission line. That means the contact pads produce a considerable amount of parasitic capacitance. Consequently, the parasitic capacitance should be de-embedded during high frequency characterization for parameter extraction from the two-port measurement.

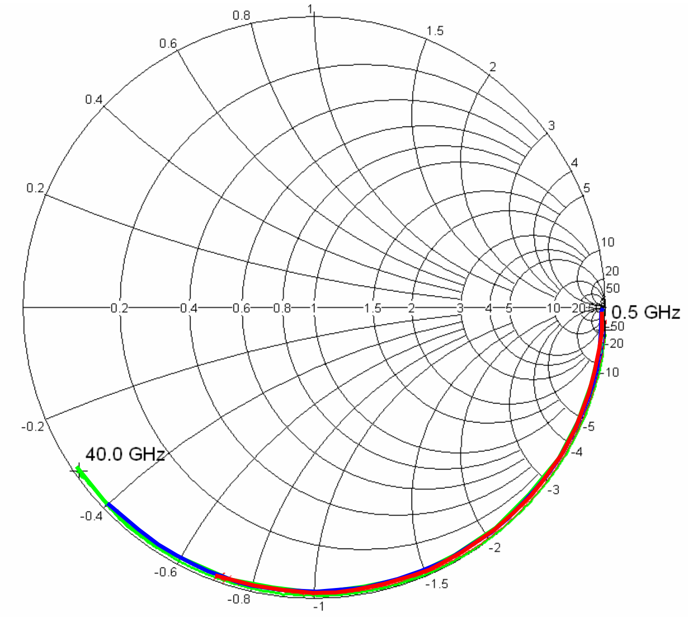

Figure 2.8: Smith Chart from one-port measurement for pad-only test structures of different dielectrics. (SiO_2, low-k2 (Coral), and low-k1 (JSR) dielectrics)

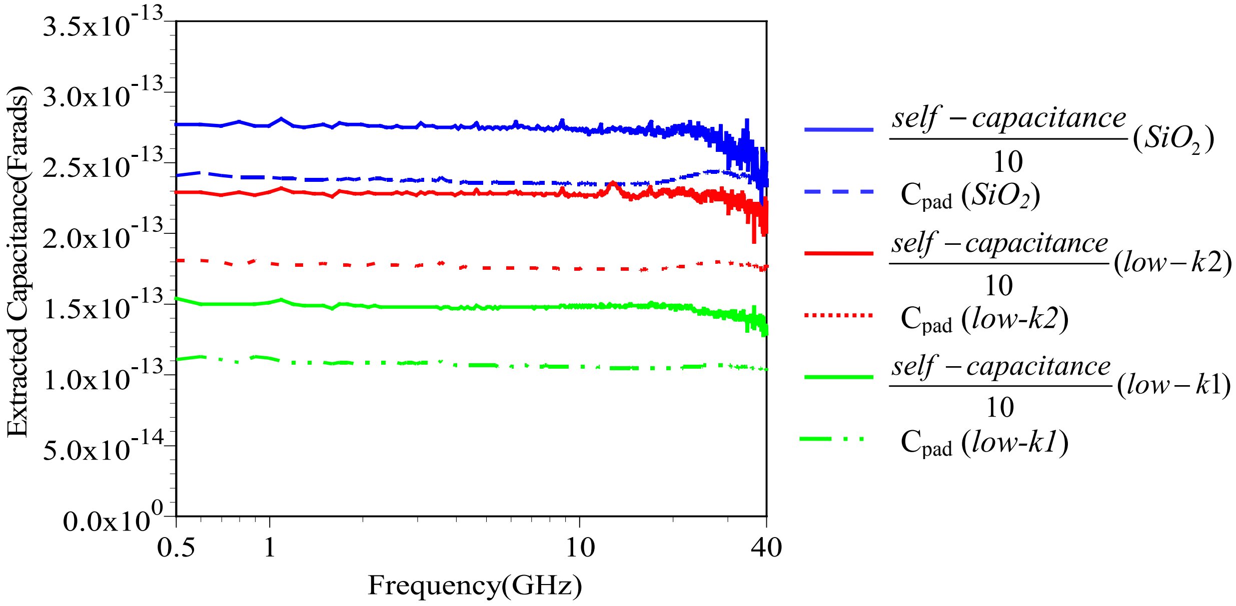

Figure 2.9: Comparison between pad capacitance (C_{pad}) and $\frac{\text{self - capacitance}}{10}$ of the transmission line (5μm width and 4000μm length) for SiO_2, low-k2 (Coral), and low-k1 (JSR) dielectrics.

A one-port measurement of on-wafer pad-only test structures of different dielectrics will be considered as examining characteristics of dielectrics in a realistic environment. One dielectric characteristic from one-port measurement is the dielectric constant, which is a measure of the response of a material to an electric field. Dielectric materials are usually characterized by their relative dielectric constant (ε_r), as well as a quantity to specify loss produced by the dielectric. The other dielectric characteristic from a one-port measurement is dielectric loss, which is the loss tangent (tanδ), the ratio of the conduction current to the displacement current through a capacitor. A “dielectric” by definition must have a loss tangent of less than one, while a “conductor” has a loss tangent greater than one. Loss tangent is also the ratio of a material’s dielectric relaxation frequency (σ/ε) to the operating frequency (ω). Hence, loss tangent is related to the conductivity σ of the dielectric, the real part of the dielectric constant ε, and the angular frequency (ω) by

$$Tan\delta = \frac{\sigma}{\omega\varepsilon} \tag{2.6}$$

A smaller loss tangent indicates less conduction current and is therefore more desirable for interconnect applications; in most conventional microwave and RF applications, a loss tangent of less than 0.01 (i.e., of the current flowing through a capacitor, only 1% is conduction current) would be considered a "good" dielectric. For IC interconnect applications, loss tangents higher than this can probably be tolerated. Loss tangent is a convenient measure of dielectric loss since it is roughly frequency independent for many materials. When the microstrip is embedded in a uniform lossy dielectric, the current flows along the field lines in the dielectric; so, the relation between G and C is simply

$$G = \omega C \times Tan\delta \tag{2.7}$$

Thus, the loss tangent (tanδ) will be Equation (2.6).

In extracting the dielectric constant (ε_r) and loss tangent (Tanδ), the S-parameters of the pad-only structure were first measured using one-port measurements up to 40GHz. From the measured S-parameters (S_{11} or S_{22}), the complex Z-parameter of the pad-only structure was extracted. S_{11} is the reflection coefficient, and the relation of the complex Z-parameter (Z_{pad}) and S_{11} are defined in Equation (2.4) and (2.5). The model of the pad only structure consists of only a lumped resistor and capacitor, which considerably reduces any uncertainties in the extraction process. In addition, a scanning electron micrograph (SEM), as shown in Figure 2.10, was used to provide more accurate cross-sectional dimensions to extract the dielectric constant and loss tangent after manufacturing was completed. However, it cannot completely eliminate the dimensional uncertainties because the cross-sectional dimensions may change from die to die and DUT to DUT.

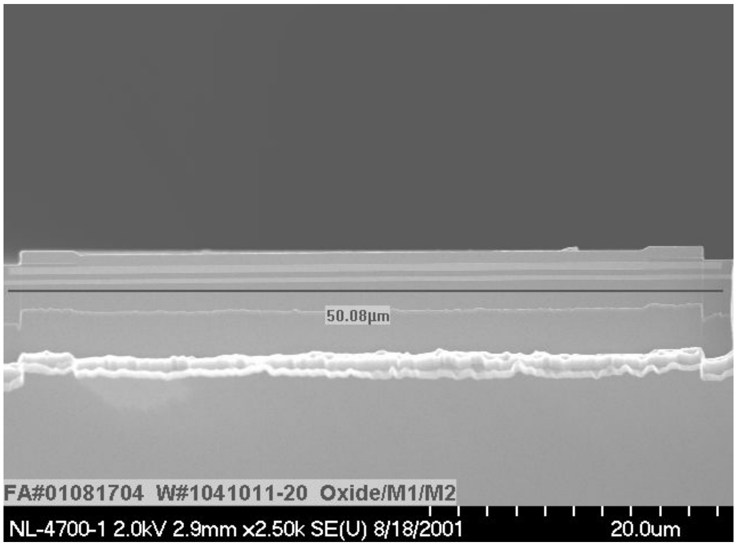

(a) Width of signal pad

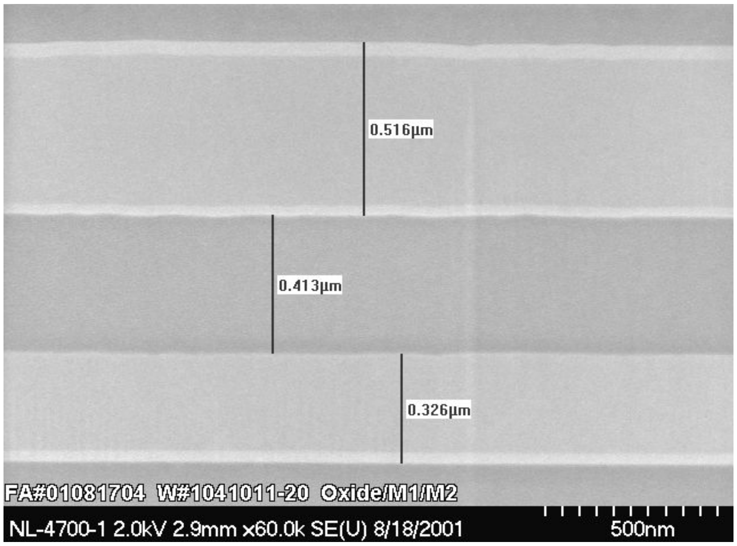

(b) Cross-section view of signal pad

Figure 2.10: Cross-sectional view of pad-only test structure (example: SiO_2 dielectric). Scanning Electron Micrograph (SEM) courtesy of SEMATECH.

In one-port measurements with pad-only test structures, both dielectric constant and loss tangent for various dielectric thin films were extracted. Extracted dielectric constants were 4.2-4.4 for SiO_2, 3.1-3.3 for low-k2 (Coral), and 1.75-2 for low-k1 (JSR) up to 40GHz as shown in Figure 2.11.

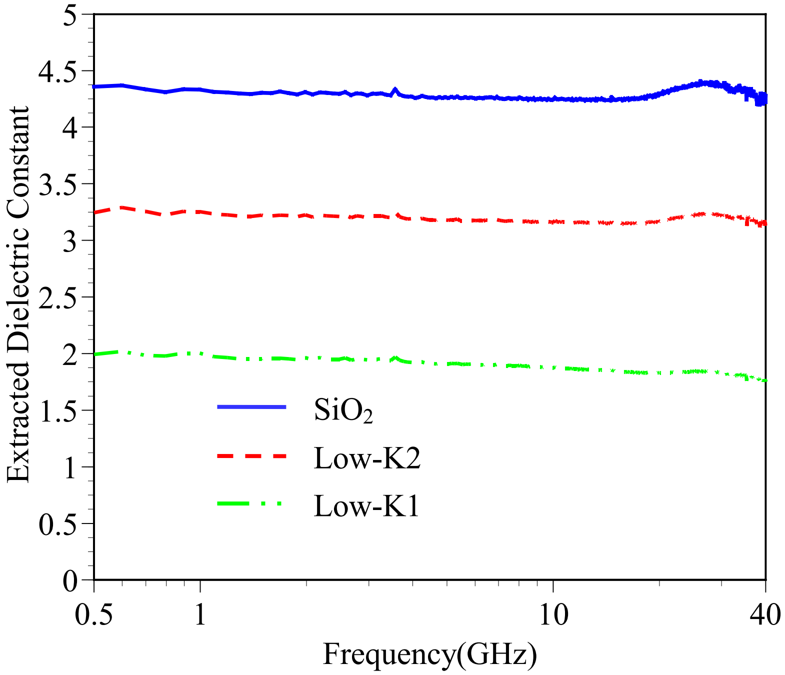

Figure 2.11: Extracted Dielectric Constant (ε_r) for various dielectrics.

The dielectric losses for the three dielectrics were so small compared to ohmic conductor losses that the extraction of loss tangent is dominated by noise and the finite precision of the measurement instrument [30], resulting in negative extracted values at high frequencies as shown in Figure 2.12. This is true even for the large area pad structures which are more optimal than the transmission line for loss tangent measurements. Based on the measurements the actual loss tangent is much less than 0.1, and most likely to be below 0.01. This indicates that dielectric loss is negligible for all measured dielectrics.

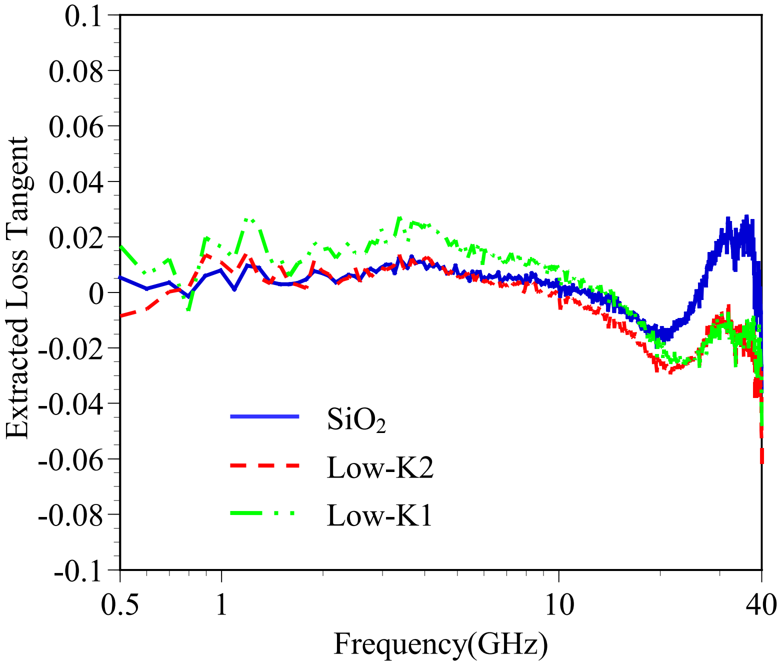

Figure 2.12: Extracted Loss Tangent (Tanδ) for various dielectrics.

2.4.2 Two-Port

A network analyzer was used to characterize the S-parameters of the single embedded microstrip test structures with two-port measurements. The frequency sweep used in the measurement started at 500MHz and terminated at 40GHz. In the measurement procedure for transmission lines, the S-parameters of a given transmission line with two-port and a pad-only structure with one-port are first measured. Two-port S-parameters for a transmission line can be fully described with a 2×2 matrix. The S-parameters for a lossy transmission line are given by Equation (2.8) [36, 37], where Z_{port} (50Ω here) is the port impedance of the VNA, Z_o is the characteristic impedance of the transmission line, γ is the propagation constant of the line, and l is the line-length.

$$\begin{bmatrix} S_{11} & S_{12} \\ S_{21} & S_{22} \end{bmatrix} =$$

$$\begin{bmatrix} \dfrac{(Z_o^2 - Z_{port}^2)\sinh \gamma l}{(Z_o^2 + Z_{port}^2)\sinh \gamma l + 2Z_{port}Z_o \cosh \gamma l} & \dfrac{2Z_{port}Z_o}{(Z_o^2 + Z_{port}^2)\sinh \gamma l + 2Z_{port}Z_o \cosh \gamma l} \\ \dfrac{2Z_oZ_{dut}}{(Z_o^2 + Z_{port}^2)\sinh \gamma l + 2Z_{port}Z_o \cosh \gamma l} & \dfrac{(Z_{dut}^2 - Z_o^2)\sinh \gamma l}{(Z_o^2 + Z_{port}^2)\sinh \gamma l + 2Z_{port}Z_o \cosh \gamma l} \end{bmatrix} \tag{2.8}$$

Since transmission lines are symmetrical and reciprocal networks, S_{11} equals to S_{22}, and S_{12} equals to S_{21}. The S-parameters are implicitly functions of frequency, then it would be because γl and Z_o are functions of frequency. Real networks containing transmission lines have parasitics such as pad parasitics at both ends that are included in the network analyzer measurement, but not in the network model given by Equation (2.8). Assuming that the parasitic is in cascade with the transmission line, a different set of parameters, the ABCD parameters, allows the cascading of networks by the multiplication of the ABCD matrices. Measured S-parameters can be converted to ABCD parameters using Equation (2.9) to (2.12) [38-40]. In addition, the relationship between ABCD parameters and S-parameters can be shown in Equation (2.13) to (2.16).

$$A = \frac{(1+S_{11})\times(1-S_{22})+S_{12}\times S_{21}}{2S_{21}} \tag{2.9}$$

$$B = Z_0 \times \frac{(1+S_{11})\times(1+S_{22})-S_{12}\times S_{21}}{2S_{21}} \tag{2.10}$$

$$C = \frac{1}{Z_0}\times \frac{(1-S_{11})\times(1-S_{22})-S_{12}\times S_{21}}{2S_{21}} \tag{2.11}$$

$$D = \frac{(1-S_{11})\times(1+S_{22})+S_{12}\times S_{21}}{2S_{21}} \tag{2.12}$$

$$S_{11} = \frac{A+\frac{B}{Z_o}-CZ_o-D}{A+\frac{B}{Z_o}+CZ_o+D} \tag{2.13}$$

$$S_{12} = \frac{2(AD-BC)}{A+\frac{B}{Z_o}+CZ_o+D} \tag{2.14}$$

$$S_{21} = \frac{2}{A+\frac{B}{Z_o}+CZ_o+D} \tag{2.15}$$

$$S_{22} = \frac{-A+\frac{B}{Z_o}-CZ_o+D}{A+\frac{B}{Z_o}+CZ_o+D} \tag{2.16}$$

The extracted transmission line interconnect parameters require an assumed network model [41-45]. The extracted parameters were based on a network model consisting of a RLCG transmission line with a pad capacitance (C_{pad}) and contact resistance (R_c) at both ends of the transmission line. Both ends of the transmission line are assumed to be the same, and only the signal probe pads are assumed to have a parasitic capacitance to the ground plane. Pad parasitics should be subtracted from the two-port high frequency measurement. The de-embedding method, which can eliminate the capacitive and resistive parasitics from the high frequency data, was used to correct the two-port measurements. Assuming that the same parasitics are with the transmission line at both ends as shown in Figure 2.13, the ABCD parameters allows the cascading of networks by the multiplication of the ABCD matrices. The relationship of $[ABCD]_{\text{line}}$ and $[ABCD]_{\text{measured}}$ matrices is shown in Equation (2.17) and (2.18).

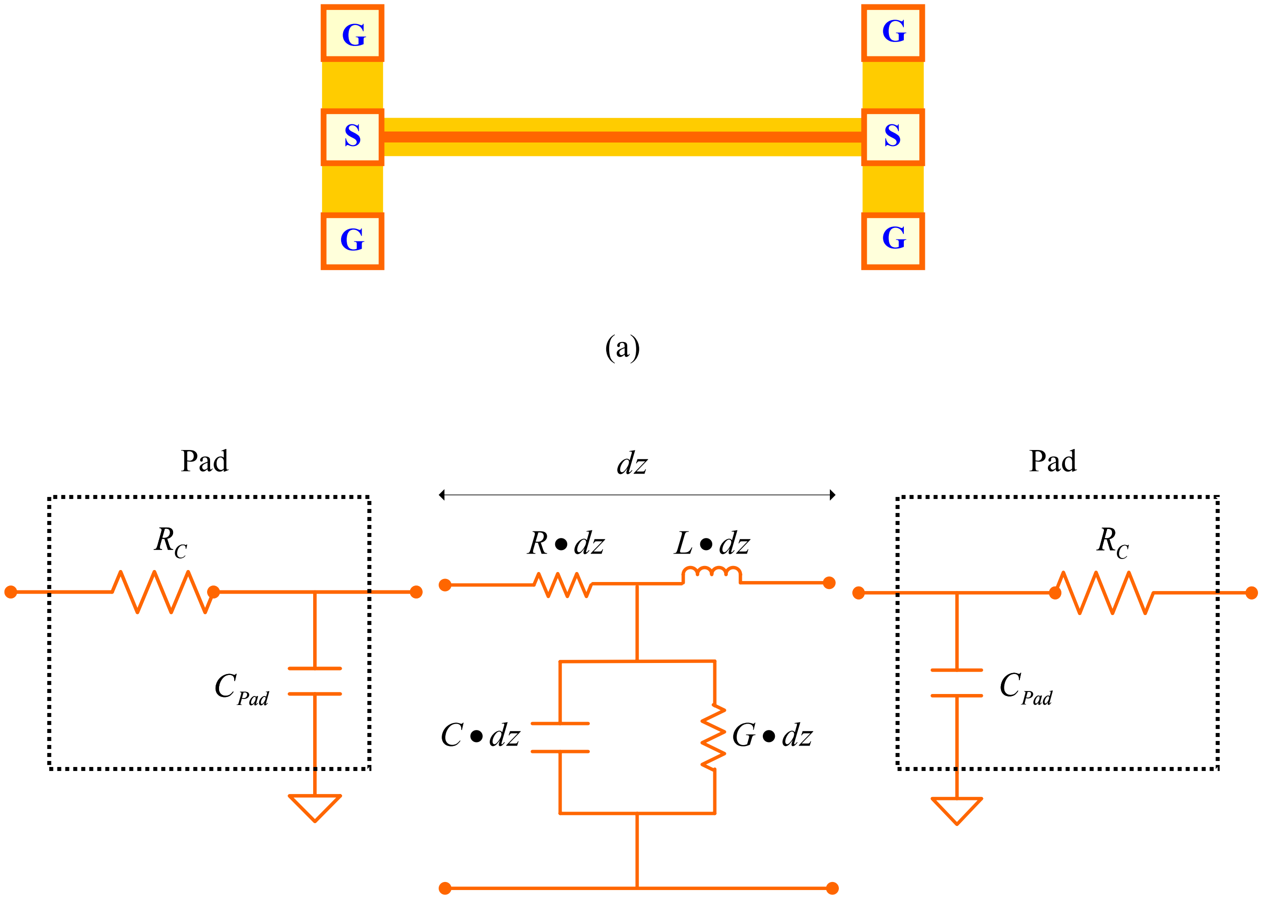

(a)

(b)

Figure 2.13: Network under test, including probe pads at both ends. (a) Test Structure, (b) an Assumed Network Model.

$$\begin{bmatrix} A & B \\ C & D \end{bmatrix}_{measured} = \begin{bmatrix} 1 & Z_{contact} \\ 0 & 1 \end{bmatrix} \begin{bmatrix} 1 & 0 \\ Y_{pad} & 1 \end{bmatrix} \begin{bmatrix} A & B \\ C & D \end{bmatrix}_{line} \begin{bmatrix} 1 & 0 \\ Y_{pad} & 1 \end{bmatrix} \begin{bmatrix} 1 & Z_{contact} \\ 0 & 1 \end{bmatrix} \tag{2.17}$$

$$\begin{bmatrix} A & B \\ C & D \end{bmatrix}_{line} = \begin{bmatrix} 1 & 0 \\ Y_{pad} & 1 \end{bmatrix}^{-1} \begin{bmatrix} 1 & Z_{contact} \\ 0 & 1 \end{bmatrix}^{-1} \begin{bmatrix} A & B \\ C & D \end{bmatrix}_{measured} \begin{bmatrix} 1 & Z_{contact} \\ 0 & 1 \end{bmatrix}^{-1} \begin{bmatrix} 1 & 0 \\ Y_{pad} & 1 \end{bmatrix}^{-1} \tag{2.18}$$

Since the DUT is quite lossy, the $Z_{contact}$ (i.e., parasitic resistance (R_c)) of the probe pads at both ends has a small effect on the parameter extraction for the transmission line. However, the Y_{pad} (i.e., parasitic capacitance (C_{pad})) of the probe pads can significantly affect the parameter extraction because C_{pad} is considerably large compared to interconnect parameters as shown in Figure 2.9. Thus, in the de-embedding procedures for transmission parameters, we chose the mean value (averaged over the frequency sweep up to 40GHz) of the extracted pad capacitance via one port measurement among multiple experiments, although the extracted pad capacitances are relatively frequency independent.

After de-embedding the pad parasitics at both ends, the characteristic impedance (Z_o) and propagation constant (γ) are calculated for the transmission line only from the $[ABCD]_{line}$ parameters, as shown in Equation (2.19).

$$\begin{bmatrix} A & B \\ C & D \end{bmatrix}_{line} = \begin{bmatrix} \cosh \gamma l & Z_o \sinh \gamma l \\ \dfrac{\sinh \gamma l}{Z_o} & \cosh \gamma l \end{bmatrix} \tag{2.19}$$

Once the characteristic impedance (Z_o) and propagation constant (γ) are determined, and after the specified nominal line-length is divided out, the transmission line parameters, the R (resistance per unit length), L (inductance per unit length), C (capacitance per unit length), and G (conductance per unit length) parameters, are calculated using Equation (2.20) to (2.25).

$$\gamma = \sqrt{(R + j\omega L)(G + j\omega C)} \tag{2.20}$$

$$Z_o = \sqrt{\frac{(R + j\omega L)}{(G + j\omega C)}} \tag{2.21}$$

Then

$$R = \mathrm{Re}\left\{\gamma Z_o\right\} \tag{2.22}$$

$$L = \mathrm{Im}\left\{\gamma Z_o\right\} / \omega \tag{2.23}$$

$$C = \mathrm{Im}\left\{\gamma / Z_o\right\} / \omega \tag{2.24}$$

$$G = \mathrm{Re}\left\{\gamma / Z_o\right\} \tag{2.25}$$

The resistance (R), inductance (L), capacitance (C), and conductance (G) parameters per unit length from S-parameters obtained using the network analyzer are extracted. Based on the two-port measurements of 0.25μm width and 3400μm length transmission lines of the SiO_2, low-k2 (Coral), and low-k1 (JSR) dielectrics, the extracted R, L, C, and G per unit length are presented as shown in Figure 2.14, 2.16, 2.18, and 2.20, respectively. And Figure 2.15, 2.17, and 2.19 show the extracted R, L, and C per unit length of 0.25μm width of SiO_2 dielectric for 2100μm, 3400μm, 8100μm, and 11000μm line-length. The resulting extracted parameters are based on the lumped contact resistance (R_c) and the mean value of lumped pad capacitance (C_{pad}) from multiple one-port measurements of the pad-only test structure at the de-embedding network model.

As shown in Figure 2.14, the variation in extracted R for the various dielectrics is due to process variation, as verified by DC resistance measurements. The extracted R per unit length is fairly frequency independent below 20GHz as shown in Figure 2.14 and 2.15. The extracted R per unit length seems like a roll up at higher frequencies. Such a roll up might be attributed to skin effect in the signal line because of the high frequencies involved. However, it is unlikely that the skin depth is important for any of the lines measured here because the thickness of the signal line (0.5μm) is less than 2 skin depths at the highest frequency. The frequency dependence is likely due to another cause. For instance, length offset errors in S-parameter measurement can change the effective DUT by including a finite length transmission on either end of the desired DUT, which will be discussed in chapter 3 and 4. On the other hand, the wrong de-embedding network model might be the cause of the frequency dependence, which will be covered in chapter 5.

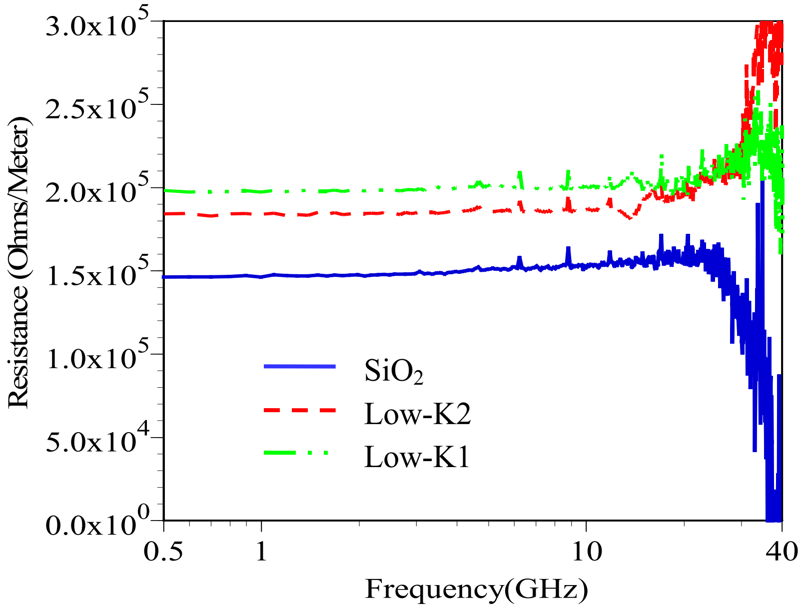

Figure 2.14: Extracted R per unit length of 0.25µm line-width and 3400µm line-length for various dielectrics.

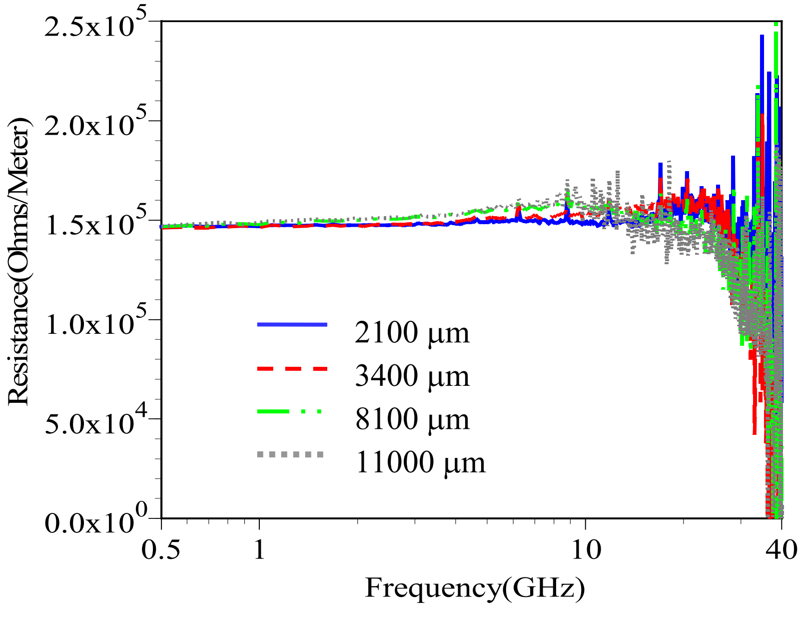

Figure 2.15: Extracted R per unit length of 0.25µm line-width of SiO_2 dielectric for various line-lengths.

The extracted L per unit length may exhibit some weak frequency dependence for the mid frequency range as shown in Figure 2.16 and 2.17. The extracted L per unit length shows an apparent frequency dependency, but again, there is no evidence that the frequency dependence is due to anything but extraction errors, such as length offset error or wrong de-embedding of pad, rather than current redistribution in the metal due to skin effect. Since the metal is less than two skin depths thick even at 40GHz, current redistribution would not be expected to occur.

Shorter lines (2100μm and 3400μm line-length) cause a smaller error than longer lines (8100μm and 11000μm line-lengths) at low frequencies as shown in Figure 2.17. At a low frequency, this is an artifact due to the impact of finite measurement precision combined with the very high ohmic loss, while at high frequencies this may also be an artifact due to the very high insertion loss leading to a signal dominated by noise. Furthermore, the absolute value of extracted L as shown in Figure 2.16 and 2.17 for the various dielectrics and line-lengths is larger than would be expected from electromagnetic calculations using SIMIAN (Surface Impedance Method for Interconnect Analysis) [46], which is a program for calculating the series impedance of two-dimensional multi-conductor interconnects and transmission lines using the Surface Ribbon Method developed by Microelectromagnetics Device Group under Dr. Dean P. Neikirk in the University of Texas at Austin. Specifically, the extracted L of longer lines (i.e., 8100μm and 11000μm line-lengths) is substantially larger than the calculated ones using SIMIAN.

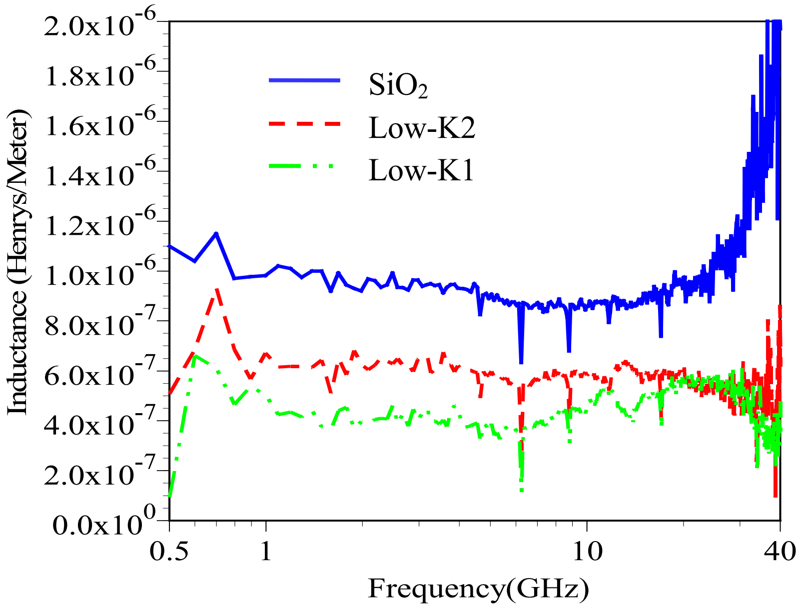

Figure 2.16: Extracted L per unit length of 0.25μm line-width and 3400μm line-length for various dielectrics.

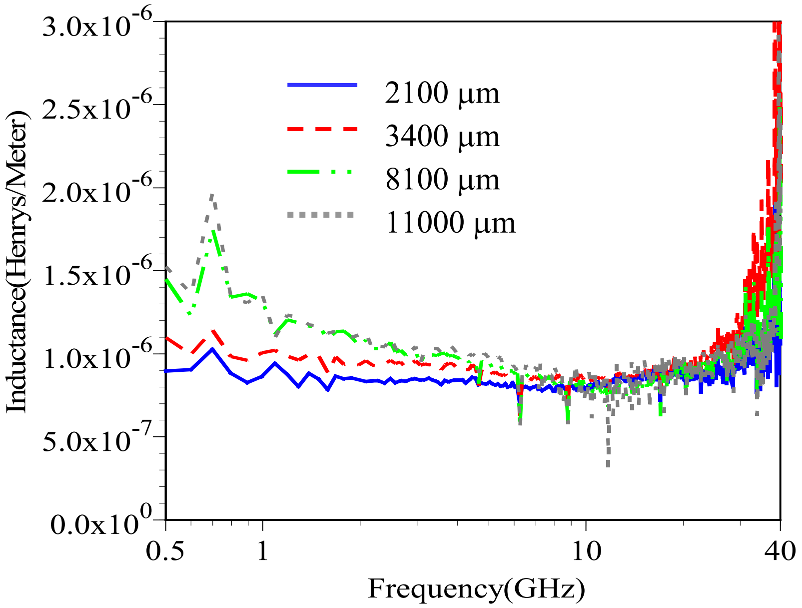

Figure 2.17: Extracted L per unit length of 0.25μm line-width of SiO_2 dielectric for various line-lengths.

The extracted C per unit length is quite frequency independent below 20GHz as shown in Figure 2.18 and 2.19. The roll-down or up for frequencies above 20GHz is again an artifact caused by the large insertion loss combined with noise. Since the nominal ratio (width / thickness of signal line) is smaller than 0.5 for 0.25µm and 0.175µm geometries, the fringing component becomes the dominant component. The extracted C for the 0.25µm and 0.175µm geometries is no longer a strong function of width due to the dominant fringing component of the electric fields.

The extracted G per unit length of different dielectrics is zero below 20GHz as shown in Figure 2.20. Hence, the dielectric loss for these materials is so low that it is rendered undetectable by the finite conductor loss, even for a 5µm line width. Again, the extracted G is below detection limit due to very high ohmic conductor loss compared to much lower dielectric loss combined with the impact of finite measurement precision at a low frequency. At high frequencies, extracted G is an artifact due to the very high insertion loss and the impact of finite measurement precision.

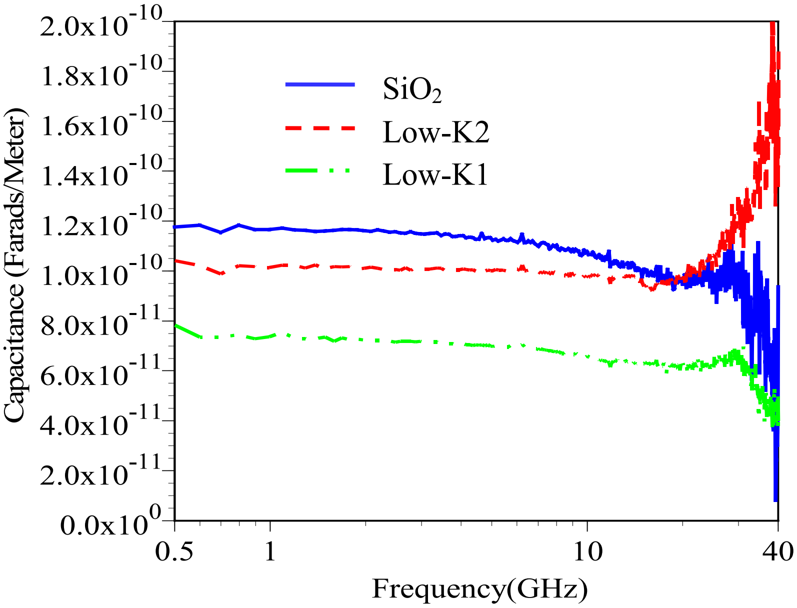

Figure 2.18: Extracted C per unit length of 0.25μm line-width and 3400μm line-length for various dielectrics.

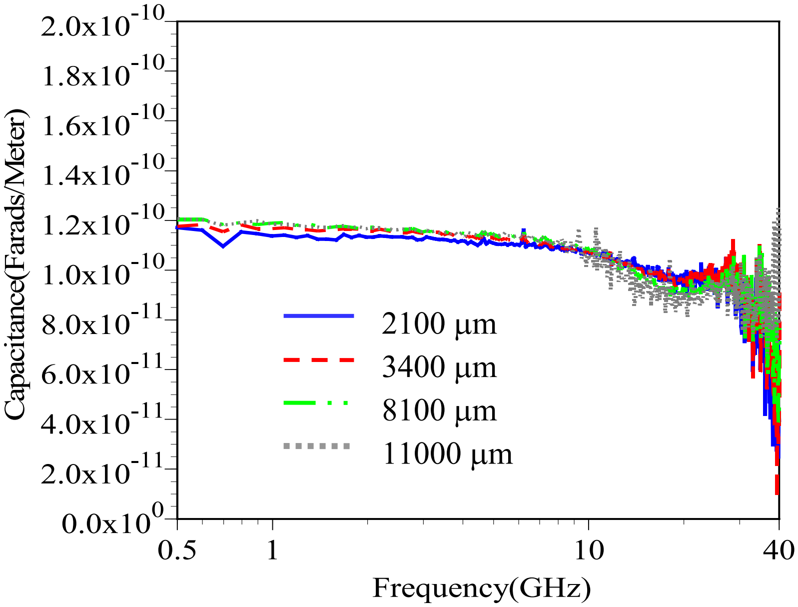

Figure 2.19: Extracted C per unit length of 0.25μm line-width of SiO_2 dielectric for various line-lengths.

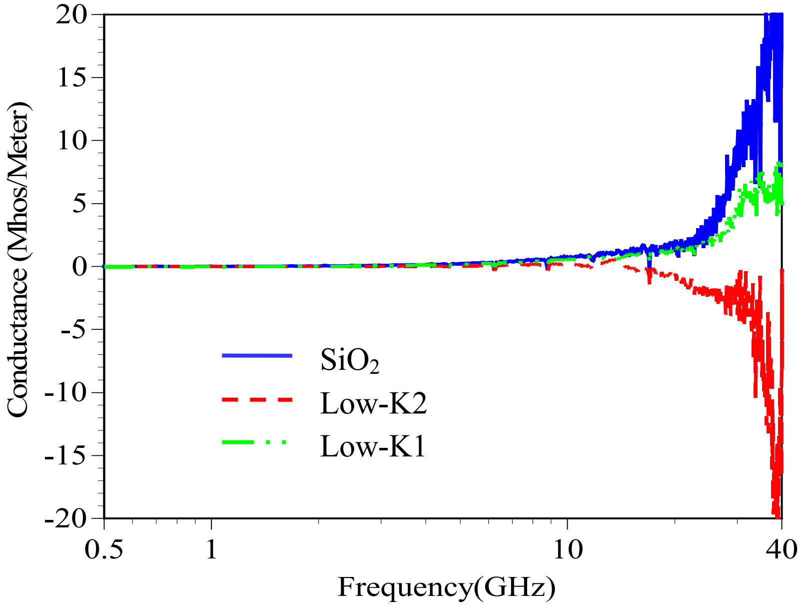

Figure 2.20: Extracted G per unit length of 0.25μm line-width and 3400μm line-length for various dielectrics.

The propagation constant (γ) describes how a signal propagates through the transmission line. Often, the propagation constant (γ) is broken down to real and imaginary parts. The real part, α, is commonly known as the attenuation constant because it determines how fast a signal on the line loses magnitude, and is a common measure of signal loss. The imaginary part, β, is referred to as the phase constant because it determines how the phase of the signal changes as it propagates through the transmission line. When considering transmission lines where signals only propagate in one direction, both attenuation constant (α) and phase constant (β) are defined to be non-negative.

Figure 2.21 (a) and (b) shows the attenuation constant (α) and phase constant (β) extracted from the propagation constant (γ) for 5μm and 0.25μm geometries of SiO_2 dielectric. The extracted the attenuation constant (α) and phase constant (β) appear to be identical to each other at frequencies below about 0.5GHz for 5μm geometry and 5GHz for 0.25μm geometry as shown in Figure 2.21 (a) and (b). This means a 5μm geometry at frequencies below about 0.5GHz could be characterized by the RC transmission line. And a 0.25μm geometry at frequencies below about 5GHz could be characterized by the RC transmission line. The extracted attenuation constant (α) and phase constant (β) have $\sqrt{\omega}$ dependences at frequencies less than 3GHz for 5μm geometry and 10GHz for 0.25μm geometry, which mean 5μm and 0.25μm geometries could well be modeled by an RC transmission. However, above 0.5GHz for 5μm geometry and 5GHz for 0.25μm geometry, the extracted attenuation constant and phase constant begin to split and have different slopes. The frequency at which the extracted attenuation constant and phase constant start to split varies with 5μm geometry and 0.25μm geometry (or 0.175μm geometry) of the transmission line as shown in Figure 2.21 (a) and (b), because the loss increases as the cross-sectional area decreases. Above about 5GHz, the line for 5μm geometry is an RLC transmission line.

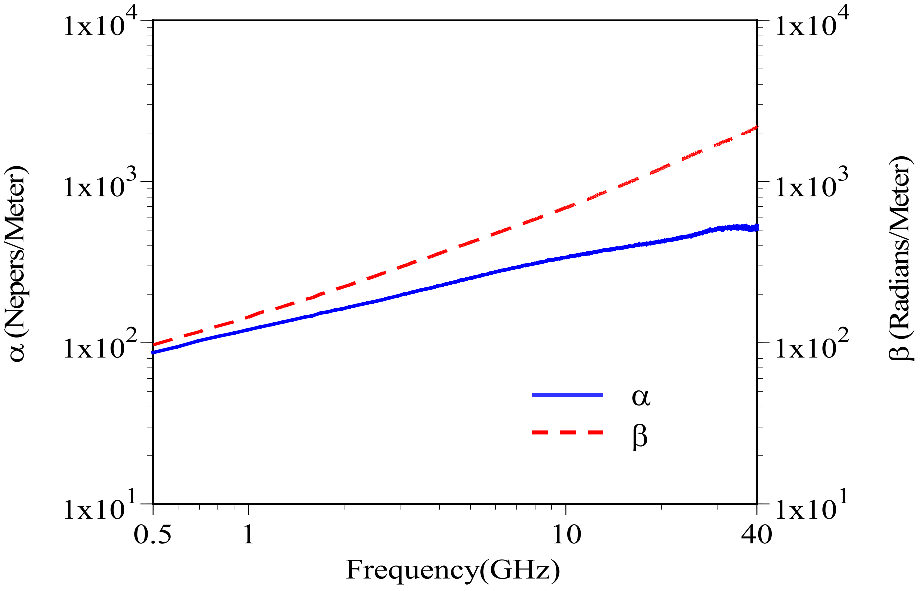

(a) 5μm geometry

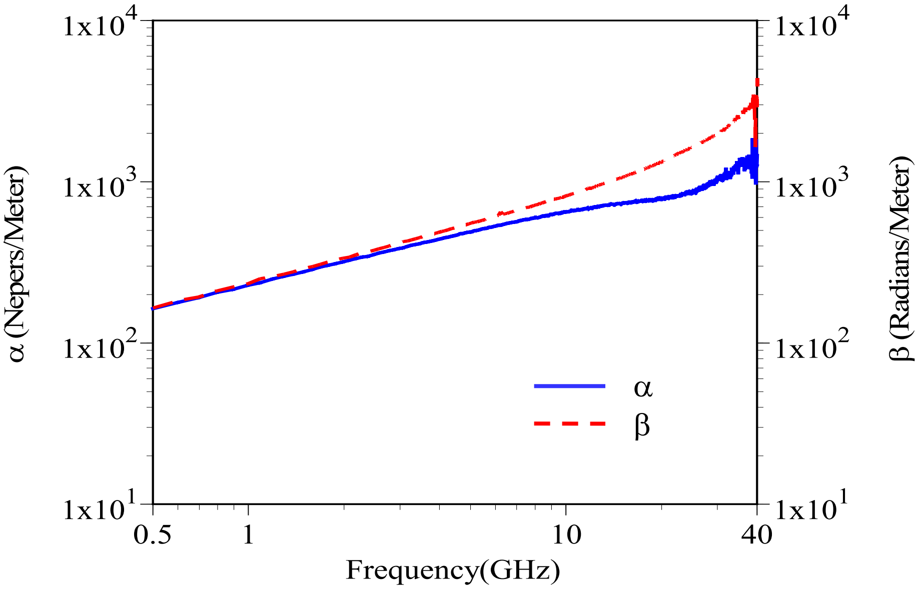

(b) 0.25μm geometry

Figure 2.21: Extracted attenuation constant (α) and phase constant (β) of different geometries of SiO_2 dielectric. (a) 5μm geometry: 5μm width and 4000μm line length (b) 0.25μm geometry: 0.25μm width and 3400μm line length

The relative importance of the extracted R and L for tested 5μm and 0.25μm geometries is shown in Figure 2.22 (a) and (b).

The extracted R for 5μm geometry of SiO_2 dielectric is dominant at low frequencies as shown in Figure 2.22 (a). At frequencies less than 1GHz, the extracted R is greater than 10 times ωL which implies that L does not contribute significantly to the series impedance. However, the ωL is comparable to the extracted R at frequencies above about 10GHz, which illustrates inductive effect is important. Hence, the inductive effects could not be significant at frequencies of less than about 5GHz.

The extracted R for 0.25μm geometry of SiO_2 dielectric is dominant at frequencies less than 10GHz as shown in Figure 2.22 (b). The ωL is comparable to the extracted R only for frequencies greater than above about 20GHz, which implies inductive effects are important. In the 0.175μm geometry, the extracted R of SiO_2 dielectric is also dominant at frequencies less than 10GHz, but ωL is comparable to the extracted R only for frequencies greater than above about 23GHz. Thus, the inductive effects could not be important at frequencies of less than about 10GHz.

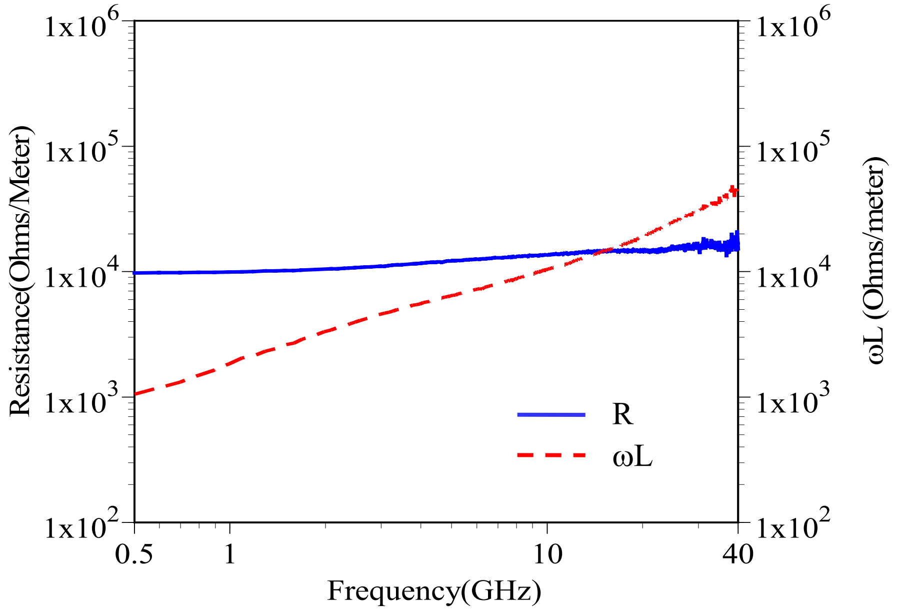

(a) 5µm geometry

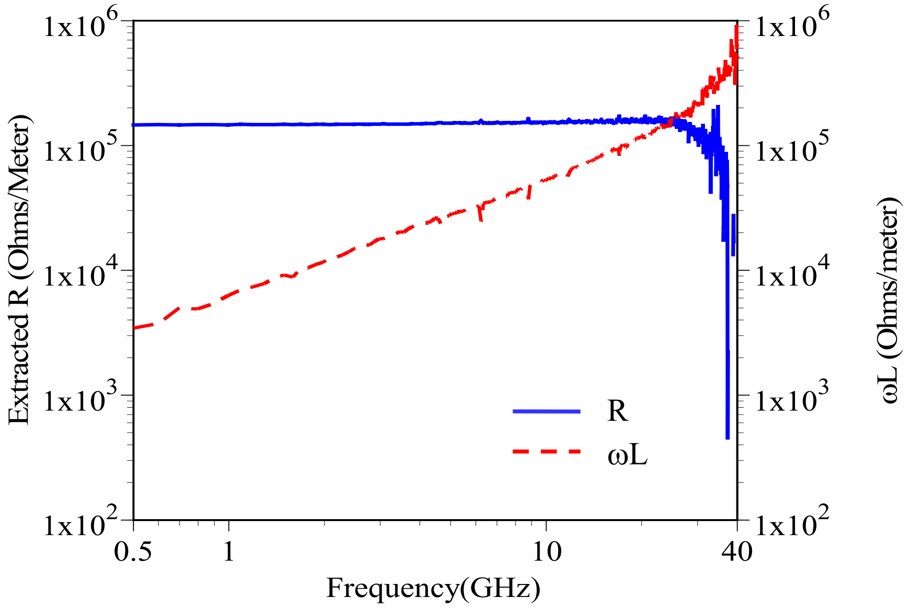

(b) 0.25µm geometry

Figure 2.22: Extracted R and ωL of different geometries of SiO_2 dielectric. (a) 5µm geometry: 5µm width and 4000µm line-length (b) 0.25µm geometry: 0.25µm width and 3400µm line-length

2.5. SUMMARY AND DISCUSSION

Characterization of dielectrics via one-port measurement using pad-only test structures could be summarized on the extracted dielectric constant and loss tangent. The extracted dielectric constant of SiO_2 is 4.2 to 4.4, low-k2 (Novellus' Coral low-k dielectric) is 3.1 to 3.3, and low-k1 (JSR Corp. low-k dielectric) is 1.75 to 2. Extraction of accurate loss tangents related to dielectric loss is very difficult due to high conductor loss for on-chip interconnects, even when using data from the shortest line length with the widest line width (1380μm length and 5μm width here). Furthermore, even for the large area pad-only test structure (50μm x 50μm in size), which produces much higher precision for extraction of loss tangent (tanδ) than do the transmission line test structures, the upper bound of the loss tangent was 0.02. Regardless, accurate extraction of the loss tangent is very difficult since the magnitude of conductor loss is much greater than dielectric loss; the measurements suggest the loss tangent is less than 0.01 for all the tested dielectrics. This indicates that the dielectric loss is insignificant compared to the conductor loss.

Extraction of line parameters for different geometries of transmission line with various dielectric thin films (SiO_2, low-k2 (Coral), and low-k1 (JSR)), various geometries (5μm, 0.25μm, and 0.175μm line-widths), and various line-lengths (i.e., varying length for each line-width) tested in this chapter has apparent non-physical frequency dependence at higher frequencies (i.e. over 20GHz). Frequency dependencies at higher frequencies (i.e. over 20GHz) seem due to the skin effect in the signal line because of the high frequencies involved. The equation for skin effect is given by

$$\delta = \frac{1}{\sqrt{\pi f \mu \sigma}} \tag{2.26}$$

where f is the frequency, μ is the permeability of the metal, and σ is the conductivity of the metal. At 40GHz for a copper line using bulk conductivity, the skin depth is 0.3μm. In this case, it is unlikely that the skin depth is important for any of the lines measured here because the thickness of the signal line (0.5μm) is less than two skin depths at the highest frequency. The apparent frequency dependence is likely due to another cause. Two possible causes of high frequency dependence in extracting line parameters are S-parameter errors such as magnitude detection limits and reference plane offset errors [29-31, 47], which will be presented in chapter 3 and 4, or using inadequate de-embedding network model of pads, which will be investigated in chapter 5.

Chapter 3

Impact of Error Propagation on the Extraction of Interconnect Parameters via Perturbation Analysis

The extracted per unit length resistance R, inductance L, capacitance C, and conductance G parameters shown in chapter 2 clearly indicated non-physical frequency dependences at the highest measurement frequencies. Examination of published data in the literature frequently shows similar behavior. A common interpretation of the apparent increase in the R parameter is that it is the result of the skin effect. For the deep submicron line dimensions and measurements frequencies below 50GHz, calculations of current redistribution do not support such a conclusion. A better explanation for the apparent frequency dependence in the extracted parameters at high frequencies is finite measurement accuracy and finite measurement precision. Furthermore, the finite errors in the calibration process and in the measurement procedure can also lead to non-physical frequency dependences at the highest measurement frequencies.

This chapter will focus on the finite measurement precision, specifically the finite errors, which might come from calibration procedures and measurements taken after calibration procedures were completed. The possible uncertainties will be length offset errors, essential reference plane offset errors due to different landing positions of wafer probes on pads [48], or Impedance Standard Substrate (ISS) during measurement and calibration. In addition some measurement uncertainties are systematic errors in the S-parameters from the network analyzer. These errors affect the extracted RLCG parameters from the high frequency measurements. In order to investigate the effect of measurement uncertainties, the extracted R, L, C, and G parameters from measurements should be compared to the perturbed R, L, C, and G parameters, which account for the measurement errors. Since perturbation analysis allows errors introduced into the frequency independent RLCG parameters without any errors, the perturbed RLCG parameters can identify the error source and improve measurements and the extraction of parameters. Hence, in chapter 3 the impact of these possible uncertainties will be investigated using the simulation with perturbation technique.

3.1 TYPES OF ERRORS

Measurement errors can occur from many different sources. These errors can affect both magnitude and phase of the S-parameters. In this chapter we will investigate the magnitude error, which is the magnitude limit error (minimum magnitude detectable signal level), and the phase errors, which are finite phase measurement precision errors (essentially a round-off error in the phase) and length offset error (reference plane offset). In addition the impact of wrong estimation for pad capacitance in an assumed lumped RC network model of pads as shown in previous chapter, which might come from the process variation of die to die or pad-only test structure to pad-only test structure, will be estimated in this section.

A VNA in different high frequency measurement set-ups has different dynamic ranges of VNA in that set-up. A VNA in those measurement setups cannot detect signals correctly below a given minimum amplitude (i.e., beyond dynamic range). All measured signals below the minimum level will not be detected correctly. The dominant uncertainty of the magnitude is magnitude limit error (minimum magnitude detectable signal level), which is the dominant error for very lossy transmission lines, such as the

0.25μm geometry and 0.175μm geometry. This error is also dependent on the line-length. For the lines under consideration, the magnitude of S_{21} always decreases as frequency increases because of the high loss in the line, but the magnitude of S_{11} is large over the entire frequency range and is never affected by the magnitude detection limit. For our measurement set-up, the optimistic minimum signal level is – 80dB, but the realistic minimum level is – 60dB. Hence, VNA for our measurement set-up cannot detect signals under –60dB, which can also be verified from the raw measurement data of S-parameters (example: Figure 3.1: 0.25μm width/11000μm line-length test structure of SiO_2 dielectric). Figure 3.1 illustrates that for the long (11000μm) line-length and 0.25μm line-width the loss is so high that no meaningful extraction can be performed for frequencies above about 5GHz. Since the considered geometry (i.e., 0.25μm line-width and 2100μm line-length) in the simulation cannot be affected by magnitude limit error based on measured raw S-parameter, this error (i.e., magnitude limit error) will not be considered in the perturbation simulation.

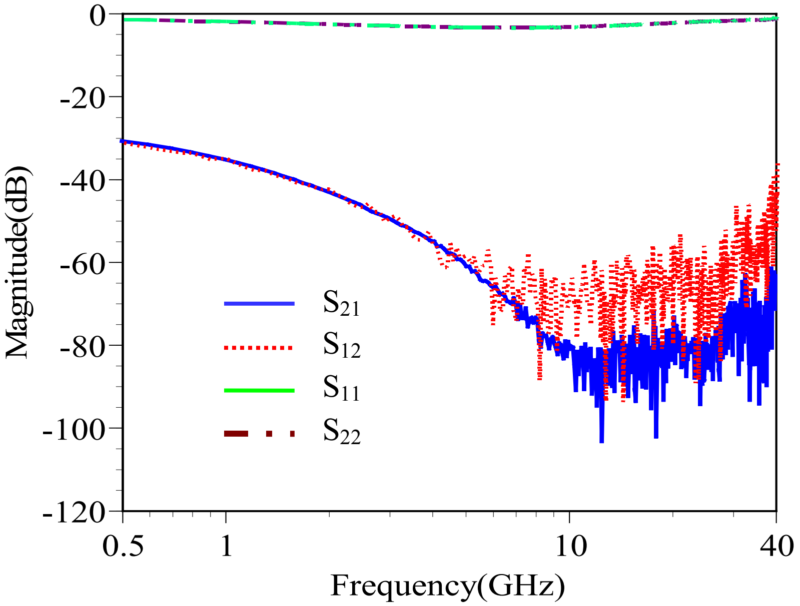

(a) Extracted Magnitude

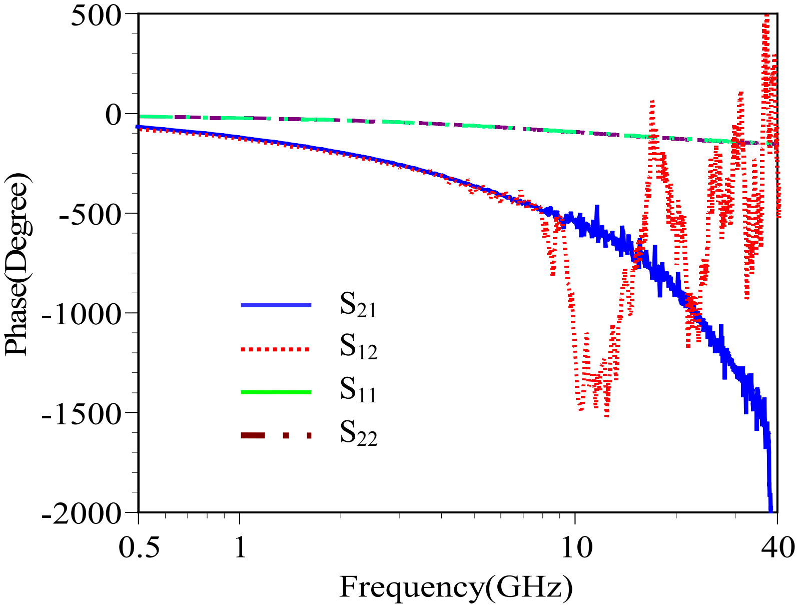

(b) Extracted Phase

Figure 3.1: Magnitude and phase of measured S-parameters, showing that for the long (11000μm) line-length and 0.25μm line-width the loss is so high that no meaningful extraction can be performed for frequencies above about 5GHz.

One of the phase errors is “Round-off” error, which is caused by the finite precision with which the phase of S-parameters can be measured. For example the finite precision for the HP 8510C network analyzer is 0.01° at favorable conditions according to the documentation from [49, 50]. For the geometries considered here, the absolute value of the phase of S_{11} and S_{21} increases as the frequency increases. This indicates the round-off error is a big effect for low frequencies because the phase of S-parameters is small. However, the round-off phase error can be a small effect for high frequencies. Hence, the round off phase error cannot explain the non-physical high frequency dependencies of extracted parameters shown in chapter 2. Thus round-off phase error will not be considered in the perturbation simulation because we could not evaluate the measurement errors at the high frequencies.

Another source of phase error is “Reference plane offset” error. Basically, this can occur whenever the setup changes between calibration and measurement. Furthermore, both the inconsistent probe landing position on wafer pads during measurement and the incorrect landing position on standard patterns on ISS (i.e., Short, Load, and Thru patterns on ISS) during calibration procedures can produce a certain amount of reference plane offset error. If the reference plane offset error occurs, all measurements will have some amount of the phase error because the reference plane of the effective DUT will be added to or subtracted from the actual DUT. This length offset error will have its own frequency dependent S-parameters which can, when cascaded with the S-parameters of the desired DUT, have a small or large effect depending on the frequency and actual DUT. As a result, the phase shift due to length offset error is linearly dependent on frequency. This indicates that the reference plane offset error is a greater problem at higher frequencies. Hence, this error will be focused on the perturbation analysis for investigating the non-physical high frequency dependencies from extracted RLCG parameters as presented in chapter 2.

Since the impact of wrong estimation for pad capacitance (C_{pad}) is similar to that of a length offset error, we will consider another error as the wrong estimation for pad capacitance (C_{pad}), which was extracted from a one-port measurement of a pad-only structure, in an assumed RC network model of pads. Since it is not possible to characterize pads connected to the tested transmission line at both ends, we did use separate pad-only test structure only to de-embed pad parasitics for characterizing the transmission line. As described in chapter 2, the amount of pad parasitics (i.e., C_{pad}) is as large as the signal line capacitance; therefore, C_{pad} should be de-embedded correctly based on the assumed network model. However, the extracted pad capacitance (C_{pad}) from a one-port measurement may different from die to die and pad-only test structure to pad-only test structure due to the fabrication process variation. Furthermore, the calculated pad capacitance (C_{pad}) may also not be correct because we cannot eliminate the dimensional uncertainties completely, even using SEM after manufacturing. Therefore, the wrong estimation of pad capacitance (C_{pad}) on the assumed lumped RC network model will be considered in perturbation simulation for investigating the non-physical high frequency dependencies from extracted RLCG parameters.

3.2 METHODOLOGY

The Devices Under Test (DUTs) in this section are embedded microstrip transmission lines of 0.25μm line-width for 2100μm line-length and 8100μm line-length using a SiO_2 inter-level dielectric, which have the same cross-sectional geometries introduced in chapter 2. These test structures have 0.5μm thick signal conductors (metal level 2, M2) and 0.4μm separation of signal (on M2) to ground (located on metal level 1, M1), as shown in Figure 2.2. In addition, a simple probe pad-only test structure consists of ground-signal-ground co-planar metal squares, 50μm x 50μm in size. The ground pads are connected to the ground plane (M1) by using vias (metal 1 (M1)-to-metal 2 (M2) contacts), as shown in Figure 2.1. The test structures for both pad-only and embedded microstrip transmission lines are located on a common die, and were fabricated at SEMATECH. To illustrate the impact of error propagation issues in this chapter, we will only consider the SiO_2 dielectric.

Figure 3.2 describes the simulation procedure using perturbation techniques with measurement uncertainties. To investigate the impact of the measurement uncertainties, specifically length offset error on the extracted R, L, C, and G parameters via the perturbation simulation technique, frequency independent R, L, C, and G parameters are assumed (to match the low or mid range frequency measured values) and then are used with the nominal (mask drawn) line length. The complex propagation constant (γl) and complex characteristic impedance (Z_o) are calculated from the assumed R, L, C, G, and nominal line length using Equation (3.1) and (3.2).

$$\gamma l = \sqrt{(R + j\omega L)(G + j\omega C)} \times l \tag{3.1}$$

$$Z_o = \sqrt{\frac{(R + j\omega L)}{(G + j\omega C)}} \tag{3.2}$$

Then, the complex propagation constant (γ) and complex characteristic impedance (Z_o) can be converted to the S-parameters of the transmission line with reference to $50\,\Omega$ test ports (i.e., Z_{port} equals to 50Ω) using Equation (3.3). Since transmission lines are symmetrical and reciprocal networks, S_{11} equals S_{22}, and S_{21} equals to S_{12}.

$$\begin{bmatrix} S_{11} & S_{12} \\ S_{21} & S_{22} \end{bmatrix}_{line-only} =$$

$$\begin{bmatrix} \dfrac{(Z_o^2 - Z_{port}^2)\sinh\gamma l}{(Z_o^2 + Z_{port}^2)\sinh\gamma l + 2Z_{port}Z_o\cosh\gamma l} & \dfrac{2Z_{port}Z_o}{(Z_o^2 + Z_{port}^2)\sinh\gamma l + 2Z_{port}Z_o\cosh\gamma l} \\ \dfrac{2Z_oZ_{dut}}{(Z_o^2 + Z_{port}^2)\sinh\gamma l + 2Z_{port}Z_o\cosh\gamma l} & \dfrac{(Z_{dut}^2 - Z_o^2)\sinh\gamma l}{(Z_o^2 + Z_{port}^2)\sinh\gamma l + 2Z_{port}Z_o\cosh\gamma l} \end{bmatrix} \tag{3.3}$$

Next, S-parameters for the transmission line only are converted to ABCD parameters for the transmission line only using Equation (3.4) [40].

$$\begin{bmatrix} A & B \\ C & D \end{bmatrix}_{line-only} =$$

$$\begin{bmatrix} \dfrac{(1+S_{11})\times(1-S_{22})+S_{12}\times S_{21}}{2S_{21}} & Z_{port}\times\dfrac{(1+S_{11})\times(1+S_{22})-S_{12}\times S_{21}}{2S_{21}} \\ \dfrac{1}{Z_{port}}\times\dfrac{(1-S_{11})\times(1-S_{22})-S_{12}\times S_{21}}{2S_{21}} & \dfrac{(1-S_{11})\times(1+S_{22})+S_{12}\times S_{21}}{2S_{21}} \end{bmatrix} \tag{3.4}$$

After the S-parameters of a given transmission line and pad-only structures are converted to ABCD parameters [40], total ABCD parameters, which allow the cascading of networks by the multiplication of the ABCD parameters for pads at both ends of ABCD to transmission line only at the middle, are shown in Equation (3.5).

$$\begin{bmatrix} A & B \\ C & D \end{bmatrix}_{total} = \begin{bmatrix} 1 & Z_{contact} \\ 0 & 1 \end{bmatrix} \begin{bmatrix} 1 & 0 \\ Y_{pad} & 1 \end{bmatrix} \begin{bmatrix} A & B \\ C & D \end{bmatrix}_{line-only} \begin{bmatrix} 1 & 0 \\ Y_{pad} & 1 \end{bmatrix} \begin{bmatrix} 1 & Z_{contact} \\ 0 & 1 \end{bmatrix} \tag{3.5}$$

The effect of pads are then added as shown in total ABCD parameters, and the calculated total S-parameters shown in Equation (3.6) are perturbed by a systematic length offset error (reference plane offset error). Treating the amount of length offset error as a parameter enables us to examine the error propagation that could be caused by different probe placements on the on-wafer probe pads during measurement procedures.

$$\begin{bmatrix} S_{11} & S_{12} \\ S_{21} & S_{22} \end{bmatrix}_{total} =$$

$$\begin{bmatrix} \dfrac{A_{total} + \dfrac{B_{total}}{Z_{port}} - C_{total}Z_{port} - D_{total}}{A_{total} + \dfrac{B_{total}}{Z_{port}} + C_{total}Z_{port} + D_{total}} & \dfrac{2(A_{total}D_{total} - B_{total}C_{total})}{A_{total} + \dfrac{B_{total}}{Z_{port}} + C_{total}Z_{port} + D_{total}} \\ \dfrac{2}{A_{total} + \dfrac{B_{total}}{Z_{port}} + C_{total}Z_{port} + D_{total}} & \dfrac{-A_{total} + \dfrac{B_{total}}{Z_{port}} - C_{total}Z_{port} + D_{total}}{A_{total} + \dfrac{B_{total}}{Z_{port}} + C_{total}Z_{port} + D_{total}} \end{bmatrix} \quad (3.6)$$

After calculation and perturbation, the perturbed total S-parameters are converted back to the perturbed total ABCD parameters, and then the pad-only test structures at both ends are de-embedded. Afterwards, the perturbed ABCD parameters of the transmission line only are extracted as shown in Equation (3.7). Finally, the perturbed ABCD parameters of the transmission line only are converted back to the perturbed γl and Z_o of the transmission line only using Equation (3.8), and the "perturbed" R, L, C, and G parameters are determined as described in Equation (3.9) to (3.12). These parameters can then be compared to actual experimentally measured and extracted parameters.

$$\begin{bmatrix} A & B \\ C & D \end{bmatrix}_{PERT-line} = \begin{bmatrix} 1 & 0 \\ Y_{pad} & 1 \end{bmatrix}^{-1} \begin{bmatrix} 1 & Z_{contact} \\ 0 & 1 \end{bmatrix}^{-1} \begin{bmatrix} A & B \\ C & D \end{bmatrix}_{PERT-total} \begin{bmatrix} 1 & Z_{contact} \\ 0 & 1 \end{bmatrix}^{-1} \begin{bmatrix} 1 & 0 \\ Y_{pad} & 1 \end{bmatrix}^{-1} \quad (3.7)$$

$$\begin{bmatrix} A & B \\ C & D \end{bmatrix}_{PERT-line} = \begin{bmatrix} \cosh \gamma_{PERT} l & Z_{o-PERT} \sinh \gamma_{PERT} l \\ \dfrac{\sinh \gamma_{PERT} l}{Z_{o-PERT}} & \cosh \gamma_{PERT} l \end{bmatrix} \quad (3.8)$$

$$R_{PERT} = \mathrm{Re}\left\{\gamma_{PERT} Z_{o-PERT}\right\} \tag{3.9}$$

$$L_{PERT} = \mathrm{Im}\left\{\gamma_{PERT} Z_{o-PERT}\right\} / \omega \tag{3.10}$$

$$C_{PERT} = \mathrm{Im}\left\{\gamma_{PERT} / Z_{o-PERT}\right\} / \omega \tag{3.11}$$

$$G_{PERT} = \mathrm{Re}\left\{\gamma_{PERT} / Z_{o-PERT}\right\} \tag{3.12}$$

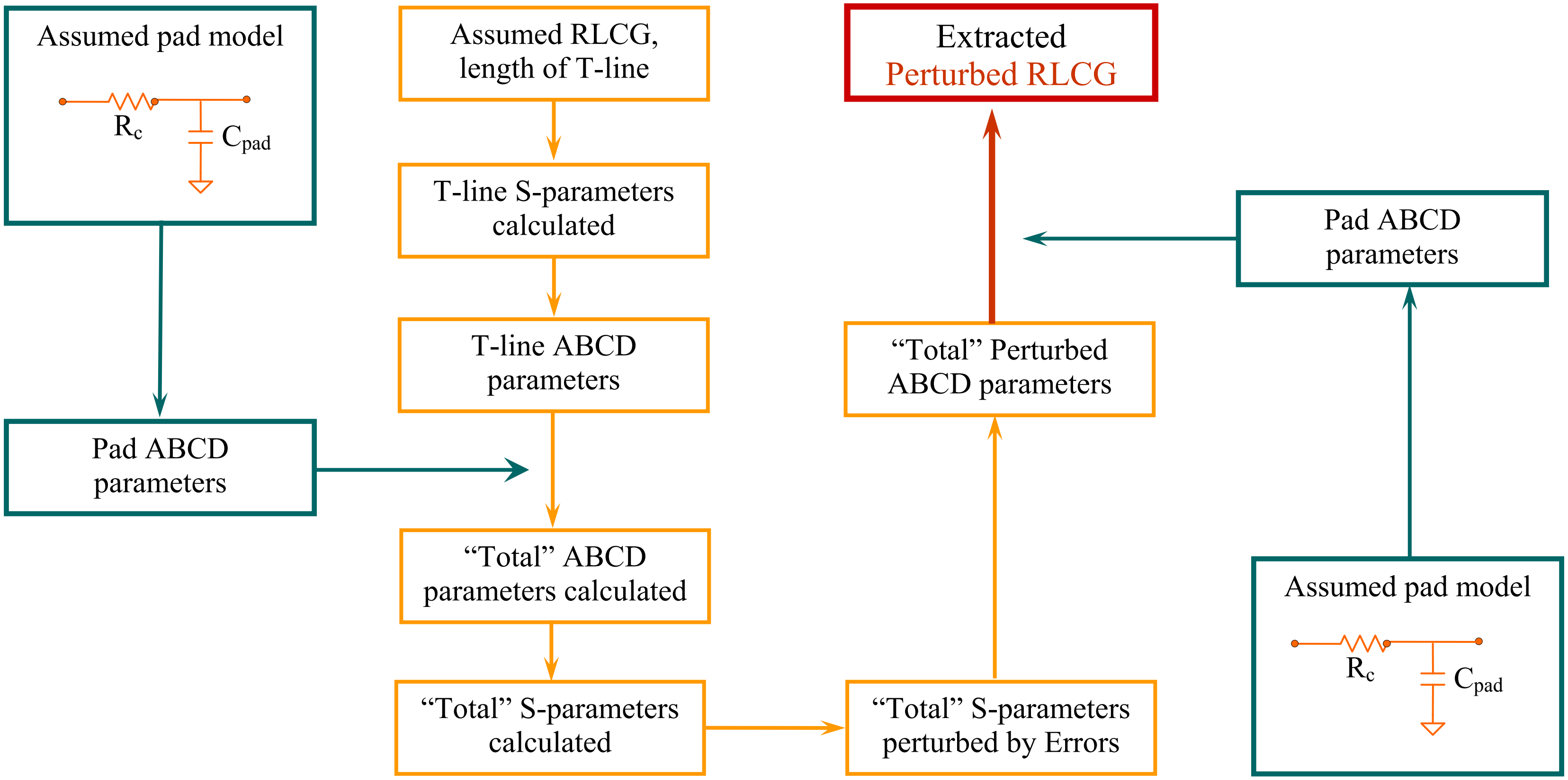

Figure 3.2: The simulation procedure using perturbation techniques with measurement uncertainties.

3.3 SIMULATION RESULTS

As a part of error propagation analysis on RLCG extraction for high frequencies, the purpose of perturbation analysis is to investigate the impact of the systematic errors in measurement on RLCG extraction. The impact of the systematic errors on RLCG extraction was evaluated by examining: 1) different length offset errors (± 50μm and ± 100μm length offset errors) for 0.25μm geometry with 2100μm line length transmission line, 2) different line length transmission lines (2100μm and 8100μm) of 0.25μm geometry with the same length offset error (± 50μm length offset errors), 3) and the wrong estimation of pad capacitance (± 5% and ± 10% based on the mean value of the extracted C_{pad} from a one-port measurement for pad-only test structures of multiple dies) in an assumed RC network model for 0.25μm geometry with 2100μm line length transmission line.

As a result of the perturbation analysis, the R, L, C, and G extracted from the perturbed S-parameters with different length offset errors and without any other errors for 0.25μm geometry with 2100μm line length transmission line are shown in Figure 3.3, Figure 3.5, Figure 3.7, and Figure 3.9, respectively. In addition the perturbed R, L, and C for different line-lengths with the same length offset errors (± 50μm length offset errors) are shown in Figure 3.4 Figure 3.6, and Figure 3.8, respectively.

As shown in Figure 3.3, the perturbed R is mostly affected at high frequencies with the different length offset errors of ± 50μm and ± 100μm. Below 5GHz, the perturbed R for all considered length offsets is pretty much frequency independent, which means the impact of the length offset error is so small that any frequency dependencies cannot be detected in low frequencies for the considered test structures. However, above 5GHz, the perturbed R for all considered length offset errors (± 50μm and ± 100μm) has non-physical frequency dependencies, which specifically indicate the perturbed R decreases in high frequency ranges. In addition, the large offset (i.e., ± 100μm length offset) causes the roll-off to start at a lower frequency and produces larger errors. Positive length offsets, +50μm and +100μm, make a similar extracted R as the current redistribution in frequency ranges (i.e., 5GHz to 20GHz), although the extracted R decreases over 20GHz. As described in chapter 2, the exhibited frequency dependency might be not skin effect, but length offset error for the considered geometries.

The effect of differing line lengths under the same length offset errors (± 50μm length offset errors) is illustrated in Figure 3.4. The effect of differing line lengths for perturbed R is so small at low frequencies that the extracted R is frequency independent at low frequencies. The line-length dependence on the length offset error (± 50μm length offsets) in extracted R is less obvious at high frequencies. The longer transmission line (8100μm line-length) has smaller errors than the shorter transmission line (2100μm line-length) for the positive 50μm length offset at high frequencies. The longer transmission line (8100μm line-length) has the roll-off start at a lower frequency and produces a bigger error compared to the shorter transmission line (2100μm line-length) for the negative 50μm length offset at high frequencies.

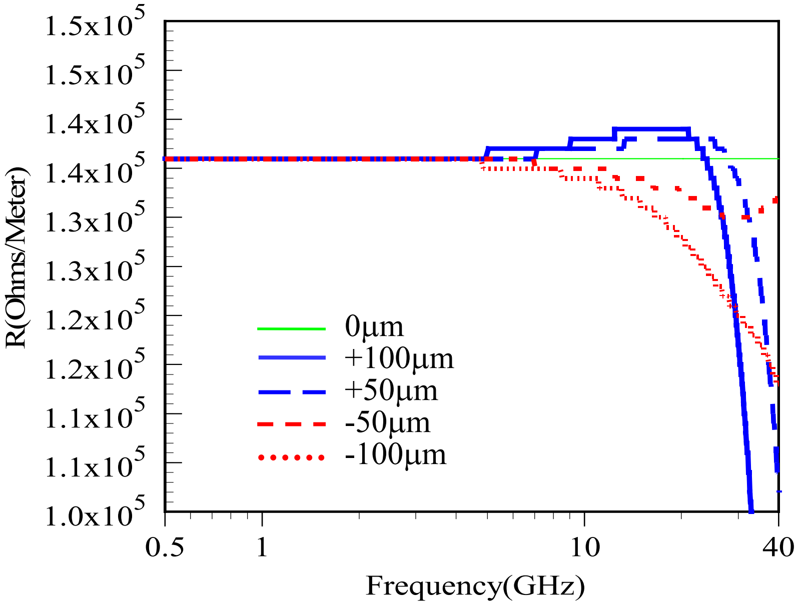

Figure 3.3: Perturbed R per unit length of 0.25µm width and 2100µm line length with 0µm (i.e., without length offset error), ± 50µm, and ± 100µm length offsets.

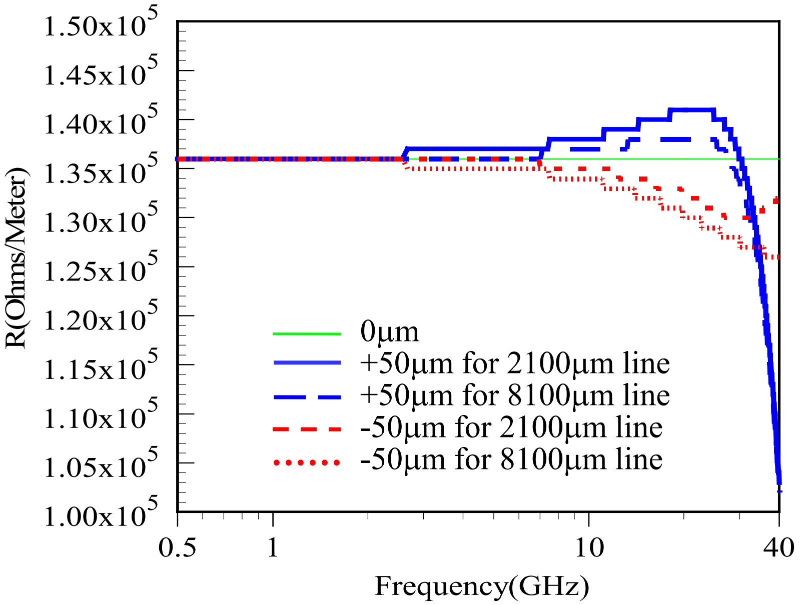

Figure 3.4: Perturbed R per unit length of 2100µm and 8100µm line length of 0.25µm width with 0µm (i.e., without length offset error), and ± 50µm length offsets.

The perturbed L is mostly affected at high frequencies with the different length offset errors: ± 50μm and ± 100μm length offsets, as shown in Figure 3.5.

The larger length offset errors (± 100μm here) produce larger errors in both low and high frequencies. In low frequencies the impact of error for smaller length offsets (± 50μm here) is only 2% and 6% for larger length offsets (± 100μm here). Above 30GHz the error for smaller length offsets is 32%, and 70% for larger length offset errors. Thus, these indicate that the larger length offset errors produce larger errors in both low and high frequencies in extracting L, and the impact of the length offset error in extracting L is much bigger at high frequencies than at low frequencies.

A longer transmission line (8100μm line-length) has more error than a shorter transmission line (2100μm line-length) in the extracted inductance at low and high frequencies, as shown in Figure 3.6. Specifically, the perturbed L for the longer line (8100μm line-length) at the lowest frequency is 15% of maximum error, whereas the perturbed L for the shorter line (2100μm line-length) is only 2% in error. In the highest frequency the error is about 30% for both longer and short lines, an even longer line has slightly more error.

Similarly, length offset error has a bigger effect on high frequencies; however, the L, extracted from perturbed S-parameters, also has an effect on low frequencies, specifically there is more error for longer lines.

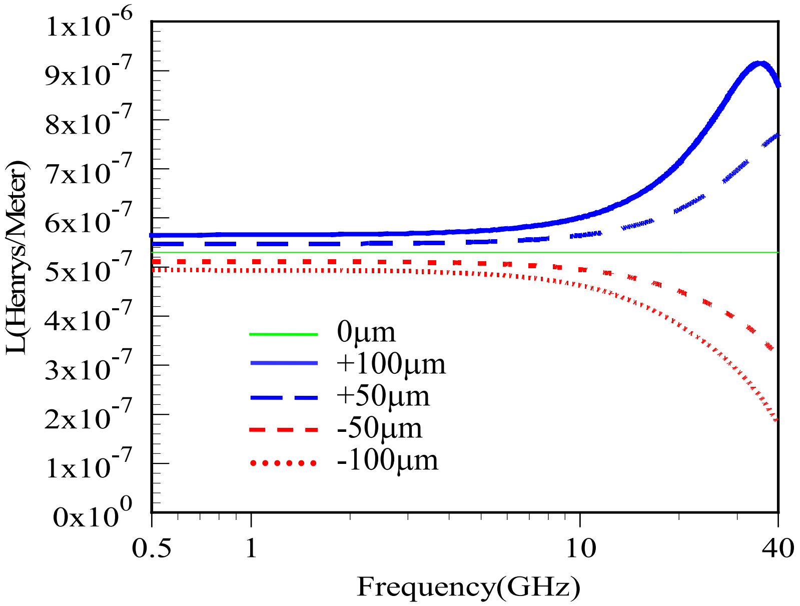

Figure 3.5: Perturbed L per unit length of 0.25µm width and 2100µm line length with 0µm (i.e., without length offset error), ± 50µm, and ± 100µm length offsets.

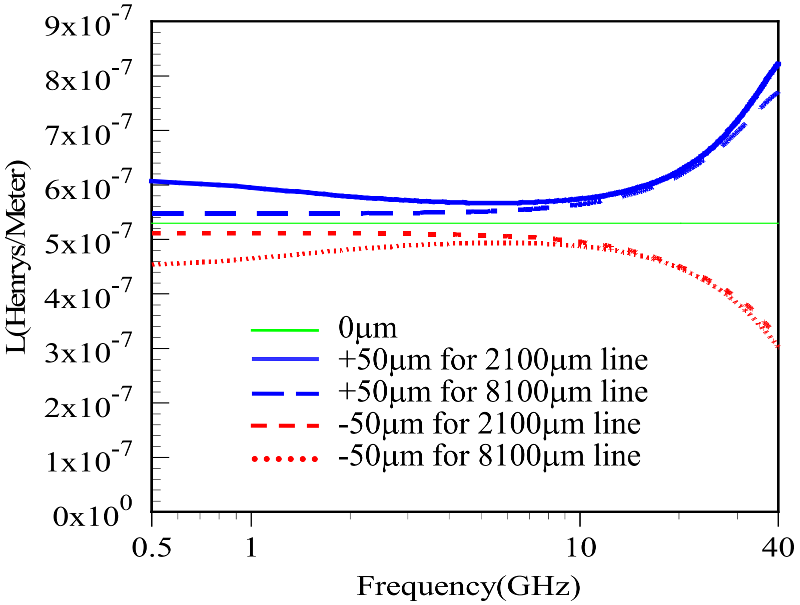

Figure 3.6: Perturbed L per unit length of 2100µm and 8100µm line length of 0.25µm width with 0µm (i.e., without length offset error), and ± 50µm length offsets.

The perturbed C is affected the most at high frequencies with the different length offset errors, ± 50μm and ± 100μm length offsets, as shown in Figure 3.7.

In all cases of the considered length offsets, the perturbed C illustrates a frequency dependent roll-up or down that might not be present in the actual capacitance. The large length offsets (i.e., ± 100μm here) cause the roll-off to start at a lower frequency (about 10GHz) and also causes larger errors at the higher frequency. The error at lowest frequency is about only 4% for both ± 50μm and ± 100μm length offsets. This means the impact of length offset error for extracted C at the lowest frequency is fairly small, thus C could be extractable with these errors at the low frequency region. However, the maximum error at the highest frequency is 70% for larger length offsets (i.e., ± 100μm here), and 30% for smaller length offsets (i.e., ± 50μm here). Again, it is obvious that the larger length offset error, the bigger the impact on extracted C. Furthermore, the length offset error could produce a bigger effect on the extracted C at the high frequency region.

A longer transmission line (8100μm line-length) has slightly more error than a shorter transmission line (2100μm line-length) in the extracted capacitance at high frequencies, as shown in Figure 3.8. However, the extracted C for both shorter and longer line indicates that the impact of error on the extracted C does not look much different, even at highest frequencies. At 40GHz the error of extracted C for the longer line is about 34.6%, while the error for the shorter line is about 30.7%. In addition, the impact of length offset error for line-length difference does not have much effect on low frequencies for extracted C.

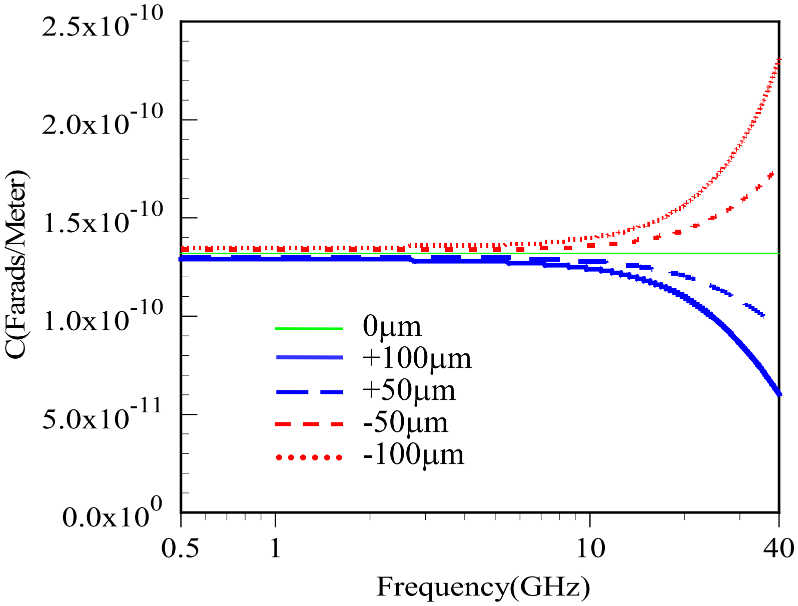

Figure 3.7: Perturbed C per unit length of 0.25μm width and 2100μm line length with 0μm (i.e., without length offset error), ± 50μm, and ± 100μm length offsets.

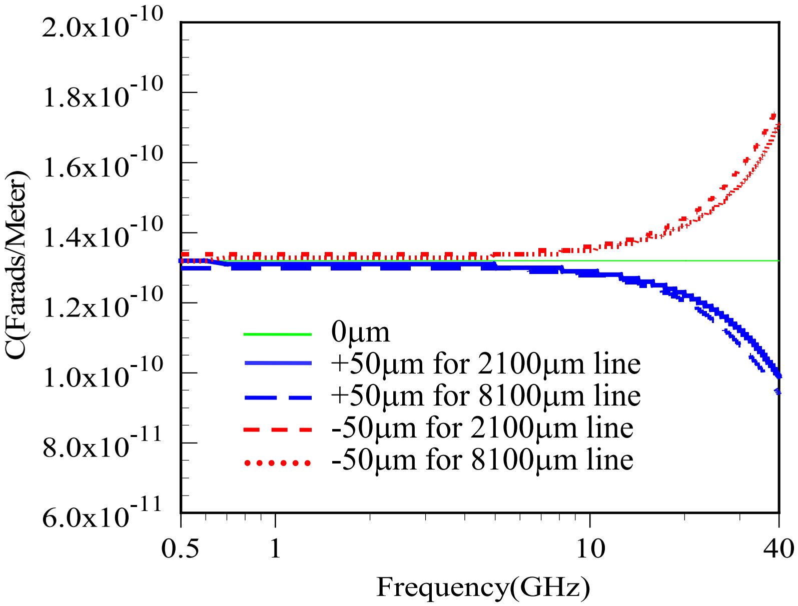

Figure 3.8: Perturbed C per unit length of 2100μm and 8100μm line length of 0.25μm width with 0μm (i.e., without length offset error) and ± 50μm length offsets.

The perturbed G is mostly affected at high frequencies with the different length offset errors, ± 50µm and ± 100µm length offset, as shown in Figure 3.9. The larger length offsets (± 100µm length offsets) have a large effect on the extracted R, L, and C for the considered transmission line as shown in Figure 3.3, Figure 3.5, and Figure 3.7, respectively. Not surprisingly, the larger the length offsets, the bigger the error at high frequencies for extracted G. The error is nearly 1500% at 40GHz for larger length offset errors, while the small length offset errors (± 50µm length offsets) have 800% error at the highest frequency. At low frequencies the error is much smaller (less than about 0.1% below 15GHz), thus, it is not visually noticeable for either smaller or larger length offset errors under 15GHz.

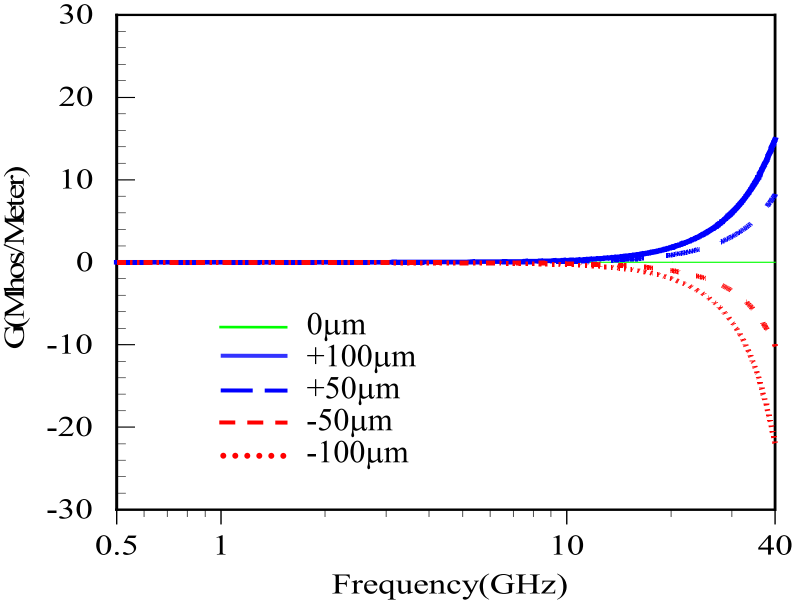

Figure 3.9: Perturbed G per unit length of 0.25µm width and 2100µm line length with 0µm (i.e., without length offset error), ± 50µm, and ± 100µm length offsets.

The impact of wrong estimation for pad capacitance is similar to that of a length offset error except the different pad capacitance (C_{pad}) affects both magnitude and phase of the S-parameters. The considered geometry is 0.25μm wide and 2100μm line length, and multiple 50μm x 50μm in-sizes of separate on-wafer pad-only test structures are used to acquire the mean of pad capacitance for multiple dies and multiple pad structures. The extracted mean value for pad capacitance on SiO_2 dielectric from a one-port measurement for multiple die with the nominal geometries equals to 2.4×10^{-13}[F]. Based on the mean value from the multiple measurements, we did test the impact of the wrong estimation of C_{pad} with ± 5% and ± 10% from the mean.

The impact of wrong estimation of C_{pad} on RLCG extraction of 0.25μm geometry and 2100μm line length transmission line is illustrated in Figure 3.10, Figure 3.11, Figure 3.12, and Figure 3.13, respectively.

The impact of the C_{pad} difference on RLCG extraction is similar to that of length offset error except for the extracted L; the error increases in the high frequencies. The extracted R is affected the most at high frequencies with different amounts of pad capacitance, similar to that of length offset errors, as shown in Figure 3.10. Below 5GHz, the extracted R for the C_{pad} difference does not have any effect on R extraction. However, above 5GHz, the extracted R for overestimated pad capacitance (+5% and +10% C_{pad} of extracted mean value from a one-port measurement) has non-physical frequency dependencies. On the other hand, the extracted R for underestimated pad capacitance (-5% and -10% C_{pad} from mean) behave like the current redistribution in frequency ranges (i.e., 5GHz to 30GHz), but as mentioned in chapter 2, the exhibited frequency dependency might be not skin effect, but the wrong estimation of pad capacitance or length offset error for the considered geometries.

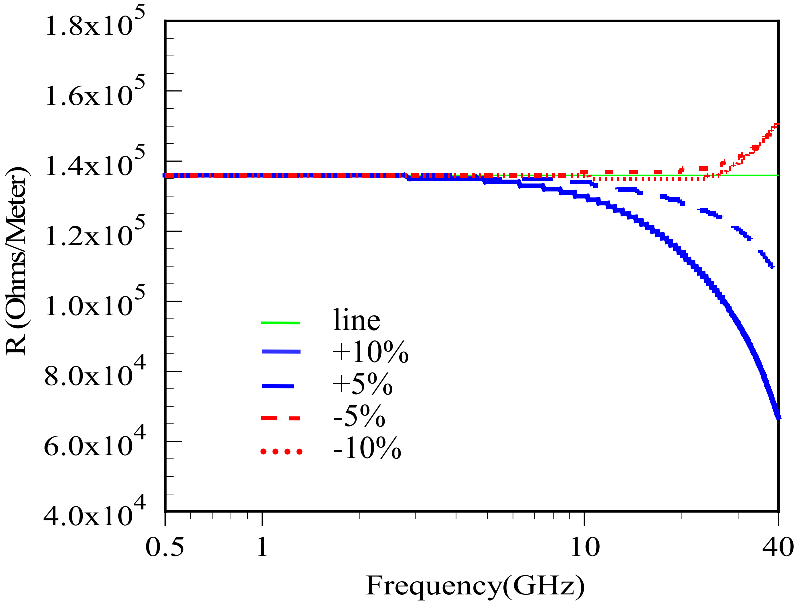

Figure 3.10: Perturbed R per unit of 0.25μm width and 2100μm line length with mean, ± 5%, and ± 10% from the mean of the extracted pad capacitance (C_{pad}).

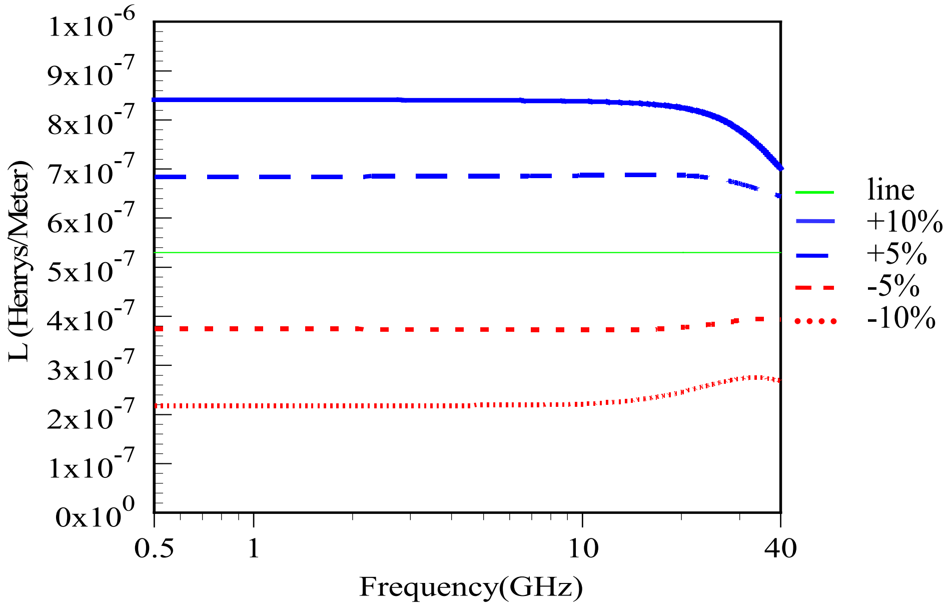

Figure 3.11: Perturbed L per unit of 0.25μm width and 2100μm line length with mean, ± 5%, and ± 10% from the mean of the extracted pad capacitance (C_{pad}).

As shown in Figure 3.11, the errors on L extraction for the different pad capacitance in the lowest frequency are +28% and +58% for +5% and +10% of C_{pad} from the mean. In the highest frequency the errors decrease on L extraction, specifically, +23% for ±5% of C_{pad} from the mean and +36% for ±10% of C_{pad} from the mean. Thus the impact of the wrong estimation of C_{pad} on L extraction is bigger in lower frequencies, rather than in higher frequencies.

The larger C_{pad} difference has a bigger effect on the extracted C as shown in Figure 3.12. Specifically, the extracted C for the C_{pad} difference in the lowest frequency is about -10% and -20% for +5% and +10% of pad capacitance from the mean, respectively. Figure 3.12 indicates that the overestimated / underestimated pad capacitance at either end (i.e., ±5% and ±10% at either end of the transmission line) in de-embedding network model at low frequencies produce underestimated / overestimated extracted C of about ∓10% and ∓20%, respectively. In addition, similar to length offset error, the impact of C_{pad} difference is bigger at the highest frequencies, specifically +17% and +27% errors for ±5% and ±10% from the mean, respectively.

As shown in Figure 3.13, the curve of extracted G has a similar shape as that of length offset error as shown in Figure 3.9. The error increases at high frequencies, and reaches nearly 600% and 1300% for ±5% and ±10% of C_{pad} differences from the mean. Just like the impact of length offset error on the extracted G, the error is much smaller (less than about 0.1% below 5GHz), hence the impact of wrong estimation of C_{pad} at low frequencies is insignificant on the extracted G.

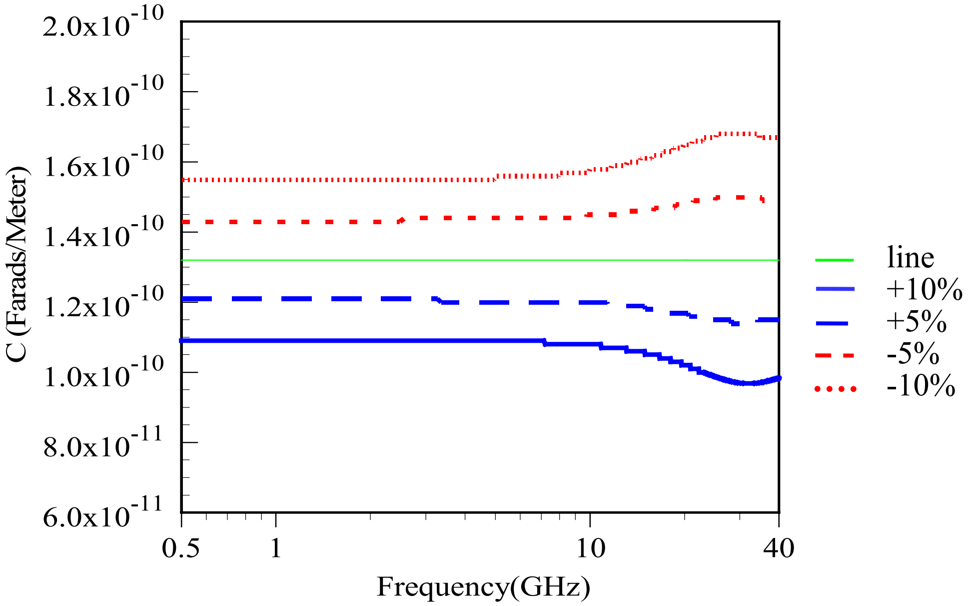

Figure 3.12: Perturbed C per unit of 0.25μm width and 2100μm line length with mean, ± 5%, and ± 10% from the mean of the extracted pad capacitance (C_{pad}).

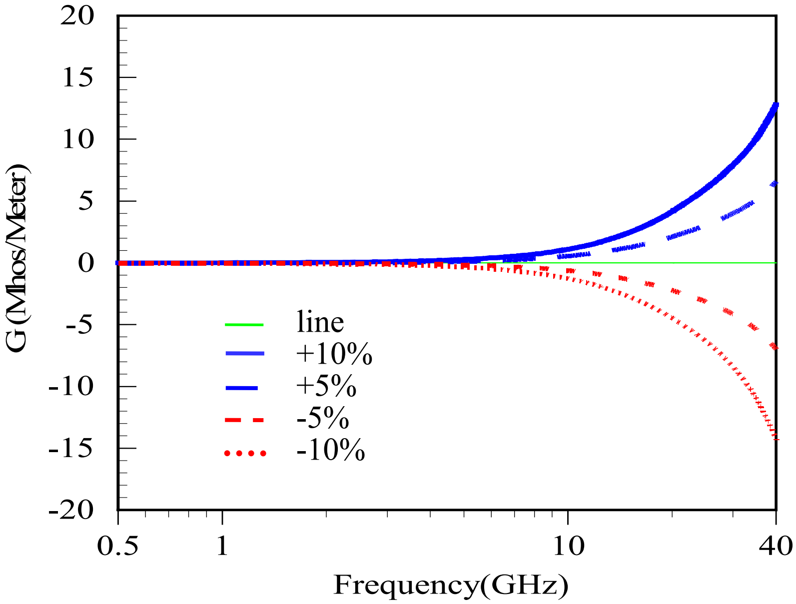

Figure 3.13: Perturbed G per unit of 0.25μm width and 2100μm line length with mean, ± 5%, and ± 10% from the mean of the extracted pad capacitance (C_{pad}).

3.4 SUMMARY AND DISCUSSION

Several possible causes of apparent high frequency dependence for extracted interconnect parameters (i.e., R, L, C, and G per unit length) presented in chapter 2 could be magnitude detection limits, reference plane offset errors, or the wrong estimation of pad parasitics (i.e., C_{pad}) based on an assumed lumped RC network model.

The most noticeable feature is the large error that occurs at high frequencies, higher than the magnitude detection limit frequency. The magnitude limit error is the dominant error if the magnitude of S_{21} is small enough for limiting to occur. The magnitude detection limit error is significant for the 0.25μm and 0.175μm geometries, and is dependent on the line length. In the 0.25μm geometry, the magnitude detection limit error is dominant at a line length of 3400μm for frequencies over 30GHz, 8100μm line length over 10GHz, and 11000μm line length at frequencies over 5GHz for all dielectrics due to the high loss in these lines. Furthermore, in the 0.175μm geometry, the magnitude detection limit error is dominant at a line length of 3000μm for frequencies over 30GHz, 5000μm line length over 20GHz, 7400μm line length at frequencies over 8GHz, and 9000μm line length over 5GHz for all tested dielectrics. The transmission lines, which are over 3000μm for 0.25μm geometry and over 2000μm for 0.175μm geometry, are not a good choice for design of a test structure at our high frequency measurement set-up because of the magnitude limit.

The perturbation simulations presented in this chapter exhibit how error propagation in the S-parameters can affect the extracted RLCG parameters for deep sub-micron transmission line test structures. They show that any apparent frequency dependence at high frequencies might be an artifact due to finite measurement precision and accuracy, compounded by small calibration errors. Based on our measurements, and taking into consideration all of these sources of error, we see no experimental evidence of dispersion and skin effect in considering Copper/SiO_2, Novellus' Coral low-k, and JSR Corp. low-k dielectrics test structures. As shown in the perturbation simulations with errors propagation, a possible cause might be reference plane offset error (length offset error), which is linearly dependent on frequency. Thus, length offset error seems to be a cause for non-physical high frequency dependencies, rather than phase round-off error, which would be a problem at low frequencies for the tested structures. In addition the wrong estimation of pad capacitance affects both the magnitude and phase of S-parameters, unlike length offset error. Except for this, the impact of the wrong estimation of pad capacitance is very similar to that of a length offset error, which depends on the frequency (i.e., bigger effect on high frequency).

Chapter 4

Impact of Probe Placement on High Frequency Measurement

The non-systematic landing position on pads or ISS is enabled to be the cause of a systematic length offset. The finite measurement precision (essentially, length offset error) could be a source of non-physical high frequency dependencies on RLCG extraction as introduced by the perturbation simulation in chapter 3.

In a conventional SOLT calibration procedure for high frequency measurement, which was applied with a two-port microwave calibration method in this section, the incorrect probe position for the standards such as “short”, “open”, “load”, and “thru” on the cascade ISS where SOLT calibration kits are optimized, could produce some amount of the systematic finite error (i.e., reference plane offset error) during the calibration procedure. In addition, in the actual measurement procedures after the calibration was completed, the inconsistent probe placements on wafer pads stimulated the length offset error. Particularly, in this chapter, we will evaluate these possible probe placement impacts on RLCG extraction by comparing actual measurement data differing only by 20μm in the probe landing position for a 2000μm long transmission line (i.e., 1%) in the measurement procedure after completed calibration. Thus, we will show experimentally that the placement of the microwave probes on the interconnect test structure probe pads can also induce non-physical frequency dependencies.

4.1 MEASUREMENT SET-UP

The tested Devices Under Test (DUTs) in this section are embedded microstrip transmission lines of two widths (0.25μm and 0.175μm) with different line lengths using a SiO_2 interlevel dielectric. The nominal cross-sectional dimensions for these structures are identical except for the width as introduced in chapter 2. In addition, a simple probe pad-only test structure consists of ground-signal-ground co-planar metal squares 50μm x 50μm in size as also presented in chapter 2. The test structures for both pad-only and embedded microstrip transmission lines are located on the same die.

High frequency measurements are made using a vector network analyzer (VNA) and carried out by connecting two Cascade Infinite 40 Ground-Signal-Ground 100μm pitch wafer probes to the network analyzer with test cables in this section. In the measurement procedures manual of the HP 8510B, the manufacturer recommends taking 256 averages on the 8510 A/B/C models for measuring the calibration standards. Averaging reduces noise by $\frac{1}{\sqrt{N}}$, where N is the number of averages. The manufacturer also recommends never going below 64 averages when measuring the transmission lines for RLCG extractions. In this section, an applied SOLT (Short, Open, Load, Thru) calibration was performed at the probe tips using a Cascade 101-190 Impedance Standard Substrate (ISS) with 256 averages.

The VNA was used to obtain the scattering parameters (S-parameters) for both the embedded microstrip transmission line (a full two-port measurement) and the pad-only test structure (a one-port measurement). The S-parameters of a given transmission line and pad-only structure were first measured and then converted to the cascaded ABCD parameters. After de-embedding the frequency dependent Y parameter of the pad parasitics at both ends, the characteristic impedance (Z_o) and propagation constant (γ) are were calculated for the transmission line. After the specified line length was divided out, the R (resistance per unit length), L (inductance per unit length), and C (capacitance per unit length) parameters were calculated.

4.2 EXPERIMENTAL METHODOLOGY

In a conventional SOLT calibration procedure, it is essential to correctly land wafer probes on standards of ISS, such as short, open, load, and thru. The cascade wafer probes should be on the center position of the “short” and “load” standard structures on ISS where the SOLT calibration kit is optimized. In addition the correct landing position of the cascade wafer probes for the “thru” standard is approximately 5μm from the visible edge of each standard at zero (just touching) overdrive. The correct ending position is 25μm from the visible outer edge which usually results in around 50μm of overdrive after the zero position from both ends. The calibration coefficients are for the combination of probe type and ISS with the probe placements at the center of the standards on ISS. The best way to set the correct amount of over-travel and skating is to use the alignment marks on the ISS and follow the alignment procedure as introduced by Cascade application notes [51].

After a conventional calibration (SOLT) is completed with correct probe position for standards on ISS, to examine the impact of different probe placement on the wafer pads in the high frequency measurement, two different probe positions on the wafer pads are considered in this chapter.

The first experiment is probe placement “Inside edge” on pads at both ends of a single transmission line as shown in Figure 4.1. The initial landing position of the probe tip is approximately 25μm (the center position of the pad (50μm x 50μm in size)) from the outer edges of each pad. The ending position is approximately 4-5μm from the inner edges of each interconnect port with approximately 20µm of skating after the initial landing.

The second experiment is probe placement at “Center” on wafer pads at both ends of a single transmission line as shown in Figure 4.2. The initial landing position of the probe tip is approximately 5µm from the outer edges of each pad. The ending position is approximately 25µm from the edges of each interconnect port with approximately 20µm of skating after the initial landing.

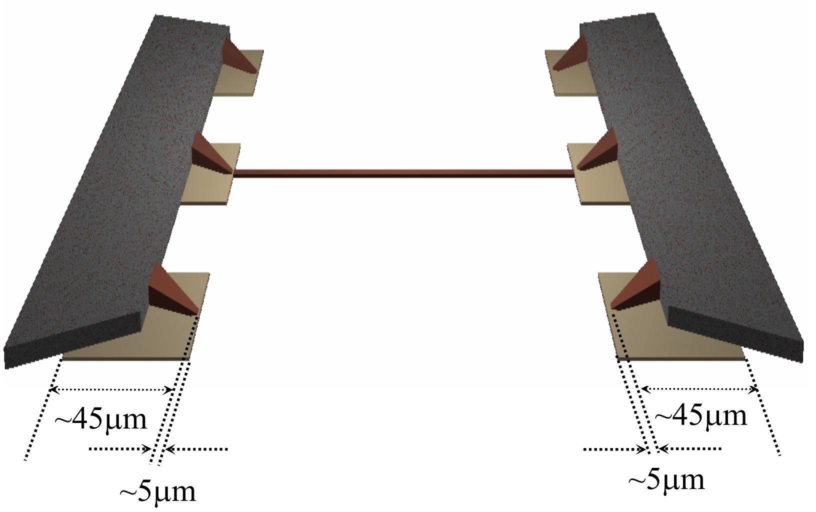

Figure 4.1: Probe placement “Inside edge” on wafer pads: The initial landing position of the probe tip is approximately 25µm (the center position of pad) from the outer edge of each port. The ending position is approximately 45µm from the outer edge of each port with approximately 20µm of skating after the initial landing position.

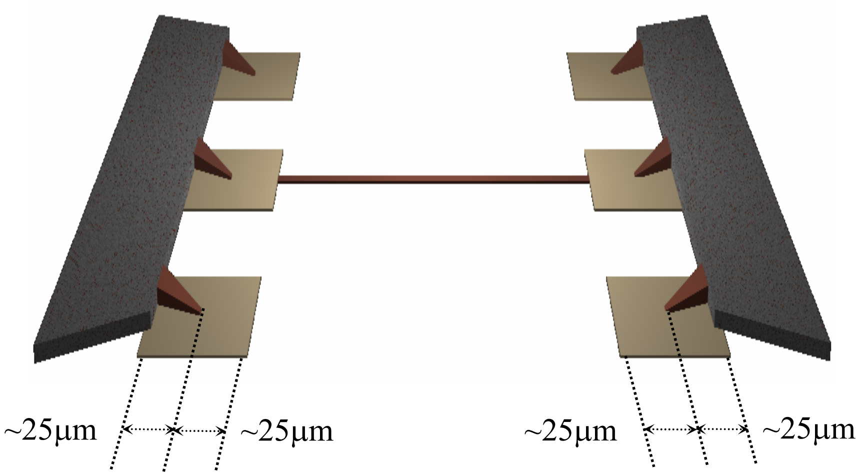

Figure 4.2: Probe placement “Center” on wafer pads: The initial landing position of the probe tip is approximately 5µm (the center position of pad) from the outer edge of each port. The ending position is approximately 25µm from the outer edge of each port with approximately 20µm of skating after the initial landing position.

4.3 RESULTS OF SIMULATION AND MEASUREMENTS

To investigate the impact of the different probe placement on the R, L, C, and G parameters extracted from actual measurement via the perturbation simulation technique as also described in chapter 3, frequency independent R, L, C, and G parameters are assumed (that match the low or mid frequency measured values) and then used with the nominal (mask drawn) line length. The complex propagation constant (γl) and complex characteristic impedance (Z_o) are calculated from the assumed R, L, C, and G. Then, the complex propagation constant (γl) and complex characteristic impedance (Z_o) are converted to the S-parameters of transmission line referenced to $50\,\Omega$ test ports. Next, the S-parameters of a given transmission line and pad-only test structures are converted to ABCD parameters [52]. The effects of pads are then added, and the calculated S-parameters are perturbed by a systematic length offset error (reference plane offset error). Treating the amount of length offset error (reference plane offset error) as a parameter enables us to examine the error propagation that could be caused by different probe placements on the on-wafer probe pads. After calculation and perturbation, the perturbed S-parameters are converted back to ABCD parameters, and then the pad-only test structures at both ends are de-embedded. Afterwards, the perturbed ABCD parameters of the transmission line only are extracted. Finally, the perturbed ABCD parameters of the transmission line only are converted back to the perturbed γl and Z_o of the transmission line only, and the "perturbed" R, L, C, and G parameters are determined. These parameters can then be compared to actual experimentally measured and extracted parameters.

Using the measurements from each landing location (i.e., Inside edge position and Center position) the extracted per unit length R, L, and C for the test structure 0.175μm wide and 2000μm long on SiO_2 wafer for example are shown in Figure 4.3 to Figure 4.8.

Multiple die and multiple measurements have been performed, as well as multiple calibrations and repeated measurements, to ensure that the differences shown are repeatable, and directly traceable to landing position.

As shown in Figure 4.3 to Figure 4.8, the apparent frequency dependence in the extracted RLC parameters from actual measurement at frequencies over about 20GHz is non-physical and has been shown to be possibly due to length offset errors via the perturbation simulations. The extracted R per unit length from actual measurements is pretty much frequency independent at low frequencies (i.e., below 10GHz) for different probe landing positions, which possibly means the impact of probe placement is negligible. However, the extracted R rolls off as much as about 9.5% above 20GHz for the inside edge position as shown in Figure 4.3, and 22.4% above 10GHz for the center position as shown in Figure 4.4. The extracted R has clearly non-physical frequency dependencies at high frequencies for both landing positions, which possibly causes the length offset errors supported by the perturbation simulations with length offset errors.

We now have identified one of the primary sources of this error as being the different probe placement on pads for high frequency measurements. These measurements and simulations show that approximately ±20μm differences at each port in probe placement for a 2000μm long transmission line (i.e., 1%) is critical to the accurate characterization of the transmission line. In summary we have obtained highly systematic results showing that non-physical behavior in extracted interconnect parameters from actual measurements at frequencies over 20GHz can be caused by small changes in the microwave probe landing position. At the higher frequencies, even a small percent difference in probe placement during measurement procedure can change the extracted R, L, and C parameters by as much as 33% for interconnects with lengths of 2000μm.

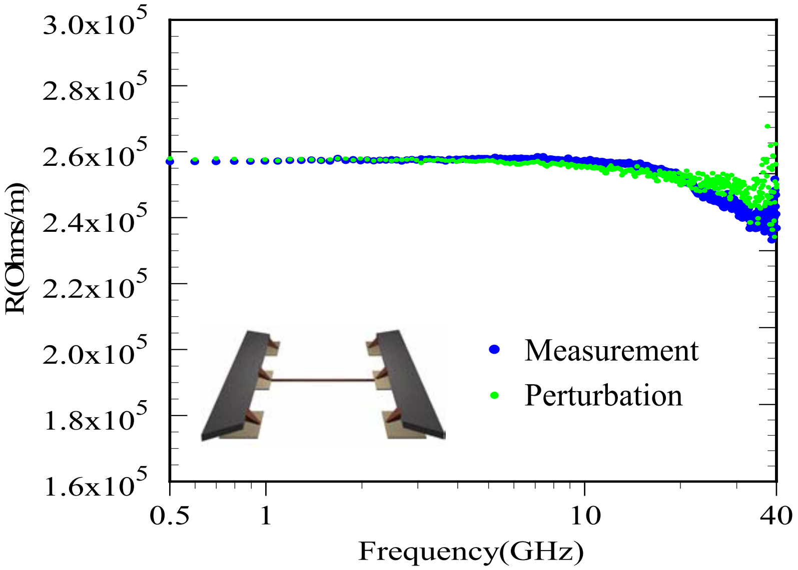

Figure 4.3: The extracted R per unit length for measurement and perturbation simulation of 0.175μm width and 2000μm line length in case of probe placement “Inside edge”. The perturbed error is considered as a -5μm length offset.

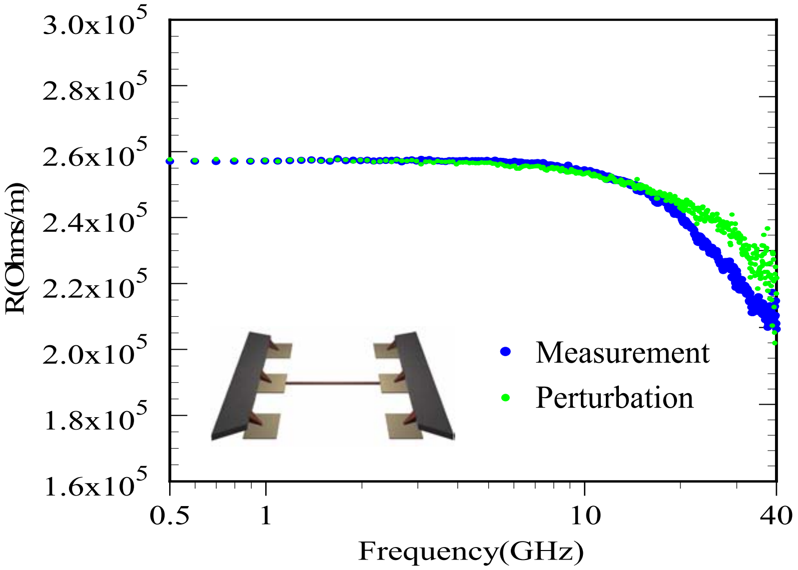

Figure 4.4: The extracted R per unit length for measurement and perturbation simulation of 0.175μm width and 2000μm line length in case of probe placement “Center”. The perturbed error is considered as a -25μm length offset.

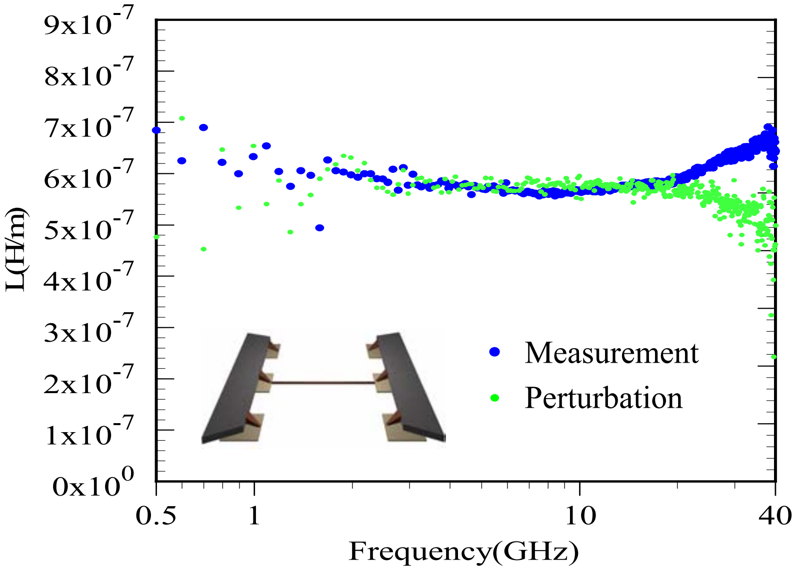

Figure 4.5: The extracted L per unit length for measurement and perturbation simulation of 0.175μm width and 2000μm line length in case of probe placement “Inside edge”. The perturbed error is considered as a -5μm length offset.

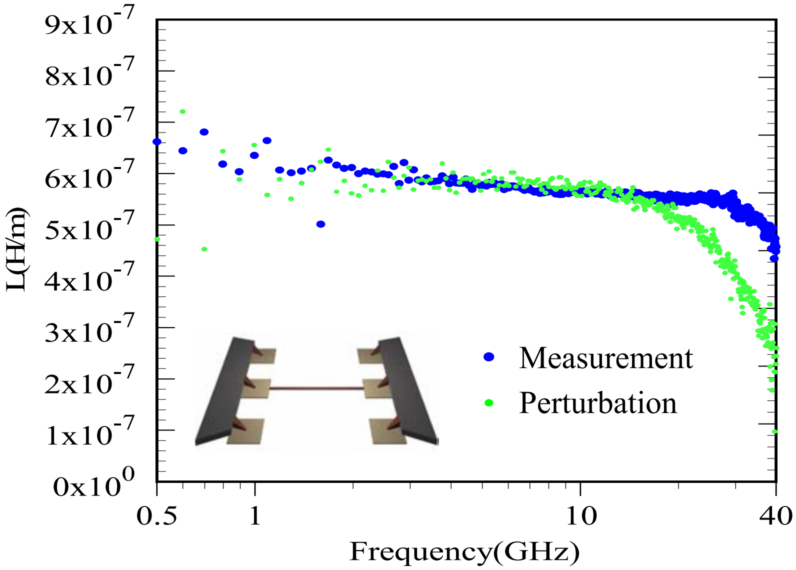

Figure 4.6: The extracted L per unit length for measurement and perturbation simulation of 0.175μm width and 2000μm line length in case of probe placement “Center”. The perturbed error is considered as a -25μm length offset.

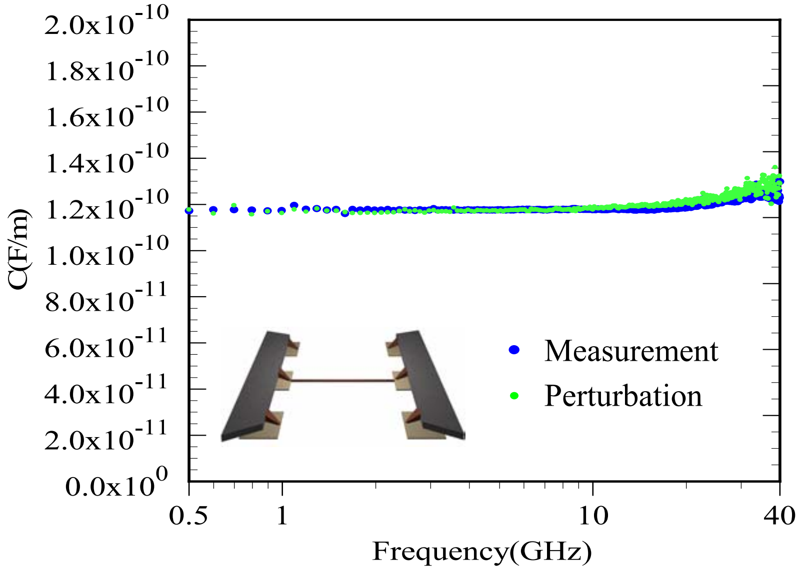

Figure 4.7: The extracted C per unit length for measurement and perturbation simulation of 0.175μm width and 2000μm line length in case of probe placement "Inside edge". The perturbed error is considered as a -5μm length offset.

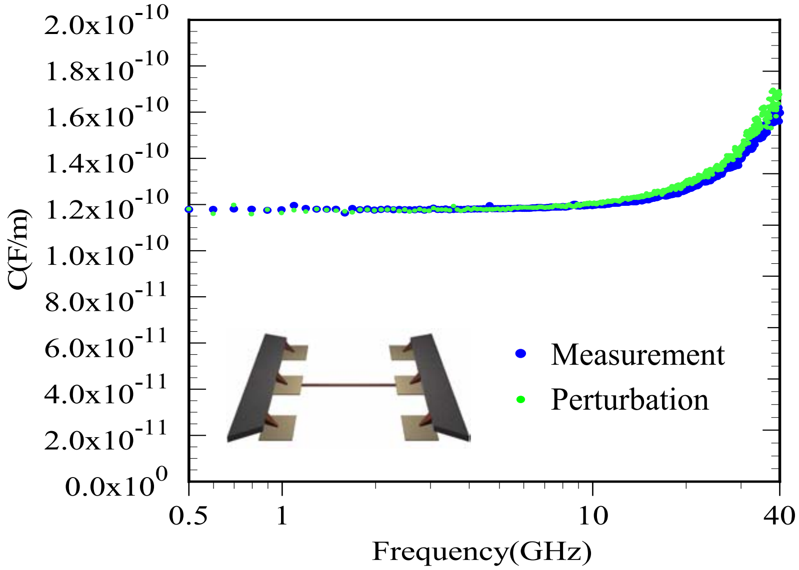

Figure 4.8: The extracted C per unit length for measurement and perturbation simulation of 0.175μm width and 2000μm line length in case of probe placement "Center". The perturbed error is considered as a -25μm length offset.

In this chapter, experimental data showing the impact of probe placement on the extracted per unit length R, L, and C for deep submicron cross-sectional copper interconnects are illustrated. This chapter presents actual measurement data for high frequencies up to 40GHz that demonstrate that the precise location of microwave probes on 50μm x 50μm square pads can have significant effects on the extracted per unit length of the R, L, and C parameters at frequencies above about 20GHz. The effect appears to be due to length offset errors from the different landing placements of the probes. Variations in landing position as small as 20μm at each port might introduce enough phase error to produce significant effects for a 2000μm long interconnect test structure. This is particularly problematic since most microwave probes require skating distances on the order of ten microns to ensure good contact.

Chapter 5

Impact of De-embedding Network Models for Pad on the Extraction of Interconnect Parameters

We have shown that extracted per unit length RLCG parameters exhibit non-physical frequency dependencies at high frequencies (i.e. over 20GHz) under an assumed network model in chapter 2. In addition, we have presented the extracted RLCG parameters that show the location of microwave probes on pads (50μm x 50μm in size) can have a significant effect at frequencies above about 20GHz under an assumed network model in chapter 4. A possible explanation for the apparent frequency dependencies in the extracted parameters for different landing positions seems to be due to the finite measurement precision, specifically the finite errors, which might be induced in the process of measurement in previous chapters.

As to the other point of view, to actually extract the desired interconnect parameters from the measurements, the correct network model of the pads would be required for de-embedding pad parasitics because the tested interconnect transmission lines were connected to pad parasitics at both ends of the interconnect [53-56]. After the de-embedding of the pad parasitics with an assumed network model as demonstrated in previous chapters, the extracted RLCG parameters for the tested interconnect transmission lines were non-physical high frequency dependencies, and furthermore, the extracted RLC parameters from the actual measurements for both inside edge and center probe positions as shown in Figure 4.3 to Figure 4.8 of chapter 4 were not even independent for the landing position. In the case of applying the correct network model to de-embed pad parasitics, pad landing position should not change the extracted interconnect transmission line parameters (i.e., RLCG per unit length) because the extracted interconnect parameters should be characteristic of the interconnect, not the pads or probes.

A feasible explanation for the apparent high frequency dependencies in the extracted parameters might be the use of an incorrect network model of the probe pads (i.e., one without the discontinuities included in an assumed network model). Therefore, the importance of the network model of the pads for extracting interconnect parameters from experiments of different probe positions at high frequencies is the focus of this chapter. Furthermore, we will show that extracted per unit length RLCG parameters often exhibit non-physical frequency dependencies at the high frequencies (i.e. above about 20GHz) due to the failure to consider the discontinuities from the changing geometry between the pads and the interconnect in the de-embedding network model of pads [31]. Consequently, the new network models which consider discontinuities to more accurately extract the interconnect parameters from high frequency measurements will be proposed in the last section of this chapter.

5.1 METHODOLOGY

The tested structures were embedded microstrip transmission lines of different nominal line-widths (0.25μm and 0.175μm wide) and different nominal line-lengths (2100μm and 2000μm long, respectively) on SiO_2 dielectric thin film. The cross-sectional dimensions for these structures are nominally identical except for the line-width as also presented in chapter 2. To make the connection between the microwave wafer probes and the embedded interconnect transmission lines requires the use of probe pads at both ends of the interconnects. Since the probe pads produce parasitics in the two-port high frequency measurement, those parasitics must be de-embedded in order to correctly determine the desired interconnect parameters. To help characterize the probe pads there are "pad-only" test structures on the die separately. The pad-only test structure consists of ground-signal-ground co-planar metal squares 50μm×50μm in size on SiO_2 dielectric thin films as also described in chapter 2.

High frequency measurements were made using the HP 8510B vector network analyzer (VNA). The VNA was used to obtain the scattering parameters (S-parameters) for the embedded interconnect transmission lines (a full two-port measurement) and the pad-only test structures (a one-port measurement). After applying SOLT calibration for one and two-port measurements, the reference plane was placed on the end of probe tips.

Again, to truly extract the desired interconnect parameters of the tested DUTs from the measurements, a network model of the pads is essential for de-embedding. The extracted interconnect parameters should be characteristic of the interconnect, not the pads or probes, thus probe landing position should not change the extracted interconnect parameters. According to these, two different probe positions on the pads were used to both determine if probe positions on the probe pads affect the extraction of the transmission line interconnect parameters and examine the correct network model of de-embedding pad parasitics.

The first experiment is probe placement at the "Inside edge" of the pads at both ends of the interconnect transmission line as shown in Figure 4.1 of chapter 4. After appropriate probe skating shown in chapter 4, the final resting position is approximately 4-5μm from the edges of each interconnect port. The second experiment is probe placement at the "Center" of wafer pads as also shown in Figure 4.2. After appropriate probe skating shown in chapter 4, the ending position is approximately 25μm from the edges of each interconnect port. Multiple die and multiple measurements have been performed, as well as multiple calibrations and repeat measurements, to ensure that the differences shown are repeatable, and directly traceable to the landing position.

If the network model of the pads is most likely correct, the final extracted interconnect parameters should be the same for both landing positions used in the experiments. Furthermore, to find a more feasible network model of the tested DUTs (i.e., interconnect transmission lines), the extracted per unit length RLCG parameters of the interconnect transmission lines might be appropriate for frequency independencies, even at the highest frequencies because there is not any reason that the extracted interconnect parameters would appear to be non-physical frequency dependent for the tested DUTs.

5.2 PAD DE-EMBEDDING NETWORK MODELS

The network analyzer measures S-parameters of the DUTs. Since the pad parasitics at both ends connected to the interconnect we could not extract the RLCG parameters of the interconnect directly. Therefore, using an assumed network model of these parasitics, we convert S-parameters to per unit length RLCG parameters of the interconnect-only. In this section we will investigate the various network models, which could not be susceptible to changes in landing position, and simultaneously produce frequency independent interconnect parameters, even at the highest frequencies no matter the landing position of the probes. Furthermore, we will show that the incorrect de-embedding network model could induce the non-physical high frequency dependencies of the extracted per unit length RLCG interconnect parameters.

5.2.1 Lumped RC_{pad} Network Model of Pad

Since the pads (i.e., 50μm×50μm in size) are so small compared to the wave lengths used in the high frequency measurements (for example, 10^4μm in free space at 30GHz), a lumped element network model might be sufficient to de-embed the pad parasitics. According to the Smith chart from a one-port measurement for an open pad-only test structure as shown in Figure 2.8 and comparing pad capacitance (i.e., C_{pad}) and self-capacitance of the transmission line itself as shown in Figure 2.9 of chapter 2, the open pads produce a considerable amount of the capacitive parasitics (i.e., C_{pad}) compared to the transmission lines itself and very small resistive parasitics (i.e., R_c).

A large area landing pad (50μm x 50μm in size) produces a much bigger parallel plate capacitance of the signal pad to the ground plane than a mutual coplanar parasitic capacitance of the signal and ground pads and a fringing component. The C_{pad}, which will be considered in this model, contains all the capacitive parasitics that can be extracted from a one-port measurement of an open pad-only test structure. The capacitive parasitics can be extracted from measured S_{11} parameters of the open pad-only test structure with the assumed port impedance (Z_o), which is equal to 50Ω. Based on the measured S_{11} from the one-port measurement for a pad-only test structure, the admittance of the pad-only test structure (Y_{pad}) can be extracted as shown in Equation (5.1).

$$Y_{pad} = \frac{1}{Z_o} \cdot \frac{1 - S_{11}}{1 + S_{11}} \tag{5.1}$$

The model of the pad-only test structure can consist of only a lumped resistor and capacitor, considerably reducing any uncertainties in the extraction process. Thus, the effective capacitive parasitics (i.e., C_{pad}) can be extracted from the extracted Y_{pad} after being divided by ω from an imaginary admittance as shown in Equation (5.2).

$$C_{pad} = \frac{\mathrm{Im}(Y_{pad})}{\omega} \tag{5.2}$$

In addition the resistive parasitics (R_c) can be extracted from regression analysis of the DC resistance measurements. The resistive parasitics (R_c) contain resistances of the external test cables connected between the vector network analyzer and probes, connectors, the pad itself, probe contact at landing pad, and vias (metal 1-to-metal 2 contacts) of probe pads. In high frequency measurement we could eliminate the parasitics of the external cables, connectors, and wafer probes through calibration. However, the resistive parasitics of the pad itself, the pad contact, and vias (metal 1-to-metal 2 contacts) could not be removed through the microwave calibration. Therefore, the resistive parasitics of the pad itself, the pad contact, and vias for high frequency parameter extraction of a two-port will be considered in the lumped RC_{pad} network model.

Since the DUT is such a lossy line, the parasitic resistance (R_c) of the probe pads at both ends has a small effect on parameter extraction for the transmission line interconnects. However, the parasitic capacitance (C_{pad}) of the probe pads can significantly affect the parameter extraction because C_{pad} is such a considerable amount compared to the interconnect parameters. Thus, in this network model, we choose the mean value (averaged over the frequency sweep up to 40GHz) of the extracted pad capacitance via one port measurement among multiple experiments, although the extracted pad capacitances are relatively frequency independent.

The extracted parameters were based on a network model consisting of a RLCG transmission line with a pad capacitance (C_{pad}) and contact resistance (R_c) at both ends of the transmission line. Assuming that the same parasitics are with the transmission line at both ends as shown in Figure 5.1, the ABCD parameters allow the cascading of networks by the multiplication of the ABCD matrices. The relationship of $[ABCD]_{line}$ and $[ABCD]_{measured}$ matrices is shown in Equation (5.3).

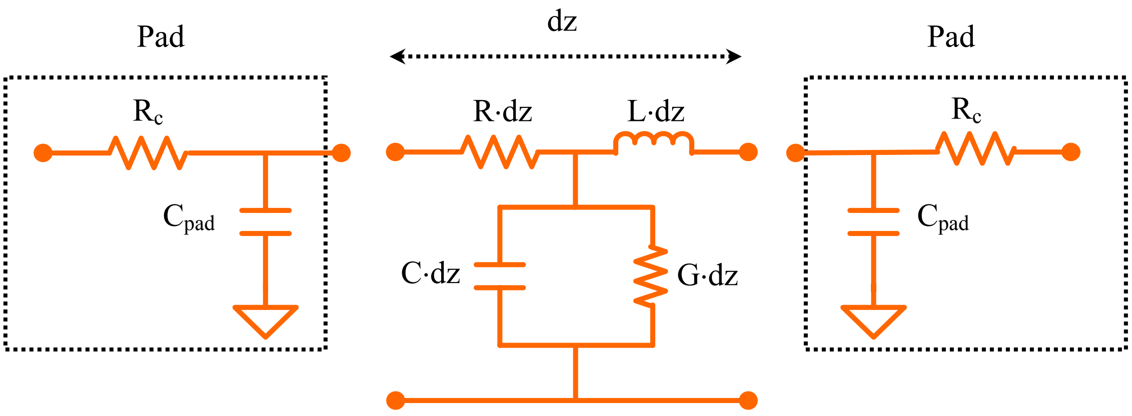

Figure 5.1: Lumped RC_{pad} network model of pad.

$$\begin{bmatrix} A & B \\ C & D \end{bmatrix}_{measured} = \begin{bmatrix} 1 & R_c \\ 0 & 1 \end{bmatrix} \begin{bmatrix} 1 & 0 \\ j\omega C_{pad} & 1 \end{bmatrix} \begin{bmatrix} A & B \\ C & D \end{bmatrix}_{line} \begin{bmatrix} 1 & 0 \\ j\omega C_{pad} & 1 \end{bmatrix} \begin{bmatrix} 1 & R_c \\ 0 & 1 \end{bmatrix} \quad (5.3)$$

After de-embedding the pad parasitics at both ends, the characteristic impedance (Z_o) and propagation constant (γ) are calculated for the transmission line only from $[ABCD]_{line}$ parameters, as shown in Equation (5.4). Once the characteristic impedance (Z_o) and propagation constant (γ) are determined, and after the specified nominal line-length is divided out, then the transmission line parameters R (resistance per unit length), L (inductance per unit length), C (capacitance per unit length), and G (conductance per unit length) can be calculated from the extracted propagation constant (γ) and characteristic impedance (Z_o) as shown in Equation (5.5) and (5.6).

$$\begin{bmatrix} A & B \\ C & D \end{bmatrix}_{line} = \begin{bmatrix} \cosh \gamma l & Z_o \sinh \gamma l \\ \dfrac{\sinh \gamma l}{Z_o} & \cosh \gamma l \end{bmatrix} \quad (5.4)$$

$$\gamma = \sqrt{(R + j\omega L)(G + j\omega C)} \tag{5.5}$$

$$Z_o = \sqrt{\frac{(R + j\omega L)}{(G + j\omega C)}} \tag{5.6}$$

Using this lumped RC_{pad} de-embedding network model of pads, the extracted per unit length R and C of the interconnect parameters of a 0.175μm wide and 2000μm long interconnect on SiO_2 dielectric thin film for a two-probe landing position are shown in Figure 5.2 and Figure 5.3. Recall that the interconnect parameters are intrinsic properties of the interconnect, and hence should not depend on probe positioning. However, the extracted per unit length R and C appear to depend on probe landing position under the lumped RC_{pad} network model. In addition, the extracted R parameters for both inside edge and center landing positions decrease at high frequencies, which is clearly non-physical. Thus, the systematic non-physical high frequency dependencies of the extracted transmission line interconnect parameters for different landing positions suggest that the lumped RC_{pad} network model of the pad is not an adequate network model for de-embedding pad parasitics of the tested DUTs.

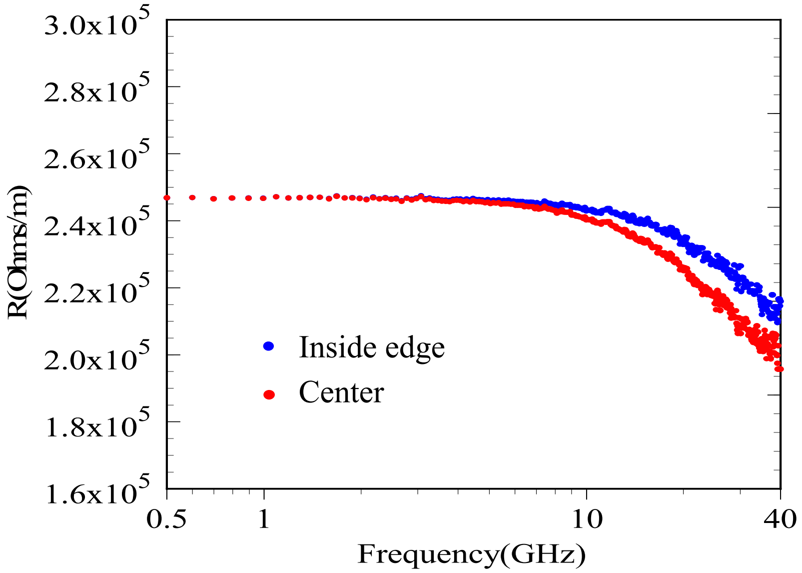

Figure 5.2 Extracted R per unit length of 0.175μm width and 2000μm line-length under lumped RC_{pad} network model of pad.

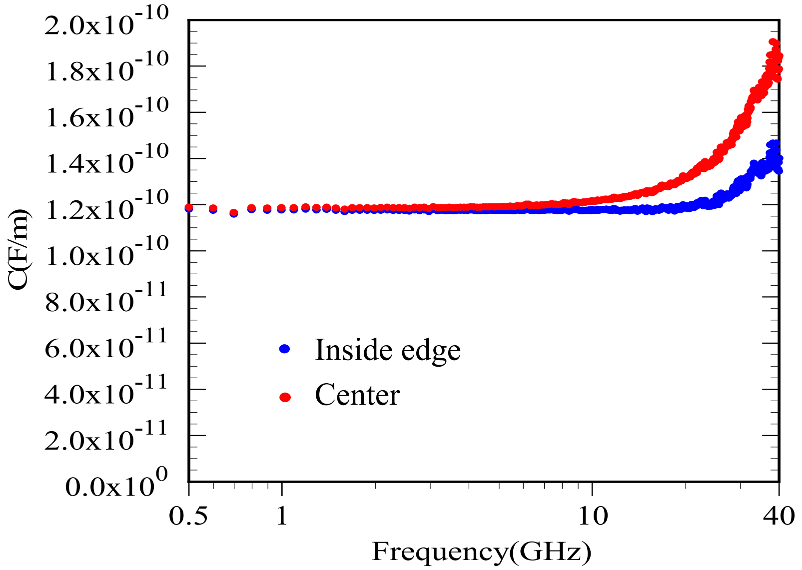

Figure 5.3 Extracted C per unit length of 0.175μm width and 2000μm line-length under lumped RC_{pad} network model of pad.

5.2.2 Frequency Dependent Y_{pad} Network Model of Pad

If the pads can be represented as lumped elements due to considering the pad size and wave lengths used in high frequency measurements, then the quantity required for de-embedding would also be a frequency dependent shunt admittance of the open pads. The frequency dependent shunt admittance (Y_{pad} parameters) of the open pads can be extracted using measured S_{11} data of separate pad-only test structures on-wafer using Equation (5.1). Assuming that the same parasitics for both sides of the interconnect transmission line, which are frequency dependent Y_{pad} parameters from a one-port measurement of an open pad-only test structure, are with the transmission line at both ends as shown in Figure 5.4, the ABCD parameters, allows the cascading of networks by the multiplication of the ABCD matrices.

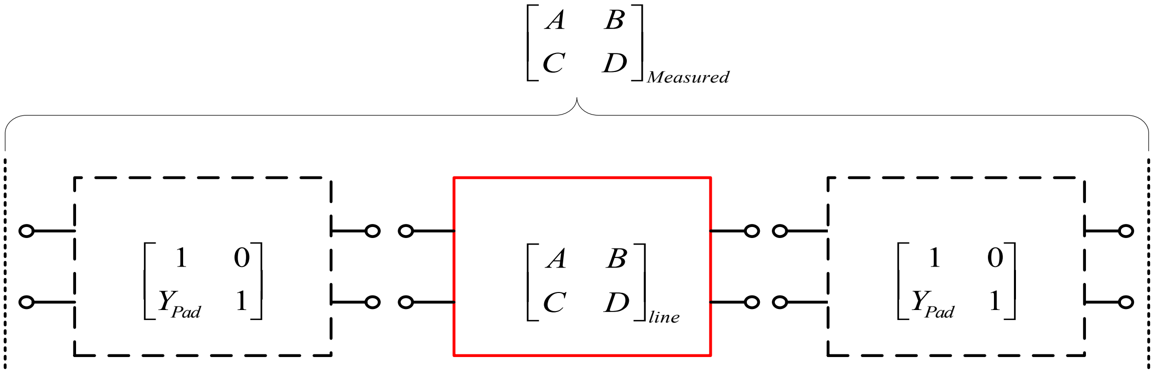

Figure 5.4: Frequency dependent Y_{pad} network model of pad.

The total network model in ABCD parameters would then be

$$\begin{bmatrix} A & B \\ C & D \end{bmatrix}_{measured} = \begin{bmatrix} 1 & 0 \\ Y_{pad} & 1 \end{bmatrix} \begin{bmatrix} A & B \\ C & D \end{bmatrix}_{line} \begin{bmatrix} 1 & 0 \\ Y_{pad} & 1 \end{bmatrix}. \tag{5.7}$$

Using appropriate matrix inverses, the extracted interconnect transmission line ABCD parameters ($ABCD_{line}$) can be obtained. After de-embedding the pad parasitics, the characteristic impedance (Z_o) and propagation constant (γ) are calculated for the transmission line interconnect only at each measured frequency as shown in Equation (5.4). After the specified line length is divided out, the per unit length RLCG parameters can be calculated from the extracted characteristic impedance (Z_o) and propagation constant (γ) as shown in Equation (5.5) and (5.6).

Using a frequency dependent Y_{pad} network model of pad de-embedding, the extracted R and C per unit length of interconnect parameters of a 0.175μm wide and 2000μm long interconnect on SiO_2 dielectric thin film for two-probe landing positions are shown in Figure 5.5 and Figure 5.6. The extracted R and C based on a frequency dependent Y_{pad} network model also appear to depend on probe landing positions. And the extracted R decreases for both probe landing positions at high frequencies, which is clearly non-physical. Thus, the systematic non-physical frequency dependencies of the extracted transmission line interconnect parameters for different landing positions imply that the frequency dependent Y_{pad} model of the pad is not an adequate network model for de-embedding pad parasitics. The frequency dependent Y_{pad} network model of pads is similar to the lumped RC_{pad} model because the extracted R and C have the dependencies of landing position and obviously non-physical phenomena at high frequencies.

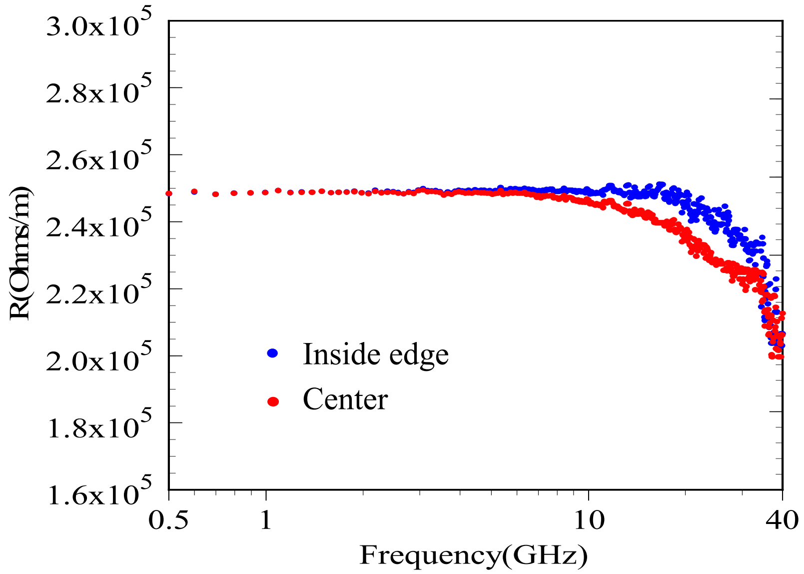

Figure 5.5: Extracted R per unit length of 0.175µm width and 2000µm line-length under frequency dependent Y_{pad} network model of pad.

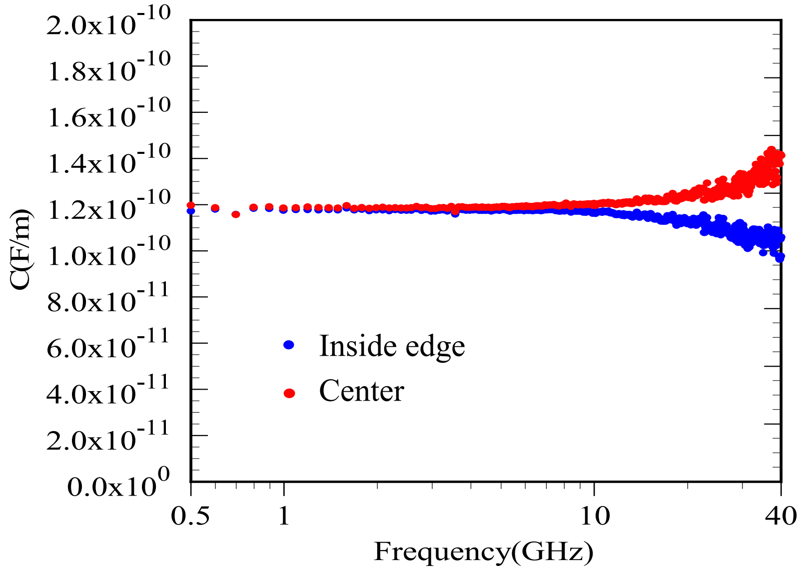

Figure 5.6: Extracted C per unit length of 0.175µm width and 2000µm line-length under frequency dependent Y_{pad} network model of pad.

5.2.3 Transmission-Line (T-line) Network Model of Pad

If the pad was a simple lumped element, it should not matter where probes land on pads (50μm×50μm in size). However, using the lumped de-embedding network models of pads shown in previous sections, the extracted interconnect parameters seem to be a function of the landing position, and furthermore, they are clearly non-physical. Thus, those data suggest the simple lumped pad network models are not enough to extract the desired interconnect parameters. In addition, the obvious observation from the original S-parameters for the tested DUTs was a phase shift at high frequencies in different landing positions, which was a highly systematic and repeatable observation as shown in Figure 5.7 and Figure 5.8. That might suggest a wave propagation effect in the pads themselves in different landing positions. Hence, we have also tried to model the pads as distributed networks by using a transmission line (T-line) pad model [55].

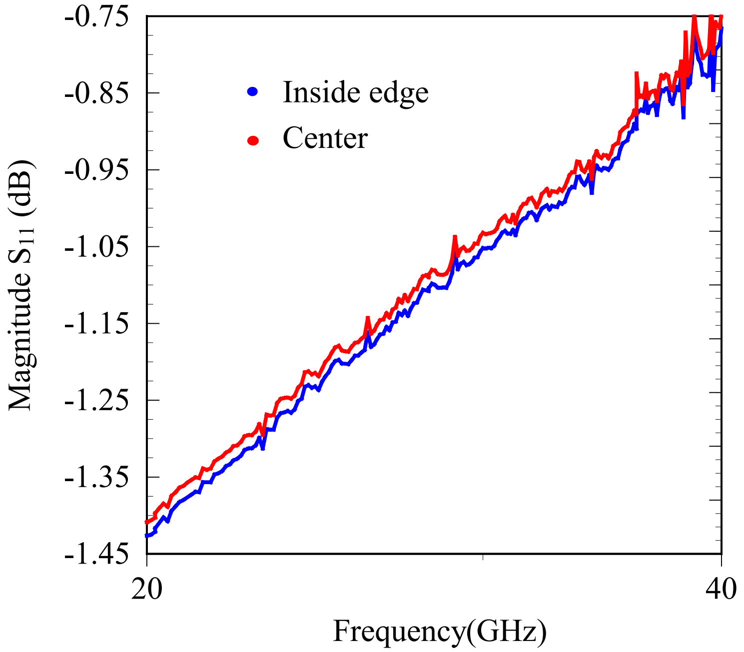

Figure 5.7: Measured magnitude of S_{11} parameter of 0.175μm width and 2000μm line-length for inside edge and center positions.

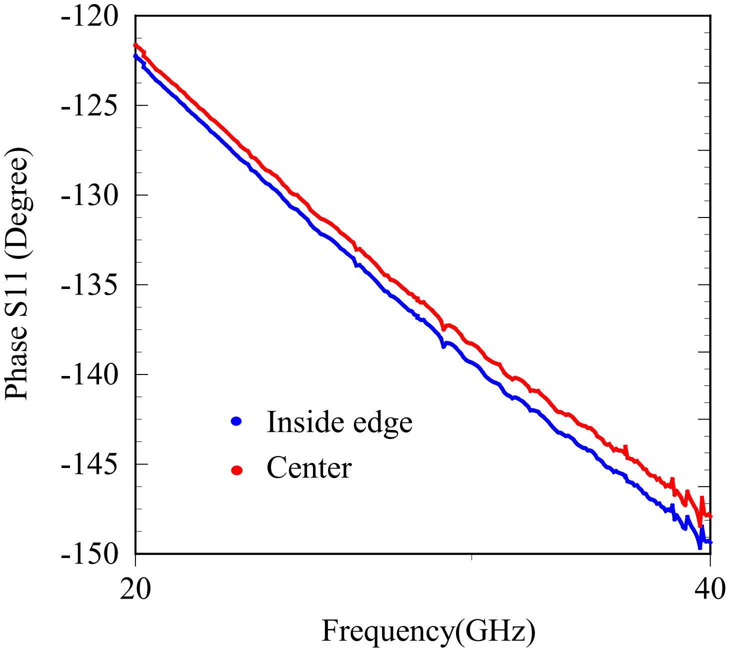

Figure 5.8: Measured phase of S_{11} parameter of 0.175μm width and 2000μm line-length for inside edge and center positions.

To construct a fairly general model of the whole test structure considering the transmission line (T-line) pad model, which could account for transmission line effect in the pads, we divided the pads into two pieces based on probe tip position (probe tip measurement plane) as shown in Figure 5.9. The part of the pad between the probe tips and the transmission line interconnect we call the “inner pad”, with length “l_1”. This part of the pad is modeled using R_{pad}, L_{pad}, and C_{pad} per unit length parameters. The part of the outside pad from the probe tips (probe tip measurement planes) we call the “outer pad”, with length “l_2”, and with the same set of R_{pad}, L_{pad}, and C_{pad} per unit length parameters. In the complete network model of the pads at both ends connected to the interconnects at center, the ABCD parameters of inner and outer divided pad model are given by Equation (5.8) and (5.9).

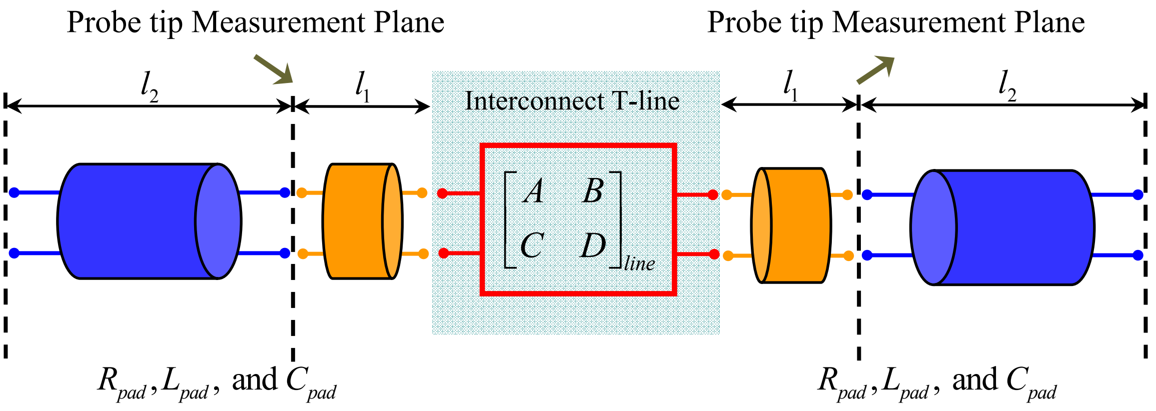

Figure 5.9: Transmission-line (T-line) network model of pad.

$$\begin{bmatrix} A & B \\ C & D \end{bmatrix}_{pad}^{inner} = \begin{bmatrix} \cosh \gamma_{pad} l_1 & Z_{o\_pad} \sinh \gamma_{pad} l_1 \\ \dfrac{\sinh \gamma_{pad} l_1}{Z_{o\_pad}} & \cosh \gamma_{pad} l_1 \end{bmatrix} \tag{5.8}$$

$$\begin{bmatrix} A & B \\ C & D \end{bmatrix}_{pad}^{outer} = \begin{bmatrix} 1 & 0 \\ \dfrac{1}{Z_{o\_pad}} \tanh(\gamma_{pad} l_2) & 1 \end{bmatrix} \tag{5.9}$$

In the above equations γ_{pad} and Z_{o_pad} are the propagation constant and characteristic impedance of the pads, respectively. The γ_{pad} and Z_{o_pad} can be constructed by R_{pad}, L_{pad}, and C_{pad} per unit length parameters as shown in Equation (5.10) and (5.11).

$$Z_{o\_pad} = \sqrt{\frac{R_{pad} + j\omega L_{pad}}{j\omega C_{pad}}} \tag{5.10}$$

$$\gamma_{pad} = \sqrt{(R_{pad} + j\omega L_{pad}) \cdot j\omega C_{pad}} \tag{5.11}$$

Since we can accurately measure and extract the pad capacitance at low frequencies from the open pad-only test structures, we can determine the C_{pad} transmission line parameter for the pad. However, the problem is that we do not have a test structure to actually measure the R_{pad} and L_{pad} parameters of the pad regions. Thus, the R_{pad} parameter for the pad was determined based on a simple calculation using the nominal pad geometries with bulk copper conductivity, and L_{pad} parameters for the pad were determined using SIMIAN (Surface Impedance Method for Interconnect Analysis) [46], which is a program for calculating the series impedance of two-dimensional multi-conductor interconnects and transmission lines using the Surface Ribbon Method. In addition, l_1 (i.e., length from contact point to inner edge) and l_2 (i.e., length from outer edge to contact point) are known from the actual pad landing position and the size of the pads.

Using a fairly general transmission-line (T-line) model of pad de-embedding, the extracted per unit length R and C of interconnect parameters of a 0.175μm wide and 2000μm long interconnect on SiO_2 dielectric thin film for two-probe landing positions are shown in Figure 5.10 and Figure 5.11. The extracted R per unit length at the low frequency is about 250kΩ/m, and C per unit length at the low frequency is about 0.12nF/m, which are the identical to those of lumped pad models. However, at high frequencies, the extracted R and C per unit length based on transmission line (T-line) pad model do also seem to depend on probe landing position. In addition, the extracted R decreases for both landing positions at high frequencies, which is non-physical behavior. Thus, the non-physical frequency dependencies of the extracted interconnect parameters for different landing position also imply that the transmission line (T-line) model of pads does not accurately extract the desired interconnect parameters as well as the frequency dependent Y_{pad} pad and lumped RC_{pad} model does for de-embedding pad parasitics.

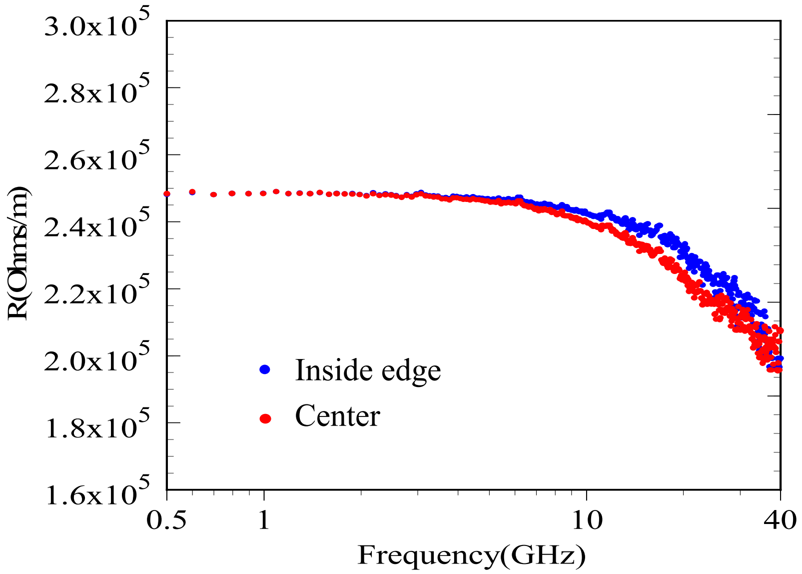

Figure 5.10: Extracted R per unit length of 0.175μm width and 2000μm line-length under transmission-line (T-line) network model of pad.

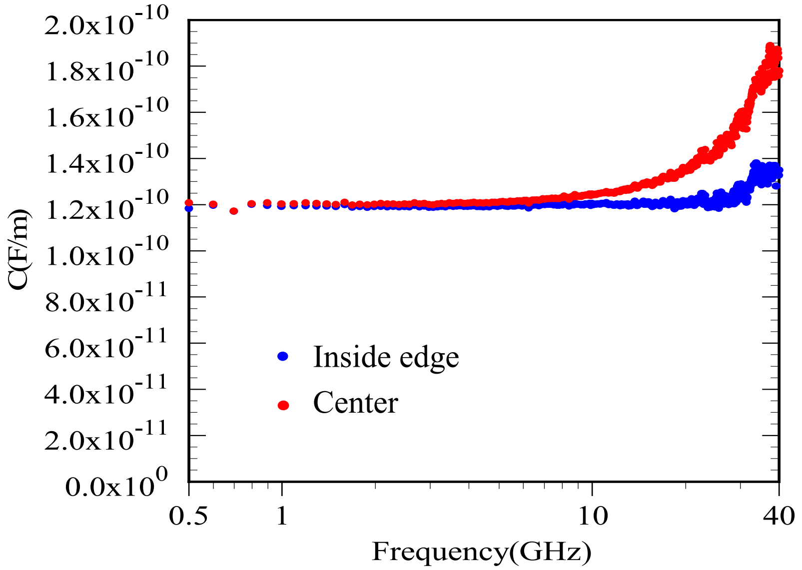

Figure 5.11: Extracted C per unit length of 0.175μm width and 2000μm line-length under transmission-line (T-line) network model of pad.

For the verification of the T-line pad model, it is valuable to compare the measurement data with the calculated data for open pad-only test structure based on the T-line pad model (i.e., the extracted and calculated imaginary Y_{pad} in the frequency domain up to the highest frequency). Figure 5.12 presents the extracted imaginary admittance (i.e., magenta and orange-dotted curves) of a simple open pad-only test structure from a one-port measurement through the different landing positions.

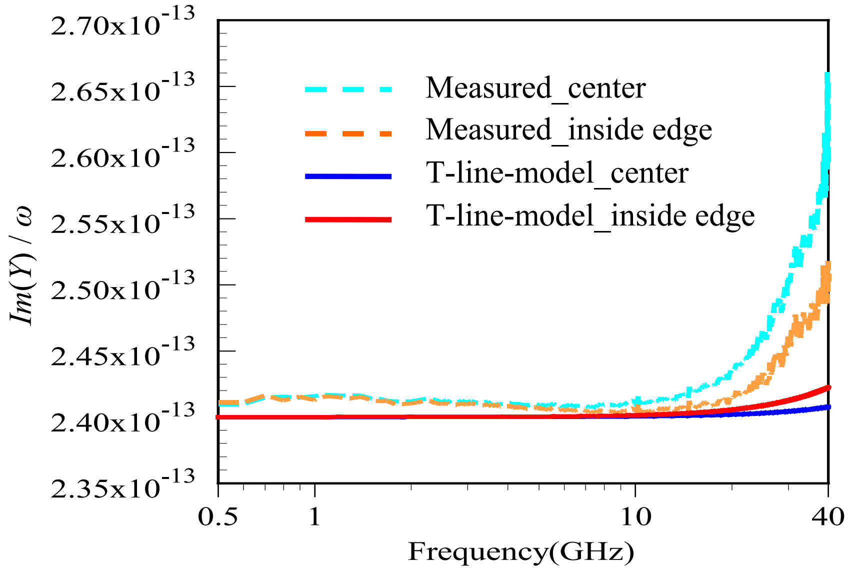

Figure 5.12: The extracted imaginary admittance from one-port measurement and calculated from transmission-line (T-line) network model of open pad-only test structure. Magenta and orange-dotted: measured open pad-only test structure when a probe lands on center and inside edge of the pad. Blue and red-solid: open pad modeled using transmission-line (T-line) when a probe lands on center and inside edge of the pad.

As shown in Figure 5.12, the extracted the imaginary Y_{pad}s from a one-port measurement for a pad-only test structure have landing position dependencies. We expected this landing position dependency possibly came from wave propagation on the pads due to the different propagation length of the landing position on the pads. If this transmission-line (T-line) model of pads is correct, we should be able to match it to measurements made on the pad-only test structures. The extracted imaginary admittance from a one-port measurement of an open pad-only test structure (shown in dotted curves) and calculated data from the T-line pad model based on Equation 5.10 and 5.11 of a simple pad-only test structure (shown in solid curves) are shown in Figure 5.12.

$$Y_{pad-center} = \frac{\tanh(\gamma_{pad} \cdot l_{1\_center})}{Z_{o\_pad}} + \frac{\tanh(\gamma_{pad} \cdot l_{2\_center})}{Z_{o\_pad}} \tag{5.10}$$

$$Y_{pad-inside\_edge} = \frac{\tanh(\gamma_{pad} \cdot l_{1\_inside-edge})}{Z_{o\_pad}} + \frac{\tanh(\gamma_{pad} \cdot l_{2\_inside-edge})}{Z_{o\_pad}} \tag{5.11}$$

At the low frequency range, the T-line model may represent the pad-only test structure. However, as the frequency goes up, the T-line model does not match the extracted data from measurements. From the result shown in Figure 5.12, we have found that the transmission-line (T-line) pad model can not produce enough inductance to match measured data of a pad-only test structure as shown in solid and dotted curves in Figure 5.12. In addition, ~20μm difference between center and inside edge landing positions is less than 0.3% of a wavelength throughout the measurement frequency range, which is far too small to generate the disparity of curves in Figure 5.12. This shows that landing position dependency can not be explained by simple wave propagation.

5.2.4 Discontinuity Models

The curves in Figure 5.12 indicate that the pad model requires an inductance to explain increasing imaginary admittance as frequency increases; the value of this series inductance (i.e., L_1 shown in Figure 5.13) also depends on landing position. This suggests we should try to explain the landing position dependency of measured imaginary admittance (i.e., $Im(Y)/\omega$) for pad-only test structure by “current redistribution” phenomena instead of “wave propagation” phenomena. The other clearly required element of the pad model is its capacitance, C_{pad}. Therefore, we constructed a lumped L_1-C_{pad} model for an open pad-only test structure as shown in Figure 5.13.

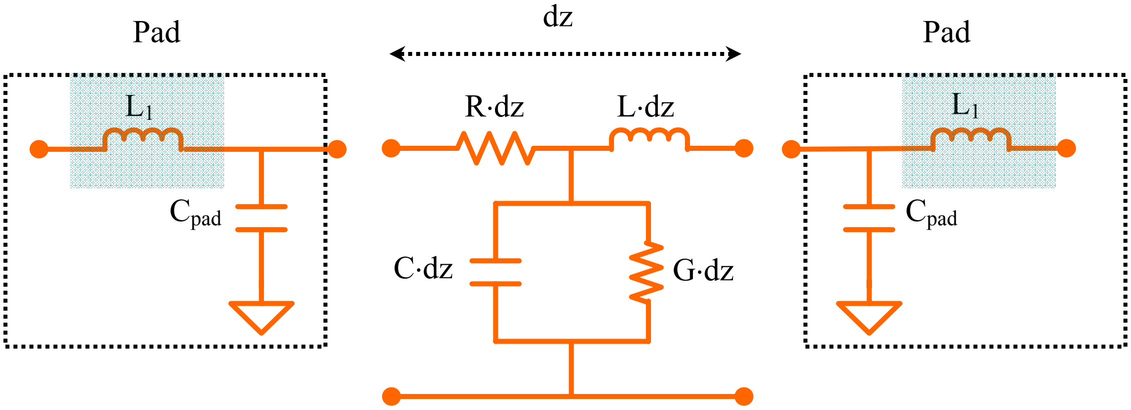

Figure 5.13: Lumped L_1-C_{pad} network model of open pad-only test structure. L_1 is due to geometrical discontinuity between probe tip and the pad.

We adjust only L_1 to match the imaginary admittance data extracted from the open pad-only test structure (Magenta and orange-dotted curves in Figure 5.14) because C_{pad} can be precisely extracted from measurement of the open pad-only test structure at low frequencies. This approach shows good agreement with measured data (shown in magenta and orange-dotted curves in Figure 5.14). Here the fitted inductance (L_1) is 7×10^{-12} [H] for center position and 2×10^{-12} [H] for inside edge position, using $C_{pad} = 2.43\times10^{-13}$ [F] from a one-port measurement of the open pad-only test structure. This shows that the landing position dependency for the pad-only test structure can be explained by current redistribution between the probe tip and the pad surface represented by the addition of a single lumped inductor; hence the complete probe tip and pad model is just an L_1-C_{pad} network model.

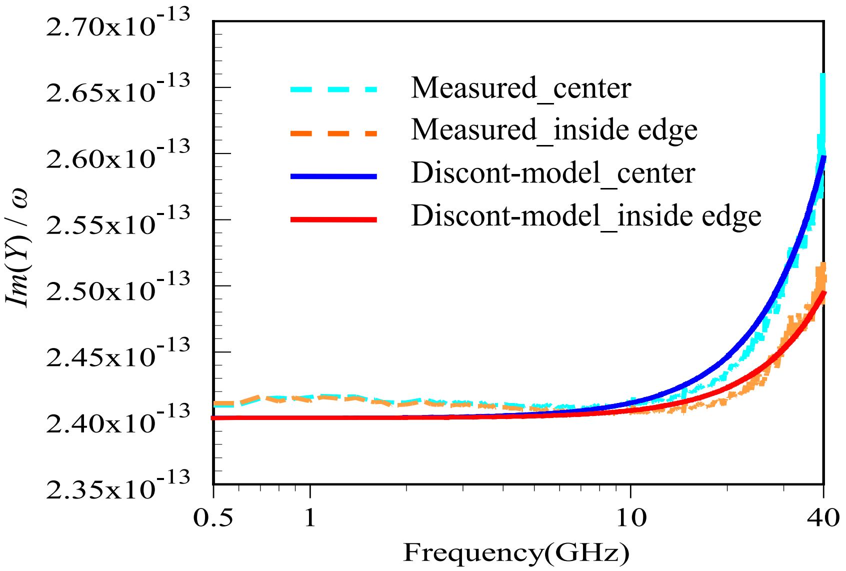

Figure 5.14: The extracted imaginary admittance from one-port measurement and calculated from lumped L_1-C_{pad} network model of open pad-only test structure. Magenta and orange-dotted curves: measured when a probe lands on center and inside edge position of the pad. Blue and red-solid curves: open pad modeled using lumped L_1 and C_{pad} shown in Figure 5.13. L_1 is due to geometrical discontinuity between probe tip and the pad. Fitted L_1s for center and inside edge landing position are 7×10^{-12} [H] and 2×10^{-12} [H], and corresponding C_{pad} is 2.43×10^{-13} [F].

Using this lumped L_1-C_{pad} de-embedding network model of pads, the extracted per unit length R and C of interconnect parameters of a 0.175μm wide and 2000μm long interconnect on SiO_2 dielectric thin film for a two-probe landing position are shown in Figure 5.15 and Figure 5.16. As we expect, the landing position dependency of the probe might be removed by considering the inductive discontinuity between the probe tip and pad. However, the extracted R is still decreasing at high frequencies for center and inside edge landing positions. Thus, considering the discontinuity between the probe tip and pad, the lumped L_1-C_{pad} model of the pad is still not enough to explain non-physical frequency dependencies of the extracted interconnect transmission line parameters.

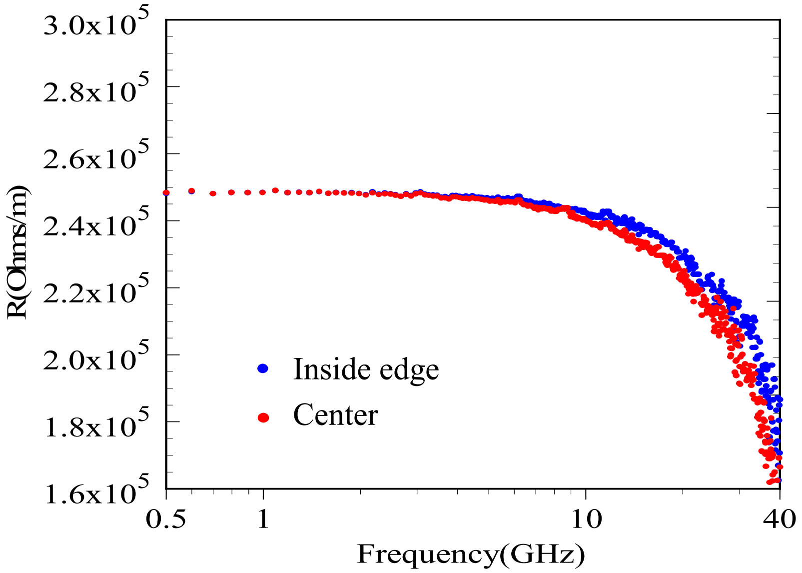

Figure 5.15: Extracted R per unit length of 0.175µm width and 2000µm line-length under lumped L_1-C_{pad} network model of pad (i.e., discontinuity between probe tip and pad: L_1).

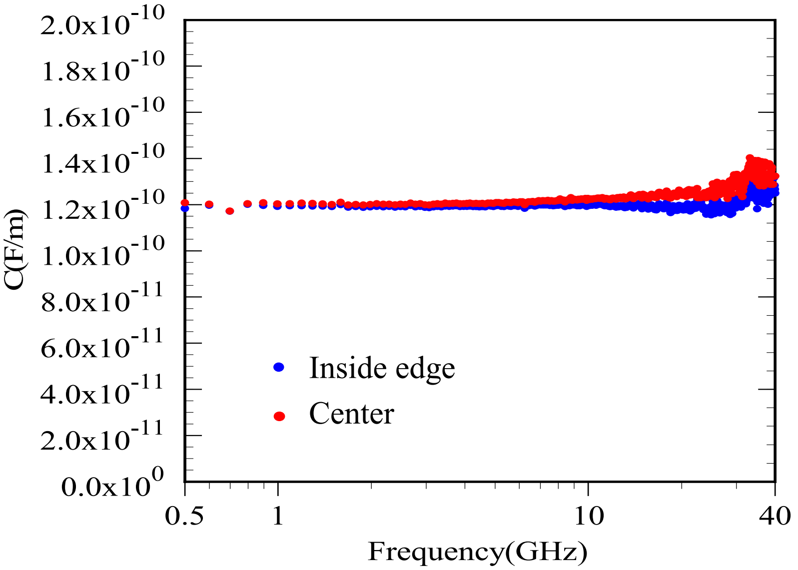

Figure 5.16: Extracted C per unit length of 0.175µm width and 2000µm line-length under lumped L_1-C_{pad} network model of pad (i.e., discontinuity between probe tip and pad: L_1).

After identifying the source of inductive discontinuity between the probe tip and pad (i.e., L_1) in the L_1-C_{pad} model (the discontinuity between probe tip and pad), we conclude that the discontinuity between the pad and the interconnect should also produce another inductive component (i.e., L_2) in the de-embedding network model. The new proposed L_1-C_{pad}-L_2 network model of de-embedding parasitics is illustrated in Figure 5.17. To clarify the two inductive discontinuities, we notate the inductive discontinuity between the probe tip and pad as L_1 and the inductive discontinuity between the pads and the interconnect transmission line L_2 as shown in the equivalent circuit model in Figure 5.17.

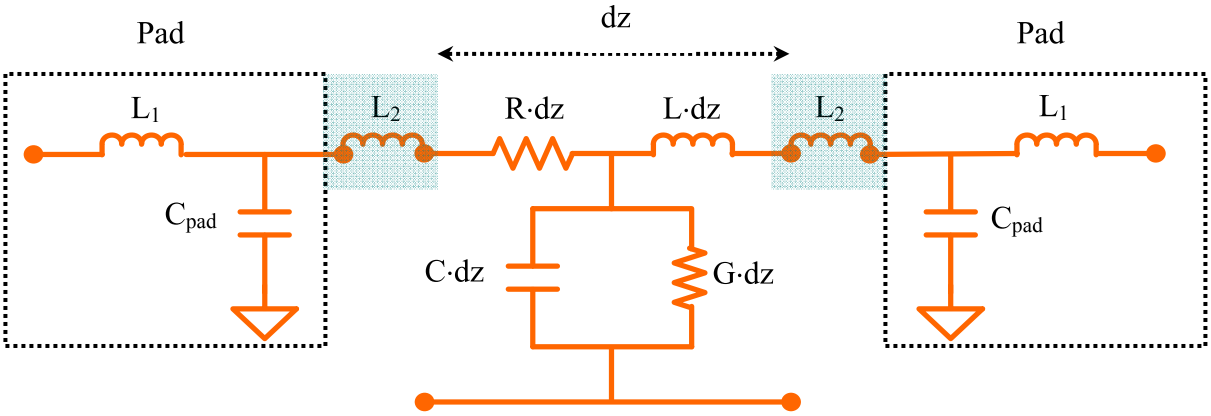

Figure 5.17: Lumped L_1-C_{pad}-L_2 network model of open pad-only test structure at both ends and interconnect transmission line at center. L_1 is due to geometrical discontinuity between probe tip and the pad. L_2 is discontinuity for changing width between pad and the interconnect transmission line.

In the L_1-C_{pad}-L_2 network model, this new L_2 may be bigger than L_1 in the lumped L_1-C_{pad} network model of pad because the width difference between the pad (i.e., 50µm) and the interconnect transmission line (0.175µm and 0.25µm) is much bigger than that between the probe tip and pad. For L_1 and C_{pad} in the lumped L_1-C_{pad}-L_2 network model shown in Figure 5.17, we use the fitted L_1 and measured low frequency C_{pad} from the one-port measurements of the pad-only test structures.

Figure 5.18 and Figure 5.19 illustrate how L_2 affects the extracted R per unit length of the tested interconnect transmission line of a 0.175μm wide and 2000μm long interconnect on SiO_2 dielectric thin film for center landing position. In Figure 5.18, the non-physical decreasing R as frequency increases can be compensated by varying L_2 in the lumped L_1-C_{pad}-L_2 network model. This network model shows that the L_2 need to correct the non-physical R.

Figure 5.18 also shows how sensitive the interconnect parameter extraction is to L_2 since we are attempting to extract the transmission line interconnect parameters only we do not know, a priori, how they should behave with frequency. One reasonable possibility, however, is that for the line-widths tested here R and C should be frequency independent, given that the lines are too small to exhibit skin effects, and strong frequency dependence of dielectric properties is not expected. To achieve this goal, we adjusted L_2 with fixed L_1 and C_{pad}; Figure 5.18 and Figure 5.19 show the extracted R per unit length of the interconnect transmission line with a fitted value of L_2 of 12×10^{-11} [H]. It is now clear that L_2 plays an important role in removing the non-physical behavior in the extracted line parameters.

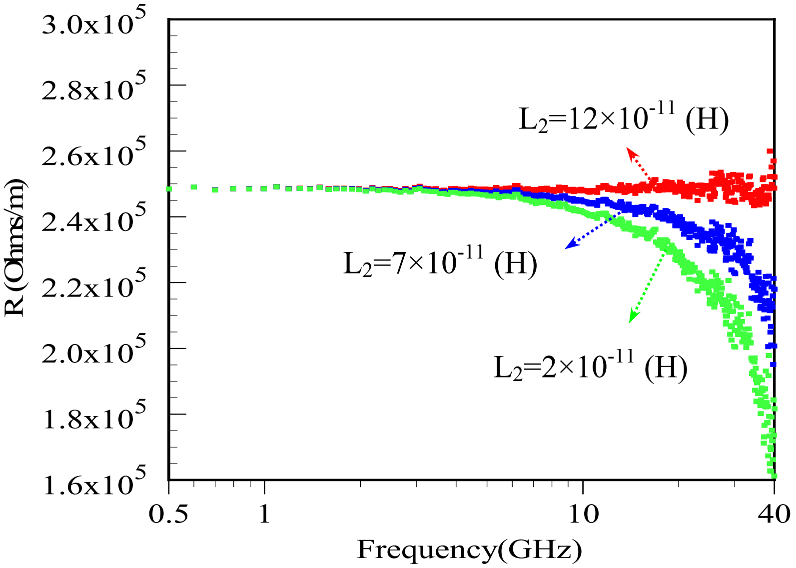

Figure 5.18: Sensitivity of discontinuity between a pad and transmission line interconnect, L_2. The extracted R per unit length of 0.175μm width and 2000μm wide transmission line interconnect varied by L_2.

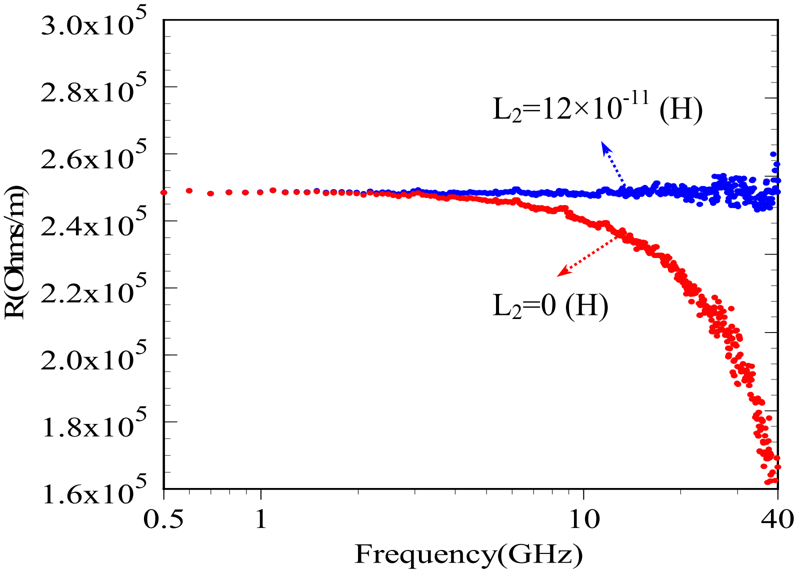

Figure 5.19: The extracted R per unit length of 0.175μm width and 2000μm wide transmission line interconnect from the lumped L_1-C_{pad}-L_2 network model shown in Figure 4.17 illustrating L_2 role to compensate non-physical line parameters.

In Figure 5.20, 5.21, 5.22, and Figure 5.23, we extract R and C per unit length from two different test sets. The interconnect transmission line in Figure 5.20 and Figure 5.21 is 0.175μm wide and 2000μm long on SiO_2 dielectric thin film. To verify the lumped L_1-C_{pad}-L_2 network model, another geometry with a different line width and length is tested. Figure 5.22 and Figure 5.23 present the extracted R and C per unit length of a 0.25μm wide and 2100μm long interconnect transmission line on SiO_2 dielectric thin film based on the lumped L_1-C_{pad}-L_2 network model. In these sets we compare different geometries with different landing positions of the probe using the lumped L_1-C_{pad}-L_2 network model.

In both sets, L_2 is roughly the same whatever the landing positions are. Here the best fitted L_2s for 0.175μm geometry and 0.25μm geometry are 12×10^{-11} [H] and 8×10^{-11} [H], respectively. From this observation, roughly speaking, L_2 in the L_1-C_{pad}-L_2 model of the pad is independent of the landing position of the probe while L_1 is dependent on the landing position. Consequently, we can say that L_1 is due to current redistribution between the probe tips and pad, while L_2 is due to current redistribution between the pads and the interconnect transmission lines.

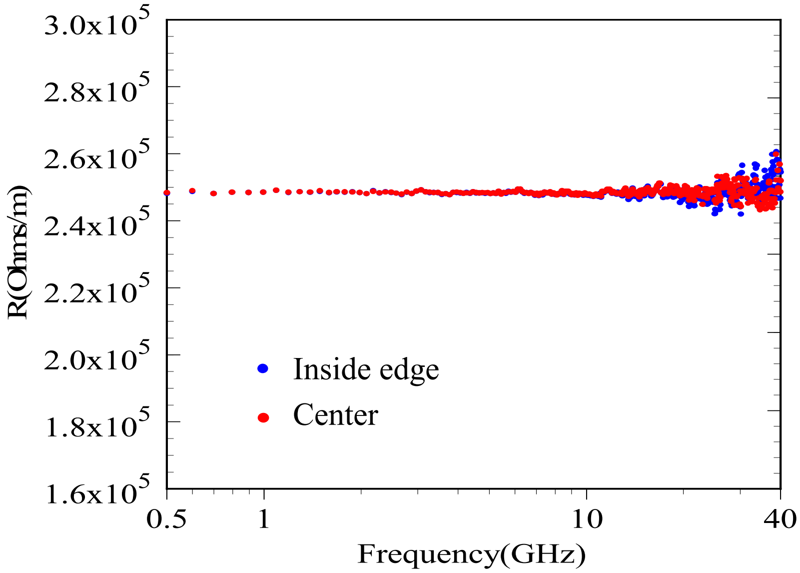

Figure 5.20: Extracted R per unit length of 0.175µm width and 2000µm line-length under lumped L_1-C_{pad}-L_2 network model (i.e., discontinuity between probe tip and pad: L_1 and discontinuity for changing width between probe pads and interconnect: L_2).

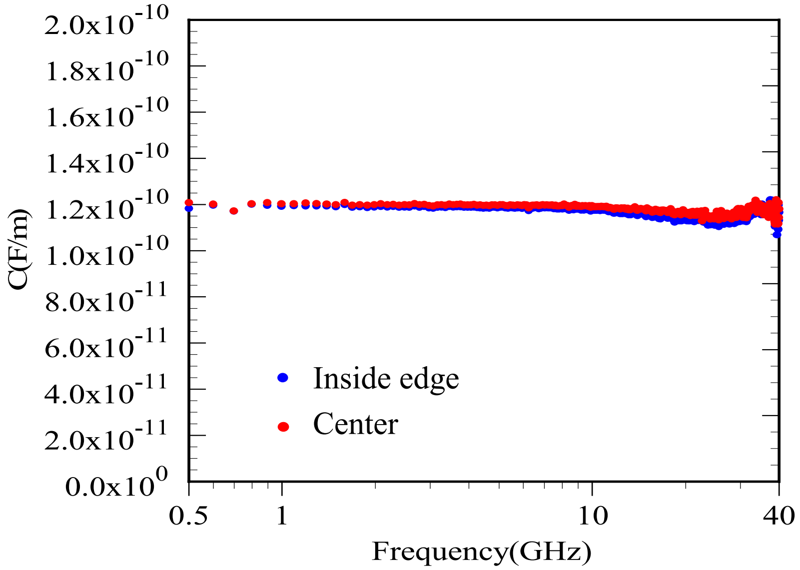

Figure 5.21: Extracted C per unit length of 0.175µm width and 2000µm line-length under lumped L_1-C_{pad}-L_2 network model (i.e., discontinuity between probe tip and pad: L_1 and discontinuity for changing width between probe pads and interconnect: L_2).

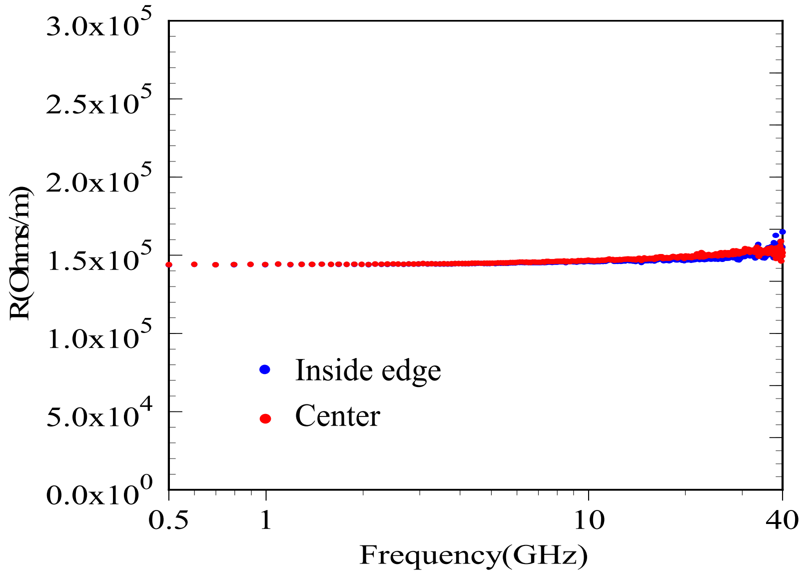

Figure 5.22: Extracted R per unit length of 0.25μm width and 2100μm line-length under lumped L_1-C_{pad}-L_2 network model (i.e., discontinuity between probe tip and pad: L_1 and discontinuity for changing width between probe pads and interconnect: L_2).

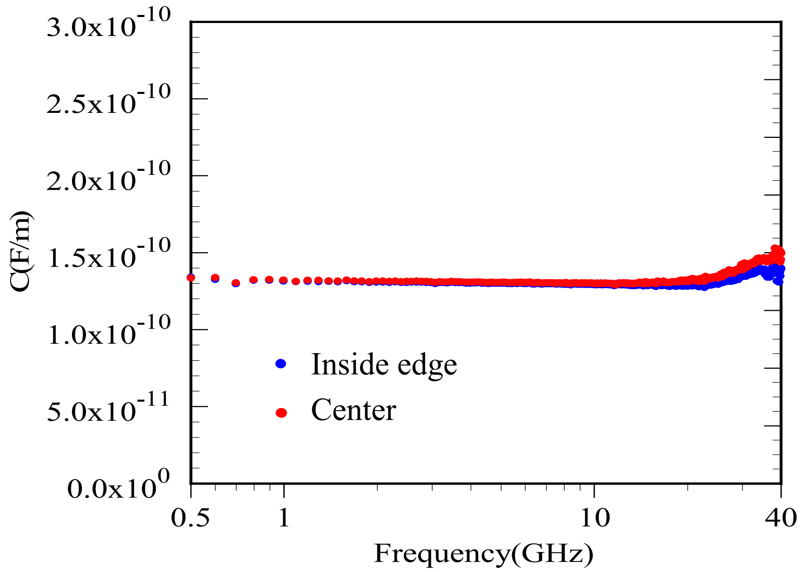

Figure 5.23: Extracted C per unit length of 0.25μm width and 2100μm line-length under lumped L_1-C_{pad}-L_2 network model (i.e., discontinuity between probe tip and pad: L_1 and discontinuity for changing width between probe pads and interconnect: L_2).

5.3 DISCUSSION

This chapter presented the impact of de-embedding network models for pad parasitics on the extraction of interconnect parameters at high frequencies. In the extraction procedure of interconnect parameters, the extracted R and C per unit length for different landing positions on the pads were presented using various de-embedding techniques for the pad parasitics at both ends of the interconnect transmission line. This chapter has also presented data for high frequency measurements up to 40GHz that show the location of microwave probes on 50micron square pads can have significant effects on the extracted per unit length RLCG interconnect parameters at frequencies above about 20GHz unless careful concern is taken in modeling the probe to pad interactions. As a result, a feasible explanation for the apparent non-physical high frequency dependencies in the extracted parameters might be the use of an incorrect network model of the probe pads.

A method is presented which can be used to extract the interconnect parameters based on many de-embedding network models. Among these, as far as the author knows, the discontinuities model (i.e., lumped L_1-C_{pad}-L_2) is the best model for extracting the desired interconnect parameters. In the lumped L_1-C_{pad}-L_2 network model, the most obvious pad parasitics are capacitive parasitics (i.e., C_{pad}) that, in these test structures, is comparable to the interconnect capacitance. In addition, inductive discontinuities (i.e. L_1 and L_2) resulting from geometrical discontinuities are required [38, 57]. Two inductive discontinuities were used: one (L_2) is due to the change in pad-width (i.e., 50μm) to interconnect line-width (i.e., 0.175μm and 0.25μm tested here), and the other (L_1) from probe tip to pads. In this chapter the results have shown the L_2 may be independent of probe landing position, while L_1 is a function of probe landing position on the pads.

Using a lumped L_1-C_{pad}-L_2 network model of pad parasitics and these discontinuities we have shown a more accurate extraction of the interconnect transmission line parameters.

Chapter 6

Conclusions

This dissertation aimed to thoroughly examine the accurate electrical parameter extraction and characterization of on-wafer embedded microstrip transmission line test structures using high frequency measurements up to 40GHz in determining on-going high-speed digital integrated system performance. In particular we aimed to determine the dielectric constant and loss of low-k dielectric materials, as well as the accurate de-embedding network model of pads on interconnect parameter extraction, the impact of error propagation on the extracted parameters, and the impact of probe placement on high frequency on-wafer measurements.

In Chapter 2, we presented the characterization of low-ks (low-k2 (Coral) and low-k1 (JSR)), and SiO_2 dielectrics via one-port measurements with the extraction of the dielectric constant, and loss using pad-only test structures instead of transmission line interconnects because extraction of loss tangent is very difficult due to high conductor loss for on-chip interconnects, even when using data from the shortest line length with widest line width. Regardless, accurate extraction of the loss tangent is very difficult since the magnitude of the conductor loss is much greater than the dielectric loss. In addition, we presented the characterization of copper and low-k / SiO_2 transmission line interconnects with the extraction of RLCG per unit length parameters via two-port high frequency measurements. Extraction of line parameters for different geometries of transmission lines with various dielectric thin films (SiO_2, low-k2 (Coral), and low-k1 (JSR)), various geometries (5μm, 0.25μm, and 0.175μm line-widths), and various line-lengths (i.e., varying length for each line-width) tested in this chapter has apparent non-physical frequency dependence at higher frequencies (i.e., over 20GHz). Thus, we have proposed that the apparent frequency dependence is likely due to measurement error or extraction error, not the skin effect.

In Chapter 3 and 4, we have discussed the measurement errors from systematic uncertainties via raw data from high frequency measurements and simulations using perturbation techniques. Several possible causes of apparent high frequency dependence for extracted interconnect parameters (i.e., R, L, C, and G per unit length) presented in chapter 2 could be magnitude detection limits, reference plane offset errors, or the wrong estimation of pad parasitics (i.e., C_{pad}) based on an assumed lumped RC network model. The most noticeable feature is the large error that occurs at frequencies higher than the magnitude detection limit frequency. The magnitude limit error is the dominant error if the magnitude of S_{21} is small enough for limiting to occur. The magnitude detection limit error is significant for the 0.25μm and 0.175μm geometries, and is dependent on the line length. The perturbation simulations have shown that any apparent frequency dependence at high frequencies might be an artifact due to finite measurement precision and accuracy, compounded by small calibration errors. Particularly, as shown in the perturbation simulations with errors propagation, a possible cause for non-physical high frequency dependencies might be reference plane offset error (length offset error), which is linearly dependent on frequency. Also, we have shown the investigation of the impact of probe placement on high frequency measurement to extract accurate parameters of on-chip interconnect experimentally in chapter 4.

In Chapter 5, the impact of de-embedding network models for pad parasitics on the extraction of interconnect parameters at high frequency was discussed. This chapter also presented data for high frequency measurements of up to 40GHz that show the location of microwave probes on 50micron square pads can have significant effects on the extracted per unit length RLCG interconnect parameters at frequencies above about 20GHz unless careful consideration is taken in modeling the probe to pad interactions. As a result, a feasible explanation for the apparent non-physical high frequency dependencies in the extracted parameters might be the use of an incorrect network model of the probe pads. A method is presented which can be used to extract the interconnect parameters based on many de-embedding network models in this chapter. Among these, as far as the author knows, the discontinuities model (i.e., lumped L_1-C_{pad}-L_2) is the best model for extracting the desired interconnect parameters for our test structures.

Bibliography

1. Association, S.I., *The International Technology Roadmap for Semiconductors*. 2003, Semiconductor Industry Association.
2. Young, B., *Digital Signal Integrity: Modeling and Simulation with Interconnects and Packages*. 2001: Prentice Hall PTR.
3. Theis, T.N., *The future of interconnection technology.* IBM J. Res. Develop., 2000. 44(3): p. 379.
4. Bakoglu, H.B., *Circuits, Interconnections, and Packaging for VLSI.* 1990, Massachusetts: Addison-Wesley Company.
5. Borkar, S., *Design challenges of technology scaling.* Micro, IEEE, 1999. 19(4): p. 23-29.
6. Fisher, P., *Clock Cycle Estimation and Test Challanges for Future Microprocessors*. May 08, 1998, SEMATECH: Austin, Texas.
7. Sylvester, D. and K. Keutzer. *Getting to the bottom of deep submicron*. in *Computer-Aided Design, 1998. ICCAD 98. Digest of Technical Papers. IEEE/ACM International Conference on*. 1998. Dept. of Electr. Eng. & Comput. Sci., California Univ., Berkeley, CA, USA: Practical.
8. Goldblatt, R.D., et al. *A high performance 0.13 μm copper BEOL technology with low-k dielectric*. in *Interconnect Technology Conference, 2000. Proceedings of the IEEE 2000 International*.
9. Cho, T., *Anisotropy of Low Dielectric Constant Materials and Reliability of Cu/Low-k Interconnects*. 2000, The University of Texas at Austin: Austin, Texas. p. 168.
10. Cregut, C., G. Le Carval, and J. Chilo. *High frequency modeling of interconnects in deep-submicron technologies*. in *Interconnect Technology, 1999. IEEE International Conference*. SNAKETECH, Voiron, France: Theoretical or Mathematical.

11. Ip, F. and C. Ting, *Dielectric Properties of Low Dielectric Constant Polymeric Materials.* Materials Research Society Symposium Proceedings, 1995. 381: p. 135-139.
12. Janezic, M.D. and D.F. Williams. *Permittivity characterization from transmission-line measurement*. in *Microwave Symposium Digest, 1997., IEEE MTT-S International*. Nat. Inst. of Stand. & Technol., Boulder, CO, USA: Experimental.
13. Janezic, M.D.W., D.F. Blaschke, V. Karamcheti, A. and Chi Shih Chang, *Permittivity characterization of low-k thin films from transmission-line measurements.* Microwave Theory and Techniques, IEEE Transactions on, 2003. 51(1): p. 132- 136.
14. Williams, D.F. and R.B. Marks, *Accurate transmission line characterization.* IEEE Microwave and Guided Wave Letters [see also IEEE Microwave and Wireless Components Letters], 1993. 3(8): p. 247-249.
15. Zaage, S. and E. Groteluschen, *Characterization of the broadband transmission behavior of interconnections on silicon substrates.* Components, Hybrids, and Manufacturing Technology, IEEE Transactions on [see also IEEE Trans. on Components, Packaging, and Manufacturing Technology, Part A, B, C], 1993. 16(7): p. 686-691.
16. Marks, R. and D. Williams, *Electrical Characterization Methods for High-Speed Interconnections.* The International Journal of Microcircuits and Electronic Packaging, 1995. 18(3): p. 207-216.
17. Lipa, S., et al., *Experimental characterization of transmission lines in thin-film multichip modules.* Components, Packaging, and Manufacturing Technology, Part A, IEEE Transactions on [see also Components, Hybrids, and Manufacturing Technology, IEEE Transactions on], 1996. 19(1): p. 122-126.
18. Deutsch, A., *Electrical characteristics of interconnections for high-performance systems.* Proceedings of the IEEE, 1998. 86(2): p. 315-357.

19. Deutsch, A., et al., *When are transmission-line effects important for on-chip interconnections?* Microwave Theory and Techniques, IEEE Transactions on, 1997. 45(10): p. 1836-1846.

20. Deutsch, A., et al., *Frequency-dependent losses on high-performance interconnections.* Electromagnetic Compatibility, IEEE Transactions on, 2001. 43(4): p. 446-465.

21. Basel, M.S., et al. *High speed digital system simulation using frequency dependent transmission line network modeling*. in *Microwave Symposium Digest, 1991., IEEE MTT-S International*. 1991. North Carolina State Univ., Raleigh, NC, USA, Practical Theoretical or Mathematical.

22. Biswas, B., et al. *Experimental electrical characterization of on-chip interconnects*. in *Electrical Performance of Electronic Packaging, 1997., IEEE 6th Topical Meeting on*. Dept. of Electr. & Comput. Eng., North Carolina State Univ., Raleigh, NC, USA: Experimental.

23. Arz, U., et al. *Accurate electrical measurement of coupled lines on lossy silicon*. in *Electrical Performance of Electronic Packaging, 2000, IEEE Conference on.* Lab. for Inf. Technol., Hannover Univ., Germany: Practical.

24. Friar, R.J. and D.P. Neikirk. *Experimental determination of the importance of inductance in sub-micron microstrip lines*. in *Interconnect Technology, 1999. IEEE International Conference*. Electr. Eng. Res. Lab., Texas Univ., Austin, TX, USA: Practical Theoretical or Mathematical Experimental.

25. Glaser, A., et al. *A Method for On-Chip Interconnect Characterization*. in *IEEE Fourth Topical Meeting on Electrical Performance of Electronic Packaging*. 1995. Portland, Oregon: IEEE.

26. Goldberg, S.B., et al., *Experimental electrical characterization of interconnects and discontinuities in high-speed digital systems.* Components, Hybrids, and Manufacturing Technology, IEEE Transactions on [see also IEEE Trans. on Components, Packaging, and Manufacturing Technology, Part A, B, C], 1991. 14(4): p. 761-765.

27. Kiziloglu, K., et al., *Experimental Analysis of Transmission Line Parameters in High-Speed GaAs Digital Circuit Interconnects.* IEEE Transactions on Microwave Theory and Techniques, 1991. 39(8): p. 1361-1367.

28. Hewlett-Packard, *Applying Error Correction to Network Analyzer Measurements*. 1997.

29. Friar, R.J. and D.P. Neikirk. *Limitations due to systematic phase errors on the extraction of loss tangent from micron-sized transmission line test structures*. in *Electrical Performance of Electronic Packaging, 1999*. Texas Univ., Austin, TX, USA: Practical Theoretical or Mathematical Experimental.

30. Friar, R.J. and D.P. Neikirk, *Limitations on the extraction of loss tangent from submicron transmission line test structures.* Advanced Packaging, IEEE Transactions on [see also Components, Packaging and Manufacturing Technology, Part B: Advanced Packaging, IEEE Transactions on], 2000. 23(3): p. 393-397.

31. Kim, J. and D.P. Neikirk. *Experimental characterization of copper/low-k transmission line interconnects through microwave measurements*. in *Electrical Performance of Electronic Packaging, 2003*.

32. Neikirk, D.P., J. Kim, and R. Friar, *Test Structure Design, Modeling, and Validation of High Frequency Cu Transmission Line Effects*. 2001, The University of Texas at Austin: Austin, Texas.

33. Hackborn, R., *An automatic network analyzer system.* Microwave Journal, 11(May 1968): p. 45-52.

34. Adam, S., *Automatic Microwave Network Measurements.* Proceedings of the IEEE, 1978. 66(4): p. 384-391.

35. Pervere, J.T.B.a.M.J. *A generalized vector network analyzer calibration technique*. in *34th ARFTG conf.* Dec. 1989. Ft. Lauderdale, FL.

36. Gupta, K.C., *Computer Aided Design of Microwave Circuits*. 1981: Artech House, Inc.

37. Rizzi, P.A., *Microwave Engineering Passive Circuits*. 1988, Englewood Cliffs, NJ: Prentice Hall. 572.

38. Gupta, K.C., et al., *Microstrip Lines and Slotlines*. 2nd edition: 1996, Arthech House.

39. Gonzalez, G., *Microwave Transistor Amplifiers: Analysis and Design*. Second ed. 1996: Prentice Hall.

40. Pozar, *Microwave Engineering*. 1990, New York: Addison-Wesley. p. 220-244.

41. Eisenstadt, W.R. and Y. Eo. *Determination of IC interconnect line parameters by S-parameter measurements*. in *VLSI Multilevel Interconnection Conference, 1991, Proceedings., Eighth International IEEE*. 1991. Florida Univ., Gainesville, FL, USA: Practical Experimental.

42. Eisenstadt, W. and Y. Eo, *S-Parameter-Based IC Interconnect Transmission Line Characterization.* IEEE Transactions on Components, Hybrids, and Manufacturing Technology, 1992. 15(4): p. 483-490.

43. Eo, Y., W.R. Eisenstadt, and J. Shim, *S-parameter-measurement-based high-speed signal transient characterization of VLSI interconnects on SiO/sub 2/-Si substrate.* Advanced Packaging, IEEE Transactions on [see also Components, Packaging and Manufacturing Technology, Part B: Advanced Packaging, IEEE Transactions on], 2000. 23(3): p. 470-479.

44. Ryu, W., et al., *Embedded microstrip interconnection lines for gigahertz digital circuits.* Advanced Packaging, IEEE Transactions on [see also Components, Packaging and Manufacturing Technology, Part B: Advanced Packaging, IEEE Transactions on], 2000. 23(3): p. 495-503.

45. Steer, M.B., et al. *Introducing the through-line deembedding procedure*. in *Microwave Symposium Digest, 1992., IEEE MTT-S International*. Dept. of Electr. & Comput. Eng., North Carolina State Univ., Raleigh, NC, USA

46. S.Kim, e.a., *SIMIAN USER'S GUIDE*. 1997, The University of Texas at Austin.

47. Friar, R.J., *Analysis, Design, and Measurement of On-Wafer Transmission Line Test Structures*. 2000, The University of Texas at Austin. p. 77.

48. Kim, J. and D.P. Neikirk. *Impact of Probe Placement on High Frequency Measurements of On-Chip Interconnects*. in *Electrical Performance of Electronic Packaging, 2005*.

49. Hewlett-Packard, *HP Test & Measurement 1999 Catalog*. 1999.

50. Hewlett-Packard, ed. *HP Test & Measurement 2001 Catalog*. 2001.

51. Cascade Microtech, I., *Proper Infinity Probe Alignment on Various ISSs.* 2002 (INFISS-APP-1102).

52. Ramo, S., J. Whinnery, and T.V. Duzer, *Fields and Waves in Communication Electronics*. 1965, New York: John Wiley & Sons. 754.

53. Ryu, W., et al. *Interconnection line structures on MCM-Si for giga-hertz quasi-TEM signal transmission*. in *Electronic Components and Technology Conference, 48th IEEE*. 1998. Dept. of Electr. Eng., Korea Adv. Inst. of Sci. & Technol., Seoul, South Korea: Application Practical Experimental.

54. Mondal, J., *Propagation Constant Determination in Microwvae Fixture De-embedding Procedure.* IEEE Transactions on Microwave Theory and Techniques, 1988. 36(4): p. 706-713.

55. Winkel, T.-M. *An accurate and complete frequency dependent transmission line characterization using S-parameter measurements*. in *Electrical Performance of Electronic Packaging, 1999.*

56. Eo, Y. and W.R. Eisenstadt, *High-speed VLSI interconnect modeling based on S-parameter measurements.* Components, Hybrids, and Manufacturing Technology, IEEE Transactions on [see also IEEE Trans. on Components, Packaging, and Manufacturing Technology, Part A, B, C], 1993. 16(5): p. 555-562.

57. Gopinath, A., A.F. Thomson, and I.M. Stephenson, *Equivalent Circuit Parameters of Microstrip Step Change in Width and Cross Junctions (Short Papers).* Microwave Theory and Techniques, IEEE Transactions on, 1976. 24(3): p. 142-144.

Vita

Jooyong Kim was born in Seoul, Korea on June 9, 1969, the son of In-Soo Kim and Kyeong-Hyuk Ihm. He earned the degree of Bachelor of Science from Dankook University in 1994. He entered the Graduate School of the University of Colorado at Boulder, Colorado, in August 1995. He received the degree of Master of Science in Engineering in August 1997. In the same year, he entered the Graduate School of Texas A&M University at College Station in Electrical and Computing Engineering. In August 1998, he transferred to the Graduate School of the University of Texas at Austin for his Ph.D. degree in Electrical & Computer Engineering. He joined the MicroElectromagnetics Device Group supervised by Dr. Dean P. Neikirk in 1999. During 1999 and 2000, he was employed as a technical intern at International SEMATECH developing and modeling interconnect issues in Copper and low-ks dielectrics. From 2000 to 2006, he worked in the research and development of on-chip interconnects in high frequency as a research assistant under Professor Dean P. Neikirk.

Permanent address: Kyerong Apt. 112-501, Chongsol Maul, Keumkook Dong,
Pundang Gu, Seong Nam, Korea

This dissertation was typed by the author.